

The Pennsylvania State University

The Graduate School

**DEVELOPMENT AND IMPLEMENTATION OF A HYBRID
VOLUME OF FLUID/LEVEL SET METHOD TO STUDY
TWO-PHASE FLOWS**

A Thesis in

Chemical Engineering

by

Anthony Daniel Fick

© 2007 Anthony Daniel Fick

Submitted in Partial Fulfillment

of the Requirements

for the Degree of

Doctor of Philosophy

May 2007

The thesis of Anthony Daniel Fick was reviewed and approved* by the following:

Ali Borhan

Professor of Chemical Engineering

Thesis Advisor, Chair of Committee

Andrew L. Zydney

Professor of Chemical Engineering

Walter L. Robb Chair and Head of the Department of Chemical Engineering

Darrell Velegol

Associate Professor of Chemical Engineering

Andrew Belmonte

Associate Professor of Mathematics

*Signatures are on file in the Graduate School.

Abstract

Simulation of two-phase flows is a complicated problem due to the nature of interfacial behavior. Knowledge of the shape of the interface is required to determine the flow field. Thus computations need to recreate the interface for each time step. In this work, a new method is described that combines the best features of two previously utilized techniques, the Volume of Fluid and Level Set methods.

Since this is a new algorithm, the method is tested against a model problem of a drop within a tube. There is previous research on this problem both experimental and computational, which the results are compared with to display the accuracy of the simulation. The two main areas studied are buoyancy-driven motion of the drop and deformation of the drop within pressure-driven flow.

For buoyancy-driven flow, the change in density between the fluids causes the drop to rise until reaching a steady velocity. The stress on the drop causes it to change shape until equilibrium is reached. To verify the technique, simulations for small drops and low Reynolds numbers are compared with velocities from the ana-

lytical results for spheres. Computations done for deformable drops also compare well with previous experiments for drop velocity and shape. The effect of Capillary and Reynolds numbers are investigated in a parameter study. Increases in both numbers lead to increased deformation. This deformation elongates and narrows the drops and thus increases the migration velocity. It is also found that initial shape effects the steady state result of the simulation. Along with the other parameters, the viscosity ratio is varied and deformation is increased for both increases and decreases in the ratio. A power law fluid is utilized as the suspending fluid to test the effect of non-Newtonian fluids on the system. The power law shortens the drops and introduces a recirculation wake behind the drop for the higher power law index. This effect is seen to a lesser degree at smaller Reynolds number with smaller deformation. The power law also produces recirculation in front of larger sized drops due to the small gap between the drop and the wall.

In the case of pressure-driven flow, the deformation occurs by an entrant cavity in the back of the drop. Testing of the code is done again by comparison to previous results. A parameter study on Reynolds and Capillary numbers is carried out. For a certain Reynolds number, deformation increases with increasing Capillary numbers until a critical value is reached above which the drop breaks up and no steady shape can be found. The deformation increases with increasing Reynolds number, and thus the critical Capillary number decreases as the Reynolds number is increased. In two different studies, the critical Capillary number passes through a maximum value at small Reynolds numbers before falling below literature results at higher Reynolds numbers. The addition of a small amount of inertia appears to stabilize the drop while higher values produce larger deformations and the drop

breaks up at a lower Capillary number. The effect of viscosity ratio is also tested and the drop deformation increases with increasing viscosity ratio, a trend observed in earlier experiments. Last, the suspending fluid is modeled as a power law non-Newtonian fluid. The power law fluid produces drops with tapered heads and flattened backs. This shape is similar to the larger size ratios in buoyancy-driven motion and to previous experiments with viscoelastic fluids.

Table of Contents

List of Figures	ix
List of Tables	xiii
Acknowledgments	xv
Chapter 1	
Introduction	1
Chapter 2	
Background and Literature Review	4
2.1 <i>Drop Deformation</i>	5
2.1.1 Buoyancy-Driven Motion	6
2.1.2 Pressure-Driven Motion	13
2.1.3 Temperature-Driven Motion	17
2.2 <i>Mathematical Techniques</i>	19
2.2.1 Volume of Fluid	20

2.2.2	Level Set Function	24
2.2.3	Hybrid VOF/Level Set Method	28

Chapter 3

Problem Formulation and Solution Procedure	31
3.1 <i>Governing Equations</i>	32
3.1.1 Fluid Mechanics	32
3.1.2 Surface Equations	39
3.2 <i>Numerical Method</i>	43
3.2.1 General Solution Procedure	43
3.2.2 Determining the Velocity and Pressure Fields	43
3.2.3 Determining Surface Force and Moving the Interface	46
3.2.4 Overview of solution procedure	53

Chapter 4

Buoyancy-Driven Results	56
4.1 <i>Validating the Algorithm</i>	57
4.2 <i>Parametric Study of Various Dimensionless Groups</i>	64
4.2.1 Reynolds and Capillary Study	65
4.2.2 Viscosity Ratio Tests	76
4.2.3 Non-Newtonian Fluids	78
4.3 <i>Conclusions on Buoyancy-Driven Motion</i>	80

Chapter 5

Pressure-Driven Results	90
5.1 <i>Problem Formulation</i>	90

5.2	<i>Study on Drops in Pressure-Driven Flow</i>	94
5.2.1	Comparison to Experimental Results	94
5.2.2	Parameter Study of Reynolds and Capillary Numbers	97
5.2.3	Viscosity Ratio and Non-Newtonian Tests	110
5.3	<i>Conclusions on Pressure-Driven Flow</i>	116
 Chapter 6		
	Conclusions and Future Work	120
6.1	<i>Conclusions</i>	120
6.2	<i>Future Work</i>	127
	 Bibliography	 130

List of Figures

2-1	Schematic of two-phase flow within a tube	6
2-2	Drop shapes from Borhan and Pallinti [6]	9
2-3	Drop shapes from Borhan and Pallinti [30]	17
3-1	Schematic of two-phase flow within a tube	33
3-2	Control volume near the interface	36
3-3	Three cases for determining midpoint for VOF	41
3-4	Flowchart of solution procedure	44
3-5	Diagram describing the calculation of motion of fluid	51
4-1	Migration velocity ratio versus viscosity ratio for sphere and present work. Size ratio 1:20, Re 0.01.	59
4-2	Steady state bubble shapes from present work and from Ryskin and Leal 1984 [15]	61
4-3	Steady state drop shapes from present work and Borhan and Pallinti 1995 [6]	62

4-4	D , L_A , and L_R versus size ratio for present work and Borhan and Pallinti 1995 [6].	63
4-5	Migration velocity ratio versus size ratio for present work and Borhan and Pallinti 1995 [6].	64
4-6	Steady state drop shapes for parameter study. Size ratio 0.7, viscosity ratio 1.0, density ratio 0.7.	66
4-7	D , L_A , and L_R versus Capillary number for $Re=1, 10, 20$, and 50 . .	67
4-8	Transition of shapes for $Ca\ 5$ from $Re\ 20, 25, 35$, and 50	69
4-9	Transition of shapes for $Re\ 50$ from $Ca\ 10, 15$, and 20	69
4-10	Steady shapes for spherical starting simulations. $Re^* 1000$ and 2000 ; $Ca\ 1, 5, 10, 20$, and 50	70
4-11	D , L_A , and L_R versus Capillary number for $Re^* 1000$ and 2000 . . .	71
4-12	Comparison of shapes for $Re\ 50$, $Ca\ 5$; using converged solution or sphere as initial condition.	72
4-13	Comparison of shapes for $Re\ 20$, $Ca\ 50$; using converged solution or sphere as initial condition.	73
4-14	Migration velocity ratios versus Capillary number for $Re\ 1, 10, 20$, and 50	75
4-15	Streamfunctions for parameter study for $Re\ 1$ and 10	84
4-16	Streamfunctions for parameter study for $Re\ 20$ and 50	85
4-17	Surface velocity ratios versus arclength for $Re\ 50\ Ca\ 10$ shape. . . .	86
4-18	Steady state shape results from viscosity ratio test for $0.5, 1.0$ (base case), and 1.5	86
4-19	Streamfunctions for viscosity ratios 0.5 and 1.5	87

4-20	Steady state shape results from non-Newtonian fluid test for power law indexes 0.5, 1.0 (base case), and 1.5.	87
4-21	Streamfunctions for power law indices 0.5 and 1.5.	88
4-22	Steady state shape results from non-Newtonian fluid test for power law index 1.5, Re 10 size 0.7, and Re 1 sizes 0.7, 0.9, and 1.1.	88
4-23	Streamfunctions for power law index 1.5 and Re 10 and 1: size 0.7.	89
5-1	Centering drop by moving VOF values to lower grid points.	93
5-2	Comparison of present work shape (size ratio 0.7, viscosity ratio 1.0, density ratio 1.0, Re 0.1, and Ca 1.2) to results of Johnson 1999 [25].	95
5-3	Critical Capillary numbers versus size ratio for present work at Re 1, 5, 10, and 50 and results of Borhan and Pallinti 1995 [31]; simulation parameters viscosity ratio 0.2, density ratio 0.72, Bond number 0.4.	96
5-4	Steady state drops for Re 1, Ca values of 0.1, 0.5, 1, and 3.	98
5-5	Steady state drops for Re 5, Ca values of 0.1, 0.5, 1.0, and 2.5.	100
5-6	D , L_A , and L_R versus Capillary number for Re 1 and 5.	101
5-7	Steady state drops for Re 10, Ca values of 0.1, 0.5, 0.7, and 0.95.	102
5-8	D , L_A , and L_R versus Capillary number for Re 10.	103
5-9	Steady state drops for Re 50, Ca values of 0.1, 0.5, 0.7, and 0.83.	104
5-10	D , L_A , and L_R versus Capillary number for Re 50.	105
5-11	Migration velocity versus Capillary number for Re 1.	106
5-12	Migration velocity versus Capillary number for Re 5.	106
5-13	Migration velocity versus Capillary number for Re 10.	107
5-14	Migration velocity versus Capillary number for Re 50.	107
5-15	Streamfunctions for Re 1, Ca values of 0.1, 0.5, 1, and 3.	108

5-16	Streamfunctions for Re 5, Ca values of 0.1, 0.5, and 1.0.	109
5-17	Streamfunctions for Re 10, Ca values of 0.1, 0.5, and 0.7.	110
5-18	Streamfunctions for Re 50, Ca values of 0.1, 0.5, and 0.7.	111
5-19	Steady state shape results from viscosity ratio test for 0.5, 1.0 (base case), and 1.5.	112
5-20	Streamfunctions from viscosity ratio test for 0.5, 1.0 (base case), and 1.5.	113
5-21	Steady state shape results from power law index test for 0.5, 1.0 (base case), and 1.2.	115
5-22	Streamfunctions from power law index test for 0.5, 1.0 (base case), and 1.2.	116

List of Tables

3-1	Volumes leaving computational cell for all cases	52
4-1	Migration velocity ratios for various size ratios, number of grid points, and calculated spherical values. Simulation parameters: viscosity ratio 0.25, density ratio 0.7, Re 0.01	60
4-2	Results from viscosity ratio test along with base case values	77
4-3	Results from non-Newtonian fluid test along with base case values .	78
5-1	Comparison of simulation to literature result for relative drop velocity and additional pressure loss [27].	95
5-2	Critical Capillary numbers at various Reynolds numbers including literature result [28].	110
5-3	Results from viscosity ratio test along with base case values	112
5-4	Comparison of simulation to literature result for relative drop velocity and additional pressure loss [27].	114
5-5	Results from power law index test along with base case values . . .	114

6-1	Curvature of spherical drop calculated by hybrid VOF/Level Set method and VOF method	126
-----	---	-----

Acknowledgments

Spending eleven years at one university, there are a multitude of people who have helped me along the way and made the most of my time in State College. As this is the last document I give to Penn State, I would like to take this opportunity to remember those who have supported me.

First, I need to thank Dr Ali Borhan, my advisor for my entire Penn State career. Besides teaching me about fluid mechanics and mathematical techniques, he had confidence in my abilities to complete the project despite the setbacks. Also, I have had the unique opportunity to join him on several volleyball teams. This allowed me to see a different side of my advisor, and it was a honor to play on the same team with him.

I also thank the Penn State Academic Computing Fellowship which funded my work for three years. Not only did I gain monetarily, but also the program gave me a chance to interact with other Fellows and to visit different facilities on campus I had no idea even existed.

Besides my academic help, I am most indebted to the past and present members

and staff of the team presently called the "Gridiron Gargoyles". There are far too many names to thank them all, but I would like to single out the members of our most successful and my favorite team, the 2003 team. This team gave me something to look forward to and a reason to stay when I wanted to quit. I thank them all for everything. The best defense in the IM league included Mario, Matt, Joe, Susan, Anne, Justin, and Kelly. Although I am biased, I appreciate the most prolific offense, scaled to IM dimensions, ever seen at Penn State more than the defense. Tim, the fastest receiver I have ever thrown to; Jen, the best girl receiver; Byron and Dave, who both made big catches; Kristin with our trick touchdown play; and Natalie, who would always give me words of encouragement right before the play started. It was an honor to share the huddle with you, and the best team I've ever played with. Also, the team would not be the same without Erik, and Dr. Lloyd. Thank you both for everything.

In my work, there were many days when nothing was going right and the solution seemed impossible. My job with Target of State College helped me through those times. It was refreshing to be able to accomplish something, help other people, and be good at a job. Along with that, I had the opportunity to work with some amazing people that wanted me to reach my goal of a Ph.D. I would like to thank them all, but to limit space I will just name a few here. Thank you to Kathy Bricker for help with my job search and a lot of homemade food. Thanks to Garnett for trying to marry me off to complete strangers. Last, thank you to Julie and Brenda for getting me a pizza the night I was starving for food. Everyone at Target has been the best to work with and I appreciate them all.

While some people at work have treated me like family, none of them can

replace my own wonderful family who I need to thank as well. Graduate school gave me a chance to spend three more years at the same school as my brother Jim, and I wish I could have a few decades more. My brother has been there for me all my life, has truly supported me in everything, and I thank him very much. Obtaining this degree will be the only thing that I do that my sister did not accomplish before me. Thank you Ann Marie for all your advice, help, and giving me goals to set my sights on. Last but not least, to my mom, dad, and dziadzi. You all have had faith in me even when I did not. Thank you for your faith, your love, and your support.

Since I have so much time in State College, I have spent much more time with my roommates than my family. During two interesting years, I lived with some of the best roommates and friends I have ever known. Mike and Rory helped me battle the evil Tim, and fixed my car with rope and bungee cords. Mike is the crazed defensive lineman that breaks down doors, has no short term memory, and tells everyone any secret about me. He has also provided me with a lot of advice and is a true friend. Rory is a two time Heisman trophy winner, with a love for oreos, and enjoys hurling objects at me whenever he can. He also has helped me discuss many of my problems and vent a lot of my frustrations. Thanks to you both.

The last roommate I have to thank, is also the most important person in my life. Besides being my former roommate, she is my best friend and the love of my life. In the movie "Spiderman2", Mary Jane Watson asks the hero, Peter Parker, if someone should save him. Thank you Dr. Kimberly Susan Fick for saving me.

Introduction

Flow problems involving more than one fluid are prevalent across many different disciplines. Mixtures of multiple liquids or liquids and gases occur throughout the world. Modeling the flow characteristics of these fluids is complicated due to the behavior of the interface between the fluids. Numerical simulations of the systems need to capture this interface behavior and predict its impact on the overall flow. The work presented here describes a novel approach to simulating two-phase flows. Since this is a new algorithm, it will be applied to the model problem of a drop and suspending fluid in a confined domain.

There is much information in the literature for this model problem. The algorithm will be validated by comparison with previous experimental and numerical studies. Chapter 2 will review the literature on drop deformation for both buoyancy-driven and pressure-driven flows. This chapter will also present the past numerical techniques utilized for two-phase flows which are the base for the new

algorithm.

Presented in Chapter 3 are the governing equations behind the fluid mechanics and surface mechanics. The important parameters and variables for the system are defined as well. Last, the chapter will describe the simulation procedure and numerical techniques utilized in the algorithm.

The algorithm will be tested against analytical results for the buoyancy-driven rise of a drop in both an infinite domain and within a pipe for no deformation. The simulation shape and velocity will be compared with the expected results. Also, experimental data is available for deformable drops at low Reynolds numbers. Chapter 4 will present the results for all these tests. The simulation allows values of the parameters to be tested outside of easily accomplished laboratory experiments. The effect of these parameters is presented in a parameter study for buoyancy-driven motion within the chapter as well.

Another important class of flow problems involves pressure-driven flow. The simulation is generalized for a pressure-driven flow system. Deformation and criteria for drop break up are studied in this system and compared with previous work. The effect of finite Reynolds numbers is determined and presented in Chapter 5.

The new algorithm is able to match previous experimental and analytical solutions for a drop in a tube. The simulations of various parameter values show the effect of inertia on drop shape and velocity. New critical capillary numbers are found for pressure-driven flow at higher Reynolds numbers, and the effect on

non-Newtonian fluids is investigated. Chapter 6 discusses the conclusions of the work as well as future applications of utilizing this technique for other two-phase flow problems.

Background and Literature Review

The motion of drops and bubbles in a confined fluid medium is a problem of great practical importance in a variety of natural physical processes as well as a host of industrial applications. Much of the earliest interest in this subject was motivated by the suggested analogy between the drop motion and the motion of blood cells in the capillaries. Similar flow problems also arise in many polymer-processing operations (e.g., fiber spinning, film blowing, injection molding) where additives are used in order to achieve certain required physical/mechanical properties in the final products. The additives, generally being low molecular weight materials compared to the base polymer, can form a droplet phase suspended in the base polymer during the fabrication process. Similar droplet dispersions can also be formed when two or more polymers are mixed in processing of polymer blends, and the rheological properties of these two-phase polymer melts are found to be strongly influenced by the state of the dispersion [1] (i.e., by the distributions

of droplet size and shape which, in turn, are affected by the possible dispersion processes that can occur).

Aside from the aforementioned technical applications, the motion of drops through tubes of constant and variable cross-section remains a problem of considerable fundamental importance as a pore-scale model for studying the dynamics of two-phase flow through porous media. Although a straight cylindrical tube is a gross oversimplification of the true internal geometry of porous materials, it allows an examination of the effects of confining boundaries and rheological properties of the two-phase system on the pressure drop-volume flux relationship, which is the primary function of interest in the macroscopic description of multiphase flow through porous media, and the subsequent critical conditions for drop breakup. Hence, numerous studies have been devoted to this model problem, a summary of which is provided by Olbricht [2]. The following sections discuss experimental and theoretical work on the deformation of two-phase flows, the mathematical methods employed to simulate such problems, and the algorithm utilized in this work to model drop deformation in a confined domain.

2.1 *Drop Deformation*

Drop motion within tubes occurs under a variety of different conditions, and experimental and theoretical studies have been carried out for each system. These studies show the type and magnitude of drop deformation varies depending on the

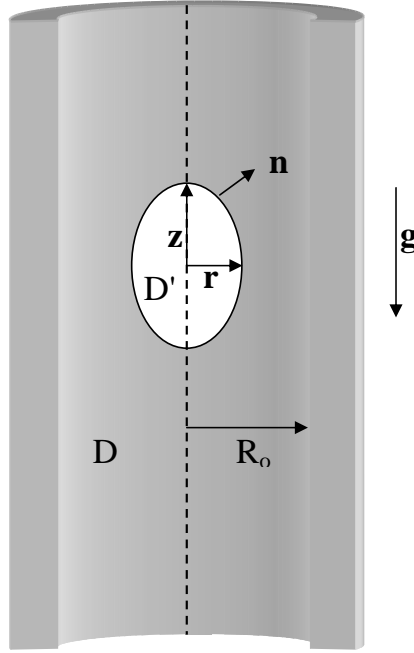


Figure 2-1. Schematic of two-phase flow within a tube

driving force of the flow. Therefore three different driving forces for drop motions are described to illustrate previous research and the resulting interface shapes.

2.1.1 Buoyancy-Driven Motion

An example of a two-phase system in a gravitational field is shown in figure 2-1. The force on the drop attributed to gravity and buoyancy is given by Eq. 2.1

$$F = (\rho - \rho')Vg \quad (2.1)$$

where V is the volume of the drop, g is the acceleration due to gravity, ρ is the density of the suspending fluid (represented by D in the diagram), and ρ' is the

density of the drop (D'). Figure 2-1 also displays the tube radius R_o . From equation 2.1, the force is either positive or negative depending on the difference in density. The drop rises for a positive force and falls when the force is negative. Once the drop is in motion, it also experiences a drag force. This drag force is a function of the velocity of the drop as well as the drop shape. The net force on the drop in motion is given by Eq. 2.2

$$F_{net} = (\rho - \rho')Vg + F_{drag}(\vec{v}) \quad (2.2)$$

The drop accelerates until all the forces are in equilibrium, and the drop attains a steady state velocity. This velocity is dependent on the shape of the drop through the drag force contribution. Thus the surface tension of the interface plays a role in determining the steady state of the system.

Most of the experimental work in this area has been done for the motion of large gas bubbles within capillaries at low Reynolds number. A 1961 study by Bretherton [3] obtained the increase in speed of a long bubble over the average speed of the suspending fluid. In these experiments, the bubble was separated from the capillary wall by a thin film of fluid, and inertial effects were neglected. Goldsmith and Mason [4] carried out similar large bubble experiments with air as well as viscous bubbles. The study determined velocity fields in the suspending fluid and within the viscous bubbles using tracer particles, as well as obtained the

thickness of the film between the bubble and the wall. Some of the trials in the study used surfactants so the results cannot be compared to a clean surface, or a surface devoid of surfactants. To determine the wall effects in capillary problems, Coutanceau and Thizon [5] investigated the problem of a single bubble rising within another fluid inside a circular tube. Velocity profiles and shape results were found for a variety of bubble/tube size ratios. The wall was found to influence the bubble terminal velocity even before shape changes occurred.

While there is a large amount of experimental data for buoyancy-driven motion of bubbles within a tube, there is not as much information in literature for viscous drops. An examination on the effects of a variety of parameters was conducted in 1995 by Borhan and Pallinti [6]. In this work, three separate suspending fluids, di(ethylene glycol), a corn syrup-water mixture, and various aqueous glycerol solutions, were used. The drop fluids consisted of Dow Corning fluids, Ucon oils, silicon oil, and air. Along with the variety of fluids, three different sized capillary tubes allowed a wide range of drop size ratios, the ratio of the drop radius to the tube radius, viscosity ratios, and Bond numbers. The Bond number compares the magnitude of the gravitational and viscous components of the equations of motion. The experiments collected the migration velocity and steady state drop shapes. Examples of these shapes are shown in Figure 2-2.

The increasing size ratios in figure 2-2 correspond to increasing drop radii. The work also developed a boundary integral numerical simulation to compare simula-

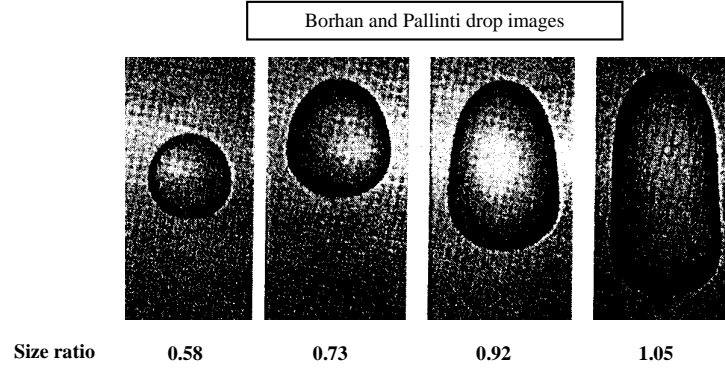


Figure 2-2. Drop shapes from Borhan and Pallinti [6]

tion results to experimental results. The data displayed a range of deformation as well as the effect the different parameters had on migration velocity and shape.

Other experimental work looked into the effect of deformation on multiple drops. A 1993 study by Manga and Stone [7] investigated the interactions between two deformable drops rising in a tube. Boundary integral simulations were done along with the laboratory experiments to model results. Using different sized drops, the study determined the impact deformation has on the coalescence of drops. The present work focuses on deformation of a single drop within a tube, however the method could be used for modeling coalescence of multiple drops.

On the theoretical side, the majority of the work in the literature described drop deformation in an infinite domain. A good review of the studies on buoyancy-driven motion up to 1978 is given by Clift et al. [8]. Some example works of drops in an infinite domain are [9, 10]. One of the earliest was by Taylor and Acrivos

in 1964 [9]. Taylor and Acrivos obtained a perturbation solution of the equations of motion to investigate motion at low Reynolds numbers. The study determined the deformation of the drop and showed this deformation affects the drag on the drop. The deformation was found to be insensitive to the viscosity ratio for the limit of low Reynolds number and negligible inertial effects. Cox, [10], developed theoretical expansions to describe small drop deformations in time dependent flow fields. The results showed deformations as well as the velocity fields within and around the drop. A 1992 work by Pozrikidis, [11], provides a more recent review of studies in the infinite domain and drops within tubes. The work also numerically simulated the motion of a train of drops within a tube by a boundary integral method.

For the previous studies the Reynolds number is so small, the inertial effects are not seen. Neglecting these inertial effects eliminates important aspects of a moving drop within a tube. Theoretical work on the flow of spheres shows lateral migration of the sphere due to inertial wall effects [12, 13, 14]. In 1965 Saffman [12] utilized matched asymptotic expansions for simple shear flow. His study showed the wall effects produced a migration of the sphere away from the centerline of the tube and towards the wall. The linearity of the Stokes equations can not produce a force in the lateral direction, and therefore this migration must be caused by inertial effects. This migration of spheres was further shown by the 1974 study of Ho and Leal [13]. Ho and Leal calculated rigid particle trajectories with asymptotic expansions

for simple shear flow and Poiseuille flow. They determined the migration force pushed the spheres to an equilibrium distance between the centerline and the wall. This force is stronger near the wall than near the centerline. Therefore a suspension of particles will preferentially concentrate in the area between the centerline and the equilibrium point, and leave the area near the wall with a small particle concentration. Magnaudet et al [14] added this migration effect in the determination of drop deformation. They obtained leading order expressions for drag and lift forces for a deformable drop near the tube wall. Equations were developed for the drag, deformation, inertial lift, and the deformation induced lift on the drop.

Including these effects into the deformation of drops requires simulations at finite Reynolds numbers. A 1984 work by Ryskin and Leal [15] and a 1989 work by Dandy and Leal [16] utilized a finite difference technique to model the buoyancy-driven motion of bubbles and drops respectively for a wide range of Reynolds and Weber numbers. Both of the works were for an infinite domain, however the results show a variety of deformations and the inertial terms effect on drop shape. In [16] the drop deformation became a spherical cap as Weber number increased at low Reynolds number. At high Reynolds numbers, the drop became a disc as Weber number increased. These were the same shapes found for bubbles in [15]. Another important finding of this work was a recirculating wake behind the drop that was detached from the drop itself. Changing parameters, such as viscosity

ratio, changed the distance between the drop and the wake, however, over the values studied, the wake was never in contact with the end of the drop. A 1997 work by Bozzi et al. [17] followed up on these works and developed a finite element method to model buoyancy-driven drop motion within a tube. For the simulations at intermediate Reynolds numbers, deformation grew with increasing Reynolds numbers. The work also found the same recirculation zone behind the drop as in [16].

Besides the basic problem of a single drop within a tube, other theoretical studies have looked into the effect of deformation. In 1999, Davis [18] studied the effect of a trailing drop on a rising drop. Using a boundary integral method, Davis showed the conditions necessary for the drops to separate, and under what conditions the drops would coalesce. A similar study on coalescence of deformable drops was done in 1997 by Rother et al. [19]. In this work, matched asymptotic expansions were done along with a boundary integral method to describe the draining of fluid between the drops. Further studies have also examined deformation involving some non-Newtonian fluids. In 1979, Chan and Leal [20] modeled migration of a deformable drop in a shear flow of a second order fluid, and in 1999, Toose et al. [21] utilized a boundary integral formulation to model a viscoelastic drop within a Newtonian fluid. Both studies showed similar deformation for non-Newtonian fluids as in Newtonian. In [20], the study only considered Poiseuille and Couette flows, while [21] only simulated the drop as a non-Newtonian fluid and the

surrounding fluid as Newtonian.

2.1.2 Pressure-Driven Motion

In the preceding section, the suspending fluid remains motionless without the presence of the drop. For the pressure-driven motion, the drop is within a flow field created by a pressure difference across the pipe. The cross sections far away from the drop have a velocity field and pressure distribution corresponding to Poiseuille flow in a pipe. In cylindrical coordinates, the dimensionless velocity and pressure are given by:

$$\bar{v} = 2(1 - r^2) \quad (2.3)$$

$$\frac{\partial \bar{P}}{\partial z} = -8 \quad (2.4)$$

where r and z are the radial and axial coordinates respectively. Equations 2.3 and 2.4 are the analytical solution of the equations of motion for pressure-driven flow in a pipe. The presence of the drop within this flow field not only affects the velocity field near the drop, but also the overall pressure drop within the pipe. Thus the extra pressure loss due to the presence of the drop is a measurable quantity in these problems along with the velocity and deformation of the drop.

Since this type of problem has applications in areas such as oil recovery and blood flow in capillaries, there are several experimental and theoretical studies on the pressure-driven motion of drops in tubes. On the theoretical side, a study by

Hetsroni et al. [22] solved for the flow field in and around a single spherical droplet or bubble within a Poiseuille flow. The work solved a function for describing the deviation of the interface from a spherical shape and presented an iterative procedure to obtain the higher order flow fields and drop shapes. Computational work has also been carried out on the problem via several studies utilizing a boundary integral calculation [23, 24, 25, 26]. The work of Martinez and Udell in [23] studied the effect of a variety of parameters on deformation of the drop and extra pressure loss for the system. Using a boundary integral method to solve the equations of motion, they varied the drop size, viscosity ratio, and capillary number. The results showed an increase in deformation with increasing capillary number and increasing viscosity ratio. The extra pressure loss and drop speed for their study compared well with the previous experimental data of Ho and Leal [27].

Coulliette and Pozrikidis [24] also modeled pressure-driven flow at small Reynolds numbers with a boundary integral calculation. The study looked at the motion and deformation of an array of drops moving within the flow field. The results showed that deformations were caused not only by pressure-driven flow, but also by the drops interacting with each other. While the work of Johnson [25] and Johnson and Borhan [26] focused mainly on the effects of surfactant on the problem, simulations were run for clean drops, drops with no surfactant, as well. The study was able to produce drop shapes as a function of time and show the mechanisms leading to drop breakup at or above a critical capillary number. This was the value of the

capillary number above which a steady drop shape was not found. The simulations allowed the determination of this critical capillary number and compared with the results found experimentally by Olbricht and Kung [28]. Last, Zhou and Pozrikidis [29] utilized an improved boundary integral method, called the method of interfacial dynamics, to simulate pressure-driven flow of suspensions. The results showed the drops migrated towards the centerline of the channel for all parameter values.

On the experimental side, in 1975 Ho and Leal, [27] studied the motion of neutrally buoyant drops. The experiments were carried out using both Newtonian and viscoelastic suspending fluids over a range of size and viscosity ratios. Besides the deformed shape, the study showed the effect the parameters had on the extra pressure loss of the system and drop speed. The work also pointed out the observed differences between the Newtonian and viscoelastic fluids. Some of these differences included a transition in the shape of drops and altering the trends in the extra pressure loss. The experimental data agreed well with previous theoretical work. Another experimental work was carried out by Olbricht and Kung [28], which also provides a good review of previous experimental and theoretical studies of pressure driven motion of drops in tubes. In the work of Olbricht and Kung [28], drop deformation and breakup was studied experimentally. It was observed that breakup would occur when the system was above a critical value of the capillary number defined as $Ca = \frac{\mu U}{\sigma}$. The μ is the viscosity of the suspending fluid, U is the characteristic velocity of the flow, and σ is the surface tension. The critical

capillary numbers were found for a variety of size and viscosity ratios. The values increased for decreasing viscosity and size ratios.

The work of Borhan and Pallinti in 1998 and 1999 [30] and [31] studied the effect of added buoyancy to the pressure-driven flow for low Reynolds numbers. The experimental studies provided drop shapes and velocities as well as critical capillary numbers for a range of density, viscosity, and size ratios. Besides the values, the work also found different mechanisms for the breakup of drops within the pressure-driven flow. Some deformations found from the experiments are shown in Figure 2-3

Instead of just elongating, the drops flattened on the centerline at the rear of the drop. The experiments determined four different modes of breakup; formation and growth of capillary waves at the interface, transient stretching in the axial direction, tail-streaming, and penetration of a re-entrant cavity at the trailing end of the fluid particle. The modes of breakup varied depending on the system and also effected the critical capillary number. However the work found that the critical capillary number decreased with increasing particle size regardless of the mode of breakup.

The previous studies looked at deformation and found the conditions necessary for drop breakup at low Reynolds numbers. The effect of inertia on drop

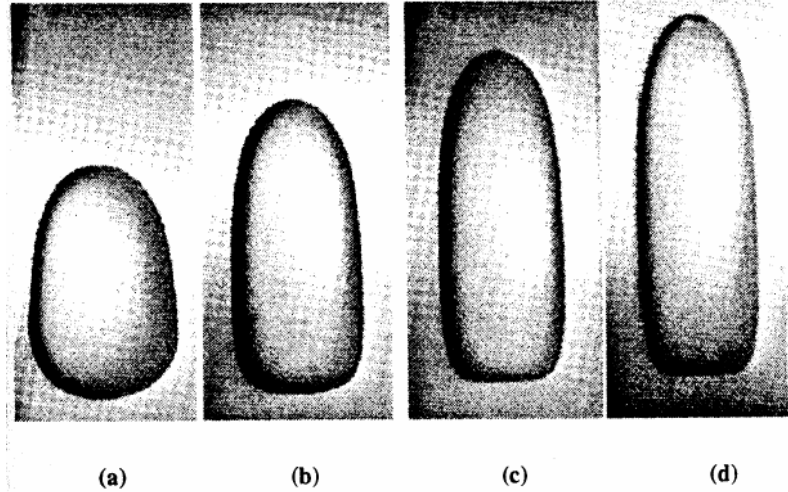


Figure 3.9 Comparison of the steady shapes for a drop size of $\kappa=0.91$ in the CW3-1 experiments ($Bo=4.1$, $\lambda=0.22$) for different capillary numbers; (a) $Ca=0.0$, (b) $Ca=0.27$, (c) $Ca=0.54$, (d) $Ca=0.75$.

Figure 2-3. Drop shapes from Borhan and Pallinti [30]

deformation and critical capillary number still remains to be determined.

2.1.3 Temperature-Driven Motion

Drop motion in the previous two sections is driven by body forces on the drop. The surface tension on the interface determines the shape of the drop. For temperature-driven motion, an external temperature gradient induces a surface tension gradient that drives the flow. This motion is created by the tangential

component of the stress jump across the interface given by Eq: 2.5

$$(\mathbf{I} - \mathbf{nn}) \cdot \nabla \sigma \quad (2.5)$$

where σ refers to the surface tension, \mathbf{I} is the identity tensor, and \mathbf{n} is the surface normal. This temperature-driven or "Marangoni" flow is more prevalent in micro-gravity conditions where gravitational forces do not dominate the smaller surface forces. A complete review in the area of thermocapillary motion can be found by Subramanian and Balasubramaniam [32]. The present work is focused on the areas of buoyancy-driven and pressure-driven motions of drops. It is possible the present work could be utilized to model temperature-driven motion as well. For the sake of completeness, a few examples of thermocapillary studies are discussed below.

A work by Haj-Hariri et al. [33] simulated thermocapillary flow due to constant temperature gradient. It was found that drop deformations slowed the drop due to a reduction in surface temperature gradient. The deformations were found to be axisymmetric and the steady drop shape elongates to an oblate spheroid. Other studies have focused on the motion of multiple drops undergoing thermocapillary motion. Rother et al. [34] utilized a boundary integral method to model the motion of two drops. The study was able to calculate trajectories for the drops and showed the inhibiting effect small deformations have on coalescence. The

work of Berejnov et al. [35] also employed the boundary integral technique for thermocapillary motion of several drops. When the two drops were the same size, the drops approached each other. However for unequal drops, with the larger one leading, the drops separated due to the deformation effect on the velocity field.

The work described in the previous sections show the importance deformation has on the flow fields regardless of the driving force behind the flow. Any simulation modeling these flow problems needs to accurately define the deformation to reach the correct solution. The next sections describe the mathematical techniques used in previous works to capture the interface as well as the technique used in this thesis.

2.2 Mathematical Techniques

The difficulty in solving two-phase problems involves the boundary conditions needed at the interface between the phases. Accurately computing the effect of the interface requires knowledge of the interface normals, curvature, and position to allow the implementation of the boundary conditions at the correct location in space. There have been several techniques utilized to track the interface, the two major ones are the Volume of Fluid (VOF) method and the use of a Level Set function. Both of these methods have advantages and limitations such that a hybrid of the two methods has been developed to capitalize on the good points of each method. The following sections discuss each method and the details of their

combination.

2.2.1 Volume of Fluid

Some early work in the area of multiphase flows utilized a technique called the Marker-and-Cell method [36, 37, 38]. This method notated computational cells that contained the fluid or the interface. However, to solve the equations of motion, interpolation at the interface cells is required and adds significant computation time. Other methods used marker particles to follow the flow, another intense computation, or line segments which are difficult to match at the cell boundaries. Due to these drawbacks, Hirt and Nichols developed the Volume of Fluid method or VOF [39]. Their work outlines the previous methods used for free boundary problems and the difficulties of those methods. The new VOF method defines a value for each computational cell corresponding to the amount of fluid contained within the cell. Cells with a value of unity are completely full, while zero values correspond to empty cells. Any cell with a fractional value of α , the VOF function, contains the interface. As a note, a cell with $\alpha = 1$ still contains the interface if a neighboring cell has a zero value of α . The VOF function is updated in time according to the donor/acceptor method to stop smearing of the interface. In this method, the amount of fluid leaving a cell with $\alpha > 0$ is calculated based on the velocity at that cell. This fluid amount is the exact amount used in calculating the new α values of the donor cell losing the fluid, and the acceptor cell that gains

the fluid. Thus the motion of the interface is accomplished by conserving mass without needing the exact location of the interface. The normals of the interface are calculated by the position derivatives of α as in Eq. 2.6

$$n_i = \frac{\partial \alpha}{\partial x_i} \quad (2.6)$$

Using a variable mesh scheme, Hirt and Nichols implement this technique in simulation of several different free boundary problems. These problems included a broken dam, undular bore, breaking bore, and a Rayleigh-Taylor instability. Their code matched the experimental results for each of the four.

Other studies have further utilized this method. Janse et al. [40] extended the VOF for spherical coordinates. This work used the donor/acceptor method to move the interface. Also the pressure condition at the boundary was solved using a free surface pressure equation along with the pressure Poisson equation. Utilizing finite difference for the derivatives, the group derived the mathematical technique necessary for spherical coordinates. Renardy et al. [41] developed an algorithm using VOF to implement a linear equation of state for a surfactant. They used the concentration of surfactant within an expression for a body force on the fluid. This method was implemented in the simulation of drops undergoing shear, providing the group the concentration profile of surfactant on the surface of the drop as well as the drop shape. Their results showed tipstreaming as well as areas

of negative surface tension due to the linear equation of state. Jeong and Yang, [42], applied the VOF method and an adaptive grid with a finite element method to study transient flows. They solved the VOF equation with finite element rather than finite difference, employing an adaptive grid to place smaller elements in the area of the interface. The free surface shape is predicted based on the shape of the elements in a filling pattern technique. The VOF function is not continuous due to the discrete values within each cell. The transitions between cells are jumps in VOF values, so the group needed to implement a smoothing technique. The method simulated radial flow with a point source and the collapse of a dam. The simulation results matched the theoretical results for the flows. While there has been some success with the VOF method, work has been done to reduce the limitations of the method, namely the inaccuracies in calculating the normals.

The donor/acceptor method of Hirt and Nichols [39] moved fluid out of cells without regard for the position of the interface within that cell. In a work by Gueyffier et al. [43], a new version of the VOF method is developed to track the interface, the piecewise linear interface calculation (PLIC). With this calculation, the normals of the interface are still calculated based on position derivatives of the VOF function. However these normals are used to create a line within the interface cell. The line has a slope based on the normals and is positioned such that the area bounded by it equals the VOF of the cell. When the donor/acceptor method moves the interface, the line segment helps determine the amount of fluid

advanced. Gueyffier et al. validated this algorithm by matching bubble rise tests with experimental results. Harvie and Fletcher [44] also implemented this PLIC in a new advection scheme called the defined donating region scheme. In this scheme, a donating region is defined in the cells based on fluid velocities to calculate the boundary fluxes for each boundary. The surface is reconstructed with the PLIC and any fluid in the cell within the donating region is moved to the neighboring cells. The work tested various VOF methods on sample problems to calculate the error function for each method. The results showed the largest error for Hirt and Nichols' original method, and an improvement of an order of magnitude for this new defined donating region scheme. All of the techniques showed a smearing of the interface, however Hirt and Nichols method also had an increase in area of fluid that was eliminated in the new method. A work by Kim et al. [45] used a different technique. They developed a first-order convection model for the VOF. For three-dimensional space, the model calculates the normals and selects a base plane. This base plane determined coefficients for a VOF distribution function that calculated the convective fluxes of the cell. This distribution function lead to better results than the donor cell method. Rider and Kothe [46] took this one step further by developing a second order accurate method. In this method, geometric terms are utilized to estimate the volume fluxes. The results of the method reduced the error in test problems at least one order of magnitude over previous VOF techniques.

The Volume of Fluid method is a powerful technique to track the interface since

a small amount of information needs to be saved each time step. The method has limitations due to the discrete nature of the VOF function leading to mathematical difficulties in calculating derivatives. Also, the inaccuracy in surface normals arise from the fact that the method is simulating a real interface by a series of line segments. This error could be overcome by reducing the grid size so that line segments can become a curved interface. However, this makes the problem more computationally intensive, just as some of the corrections in the works cited above do. This addition of computation time eliminates any benefits from the simple nature of the original method. Therefore, a better method for calculating surface normals needs to be developed.

2.2.2 Level Set Function

In response to the problems of the VOF method calculation of the surface normals and curvature, Osher and Sethian [47] developed a method to track the interface using a Level Set function, ϕ . As in the VOF method, an explicit equation for the interface is not required, so the method does not keep track of the exact interface position. Instead the Level Set function, ϕ , is defined as the normal distance a point is away from the interface. Thus ϕ is a continuous smooth function unlike the VOF function which has large jumps near the interface. For bookkeeping purposes, the distances inside the interface have a negative ϕ value, points outside the interface are positive, and the interface is where $\phi = 0$. Since ϕ is a distance

function, the normals to the interface can be calculated by Eq. 2.7 and 2.8:

$$n_x = \frac{\partial \phi}{\partial x} \quad (2.7)$$

$$n_y = \frac{\partial \phi}{\partial y} \quad (2.8)$$

This Level Set function is updated in time using the advection equation, Eq. 2.9:

$$\frac{\partial \phi}{\partial t} + (\mathbf{u} \cdot \nabla) \phi = 0 \quad (2.9)$$

where \mathbf{u} is the velocity field. In their work, Osher and Sethian were able to utilize the Level Set function in computing the solution of a variety of moving front problems.

While Eq. 2.9 moves the $\phi = 0$ level set exactly as the interface moves, the rest of the level sets do not automatically follow this equation. Therefore, the use of this equation for all of ϕ causes it to no longer be a distance function. These distortions can lead to large errors in calculating the fluid and interface properties. Also Eq. 2.9 moves the interface without any regard for mass conservation, causing a loss or gain of mass in the problem. Several studies have been done to provide corrections to the Level Set method to reduce these problems. Puckett et al. [48] provides a review of the work done on both the Level Set and the VOF techniques. One of the studies done to improve the Level Set was carried out by Sussman et

al. [49]. To reduce the loss of mass and to keep ϕ a distance function, the group moved the Level Set using Eq. 2.9, then reinitialized ϕ around the zero level set using $|\nabla\phi| = 1$. This is accomplished using equation 2.10:

$$\frac{\partial\phi}{\partial\tau} = S(\phi)(1 - |\nabla\phi|) \quad (2.10)$$

where S is the sign function. Equation 2.10 is iterated until steady state values for ϕ are reached. This method was used to simulate the 2D motion of air bubbles in water and water drops in air. For the simulations without keeping ϕ a distance function, a loss of mass of over 40 percent was seen in some problems. When the reinitializing was done for each time step, mass is conserved, and the results match expected steady state shapes and velocities.

Besides keeping ϕ a distance function, this method also maintains a sharp interface with a finite thickness. To incorporate the surface tension into the equations of motion, a continuum model developed by Brackbill et al. [50] is utilized. In this model, the interface is not a sharp line, but rather a transition region of finite thickness between the two fluids. The fluid properties such as density and viscosity are smoothed functions in the region to eliminate large derivatives. This modeling of the interface alters the normal stress boundary condition from a surface force to a body force. The body force is incorporated as an extra force into the conservation of momentum equations, thus eliminating the need to locate the interface and

apply the boundary condition. Since the interface begins with a finite thickness, the motion of the Level Set function needs to keep the size of the interface from spreading and becoming physically unrealistic. Therefore, maintaining ϕ as a distance function not only helps in mass conservation, but also is needed to implement the continuum model of surface tension.

A study by Chang et al. [51] further used reinitializing for ϕ to overcome the limitations of the Level Set method. Along with the method of Sussman et al. [49] to maintain ϕ as a distance function, the group also utilizes a mass conservation reinitializing procedure which conserves mass to a set tolerance. Simulations were done on a variety of problems showing the model conserves mass and keeps the interface at a constant, finite thickness. The group also compared different numerical techniques and found a second order ENO scheme was more robust than a centered difference scheme especially for a large density ratio. Another study by Kaliakatsos and Tsangaris [52] utilized this Level Set method with reinitializing to model deformation of drops in pipes. Using a second order projection method to solve the momentum equations, the group calculated the drop shapes and speeds for variety of parameters. The results compared well with the earlier experimental work on deforming drops.

The effectiveness of the previous studies on modeling two-phase flows with the Level Set function show the accuracy of this technique in calculating the curvature of the surface. However the difficulties in mass conservation require a large com-

putational effort to overcome. While the methods used by previous groups reduce the error, the iterations required to accomplish the reinitializing are much larger than the simple motion of fluid in the VOF method. Consequently, a method that combines the best features of the VOF and the Level Set is a more efficient and accurate way of simulating a two-phase flow.

2.2.3 Hybrid VOF/Level Set Method

The previous sections have described the advantages and limitations of both the VOF and Level Set methods. To combine the best parts of the methods, a hybrid VOF/Level Set method has been developed. For this hybrid method, the interface is modeled using the VOF and Level Set functions. The first step is to initialize the grid with the VOF function for the required initial conditions. The interface is reconstructed in each cell as in the piecewise linear interface calculation (PLIC). After the interface is determined, the level set function can be calculated by determining the normal distance of each grid point from the interface. The level set is used to determine the normals and curvature of the interface required for the surface tension force. The velocity field is determined by solving the conservation of momentum equations including the surface tension term. Once the velocity field is obtained, the interface is moved by updating the VOF function for each cell, using the new velocities and conservation of mass. The new VOF values are used to reconstruct the interface and the process repeated until steady state is reached.

Thus the level set is used to determine the curvature of the interface, a weakness of the VOF method, while the interface motion is accomplished using the VOF function conserving mass unlike in the Level Set technique.

Several studies have used this hybrid method to model two-phase flows [53, 54, 55]. A study by Sussman and Puckett [53] tested the effectiveness of the hybrid method versus the VOF or Level Set method alone for two-dimensional, axisymmetric, and three-dimensional flows. The study found the hybrid method produced results equal to or better than any other method. When the interface develops corners, the hybrid method is particularly efficient over the Level Set method which can lose up to 20 percent of mass, while the hybrid only loses a fraction of a percent of mass. In moving the interface, the hybrid method is able to match the best VOF methods, and outperforms these methods in problems involving surface tension. In 2002, Son and Hur [54] utilized the hybrid method for buoyancy-driven motion. The study modeled the axisymmetric problems of rising bubbles in a liquid, and liquid drops falling in a gas. The algorithm moves the interface using operator splitting, and advects the level set function and VOF function at the same time. This allows the level set function to be reinitialized as a distance function, as well as conserving mass using the VOF function. In solving the momentum equations, the inertial terms are calculated using cubic interpolated propagation, and second order central difference is used for the rest of the derivatives. The numerical results of the study conserve mass within a 0.01

percent error. Son continued the work in 2003 [55] by expanding the work from the axisymmetric case to the three dimensional case for rising bubbles and droplets adhering to a wall. The algorithm utilized the method outlined in the previous work and the results were able to obtain the same accuracy in conserving mass.

The previous studies show the effectiveness of the hybrid method in simulating two-phase flow problems. The work presented in this thesis is to develop a similar algorithm based on the hybrid method. Once developed, the algorithm will be tested for the system of a single drop within another fluid in a confined domain. The analytic and experimental results for this system are used to confirm the accuracy of the algorithm. The written code for the simulation is generalized to allow both buoyancy-driven and pressure-driven motion of the drop, as well as allowing non-Newtonian power law fluids. A series of simulations are carried out to determine the effect of Reynolds number, Capillary number, viscosity ratio, and non-Newtonian character of the suspending fluid for both buoyancy-driven and pressure-driven motion of the drop. Thus the algorithm matches previous work and gives insight and predictions into experimentally difficult systems.

Problem Formulation and Solution

Procedure

In this section, a detailed mathematical description is given for buoyancy driven and pressure driven two-phase flows in a confined domain. The governing fluid mechanics are presented along with the specific modified equations used in this work. Next, the hybrid VOF/Level Set Method for defining and moving the interface is described. The final section discusses the numerical techniques implemented in solving the fluid and surface mechanical equations to arrive at the steady state solution.

3.1 *Governing Equations*

Modeling any physical system requires some method of observable physical properties prediction. In this work, a set of equations exists which govern the fluid properties and the surface properties of the system of interest. These equations are presented in the following sections.

3.1.1 Fluid Mechanics

Consider the motion of a deformable drop or bubble suspended in a second phase within a tube as shown in Figure 3-1. The exterior and interior bulk phases (denoted by D and D' respectively) are assumed to be incompressible with corresponding densities ρ and ρ' , where all prime quantities refer to interior phase properties. Equations are made dimensionless using variable characteristic scales. All lengths use the tube radius R_o , velocities with a characteristic V , stresses with $\frac{\mu_o V}{R_o}$, and time with $\frac{R_o}{V}$, where μ_o is the low-shear viscosity of the exterior fluid. The characteristic velocity V is taken to be the average velocity of the bulk fluid in the case of pressure-driven motion, and $\frac{(\rho - \rho')gR_o^2}{\mu_o}$ in the case of buoyancy-driven motion, where g is the magnitude of the gravitational field. The velocity scaling is derived from balancing the viscous and gravitational forces.

The dimensionless equations governing the incompressible flow field in the two bulk phases (in the absence of thermal or surfactant effects) are given by Eq. 3.1

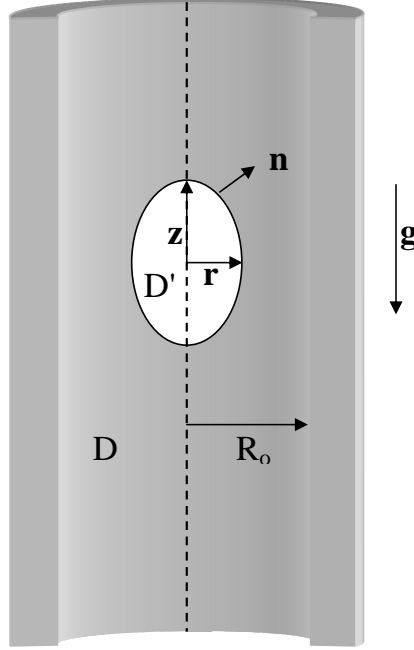


Figure 3-1. Schematic of two-phase flow within a tube

and Eq. 3.2:

$$\frac{D\mathbf{u}}{Dt} = -\frac{1}{Re}[\nabla p - \nabla \cdot \boldsymbol{\tau}] + \frac{1}{Fr}e_g \quad , \quad \nabla \cdot \mathbf{u} = 0 \quad in \ D \quad (3.1)$$

$$\frac{D\mathbf{u}'}{Dt} = -\frac{1}{\gamma Re}[\nabla p' - \nabla \cdot \boldsymbol{\tau}'] + \frac{1}{Fr}e_g \quad , \quad \nabla \cdot \mathbf{u}' = 0 \quad in \ D' \quad (3.2)$$

where the stress tensor $\boldsymbol{\tau}$ is related to the velocity gradient tensor through a power-law constitutive relation. In the above equations, u represents the velocity field, e_g is the unit vector in the direction of the gravitational field, and γ denotes the ratio of the density of the interior phase to that of the exterior phase. The Reynolds and Froude numbers are defined as $Re = \frac{\rho_o V R_o}{\mu_o}$ and $Fr = \frac{V^2}{g R_o}$, respectively. The

Reynolds number relates the importance of the viscous to inertial forces, while the Froude number relates the gravitational to inertial forces. These equations are complemented by the no-slip condition on the tube wall, and a prescribed velocity distribution (e.g., the single phase velocity profile in the case of pressure-driven motion and zero velocity in the case of buoyancy-driven motion) on inflow and outflow boundaries far away from the drop. The stress conditions on the wall and outflow are derived from the governing equations, and are predetermined on the inflow. The boundary conditions on the drop surface, $\mathbf{x} = \mathbf{x}_s(t)$, consist of the dynamic and kinematic conditions, Eq. 3.3, 3.4, and 3.5:

$$\mathbf{u} = \mathbf{u}' \quad (3.3)$$

$$\frac{d\mathbf{x}_s}{dt} = \mathbf{u} \quad (3.4)$$

$$(p' - p)\mathbf{n} + \mathbf{n} \cdot (\boldsymbol{\tau} - \boldsymbol{\tau}') = \frac{1}{Ca}(\nabla_s \cdot \mathbf{n})\mathbf{n} \quad (3.5)$$

where $\nabla_s = (I - nn) \cdot \nabla$ is the surface-gradient operator, n is the unit normal vector on the drop surface directed into D , and the capillary number is defined as $Ca = \frac{\mu_o V}{\sigma}$, with σ denoting the interfacial tension between the two phases.

Using an algorithm developed by Haj-Hariri et al [33], which combines the best features of the volume-of-fluid (VOF) method of Hirt and Nichols [39] with Level Set based approaches described in section 2.2.2. The algorithm is suitable for the treatment of flows driven, or affected by, interfacial forces, and has the following

characteristics:

- Capable of treating two- and three-dimensional incompressible flows
- Implements automatic adaptive grid refinement near the interface
- Uses the Level-Set formulation of Osher and Sethian [47] to calculate surface topology (e.g., curvature), location (tracking), and the normal distance to the interface
- Treats interfacial forces as body-forces in the momentum equations multiplied by a surface Dirac delta function which reduces number of equations

Schematically, the non-dimensional governing equations in the entire region containing both bulk fluids and the interface are rewritten as Eq. 3.6 and 3.7:

$$\frac{D\rho}{Dt} + \nabla \cdot \bar{u} = 0 \quad (3.6)$$

$$\bar{\rho} \left(\frac{\partial \bar{u}}{\partial t} + \bar{u} \cdot \nabla \bar{u} \right) = \frac{1}{Re} (-\nabla P + \nabla \cdot \bar{\bar{\tau}}) + \bar{F} \quad (3.7)$$

The force in equation 3.7 is calculated using Eq. 3.8:

$$F = \frac{1}{Re} |\nabla \phi| \bar{n} \nabla \cdot \bar{n} + \frac{1}{Fr} \bar{g} \quad (3.8)$$

The force defined by Eq. 3.8 is a body force derived to replace the stress condition Eq. 3.5. To better understand this derivation, consider a control volume around

the interface as shown in Figure 3-2.

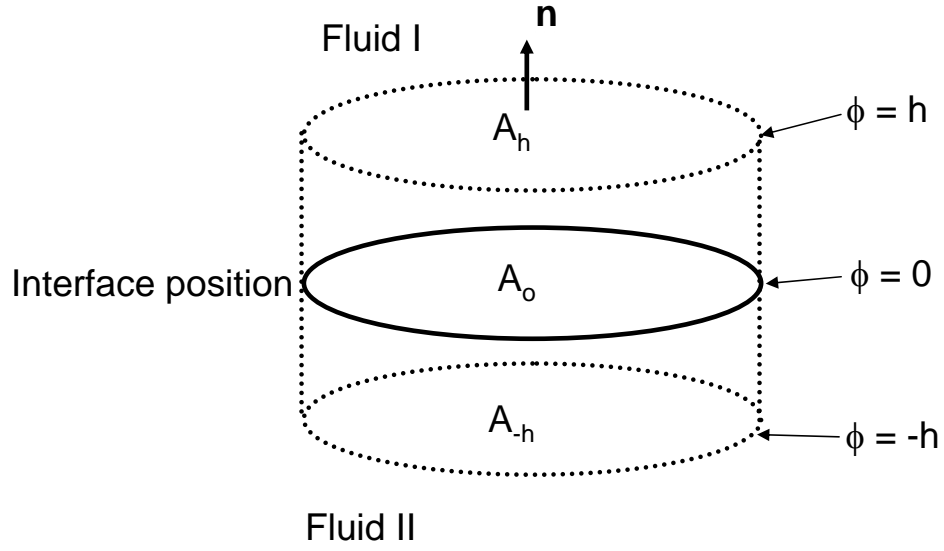


Figure 3-2. Control volume near the interface

If the case of $Re = 0$ is considered, the conservation of momentum is given by Eq.

3.9

$$\nabla \cdot \overline{\overline{T}} + \overline{F} = 0 \quad (3.9)$$

where $\overline{\overline{T}}$ is a stress tensor combining both the pressure term and the typical $\overline{\tau}$ term. The force term \overline{F} is a body force that can be written in terms of a smeared surface tension force according to Eq. 3.10.

$$\overline{F} = \overline{f} \delta(\phi) = -\sigma \overline{n} \nabla \cdot \overline{n} \delta(\phi) \quad (3.10)$$

Integrating Eq. 3.9 over the control volume $dV = dAd\phi$ produces Eq. 3.11.

$$\int_V (\nabla \cdot \bar{\bar{T}} + \bar{F}) = 0 \quad (3.11)$$

Using the divergence theorem, substituting terms, and simplifying produces the following equations:

$$\int_{A(h)+A(-h)+A(sides)} \bar{n} \cdot \bar{\bar{T}} dA + \int_{A(o)} \int_{-h}^h \bar{F} dAd\phi = 0 \quad (3.12)$$

$$\int_{A(h)+A(-h)+A(sides)} \bar{n} \cdot \bar{\bar{T}} dA + \int_{A(o)} \int_{-h}^h \bar{f} \delta(\phi) d\phi dA = 0 \quad (3.13)$$

$$\int_{A(h)+A(-h)+A(sides)} \bar{n} \cdot \bar{\bar{T}} dA + \int_{A(o)} \bar{f}|_{\phi=0} dA = 0 \quad (3.14)$$

The integration between equations 3.13 and 3.14 is possible due to the δ function only having values near the zero Level Set ($\phi = 0$). The limit of equation 3.14 is taken as $h \rightarrow 0$, thus causing $A(sides) \rightarrow 0$ and $A(h) \rightarrow A(-h) \rightarrow A(o)$. Therefore equation 3.14 becomes

$$\int_{A(h)+A(-h)} \bar{n} \cdot \bar{\bar{T}} dA + \int_{A(o)} \bar{f} dA = 0 \quad (3.15)$$

Simplifying produces

$$\int_{A(o)} \bar{n} \cdot (\bar{\bar{T}}^I - \bar{\bar{T}}^{II}) dA + \int_{A(o)} \bar{f} dA = 0 \quad (3.16)$$

$$\bar{n} \cdot (\bar{\bar{T}}^I - \bar{\bar{T}}^{II}) = -\bar{f} = \sigma \bar{n} \nabla \cdot \bar{n} \quad (3.17)$$

Equation 3.17 shows the smearing of the surface force \bar{f} into a body force \bar{F} is equivalent to solving the stress condition at the interface. Now that the force term is derived, the rest of the terms in the conservation of momentum are explained below.

The stress tensor is defined by Eq. 3.18:

$$\bar{\bar{\tau}} = \bar{\mu} (\nabla \bar{u} + (\nabla \bar{u})^T) \quad (3.18)$$

The density and viscosity in the momentum equation and definition of the stress tensor are not the fluid specific properties as usual. Instead they are position dependent functions, which can be calculated at each grid point by Eq. 3.19:

$$D = \lambda \alpha + (1 - \alpha) \quad (3.19)$$

In equation 3.19, D is the property ($\bar{\rho}$ or $\bar{\mu}$) and λ is the ratio of the internal property to the external property. The α in the equation refers to the position dependence and can be determined from either the VOF function or the Level Set

function.

Solving these equations in an r-z axisymmetric coordinate system gives Eq. 3.20, 3.21, and 3.22:

$$\frac{1}{r} \frac{\partial}{\partial r} (rU) + \frac{\partial V}{\partial z} = 0 \quad (3.20)$$

$$\bar{\rho} \left(\frac{\partial U}{\partial t} + U \frac{\partial U}{\partial r} + V \frac{\partial U}{\partial z} \right) = \frac{1}{Re} \left[-\frac{\partial P}{\partial r} - \frac{1}{r} \frac{\partial}{\partial r} (r\tau_{rr}) + \frac{\tau_{\theta\theta}}{r} - \frac{\partial \tau_{rz}}{\partial z} \right] + \frac{1}{We} |\nabla \phi| n_r (\nabla \cdot n) \quad (3.21)$$

$$\bar{\rho} \left(\frac{\partial V}{\partial t} + U \frac{\partial V}{\partial r} + V \frac{\partial V}{\partial z} \right) = \frac{1}{Re} \left[-\frac{\partial P}{\partial z} - \frac{1}{r} \frac{\partial}{\partial r} (r\tau_{rz}) - \frac{\partial \tau_{zz}}{\partial z} \right] + \frac{1}{We} |\nabla \phi| n_z (\nabla \cdot n) + Fr g \quad (3.22)$$

U and V are the r and z components of velocity, ϕ is the Level Set function described in the next section, Re is the Reynolds number, and We is the Weber number. The Weber number is the ratio of inertial force to surface tension force. The conservation of mass, Eq. 3.20, reduces to this simple form since the material density does not change with time so the material derivative of density is equal to zero.

3.1.2 Surface Equations

In the hybrid method, the surface is defined by the Level Set and VOF functions. The Level Set function is the normal distance each grid point is away from the interface. Since the Level Set is a distance function, the normals and shape of the surface can be determined from it. However the surface is moved using the

VOF function, because it is defined by the amount of inner fluid in each cell and the motion of these volumes is a simple conservation of mass calculation. The following method is used to define the Level Set in terms of the VOF to allow shape calculation and interface motion.

The value of the VOF is assumed to be an area, α . Original normals can be calculated by taking the position derivatives of the VOF function. Using the area and the normals, a line segment can be constructed to simulate the interface. The slope of the line comes from the normals, and the line encloses an area equal to α . The important values of the lines are the midpoints x_c and y_c . Different combinations of areas and normals can all be classified into three separate cases, each with its own equation to determine the midpoints. The three cases and their limits are displayed in Figure 3-3.

For the three cases, n_1 is the larger absolute value of the two normals, and the midpoints are calculated for case 1, 2, and 3 by Eq. 3.23, 3.24, and 3.25:

$$(\overline{x_c}, \overline{y_c}) = \sqrt{\frac{n_2}{2n_1}} \alpha, \sqrt{\frac{n_1}{2n_2}} \alpha \quad (3.23)$$

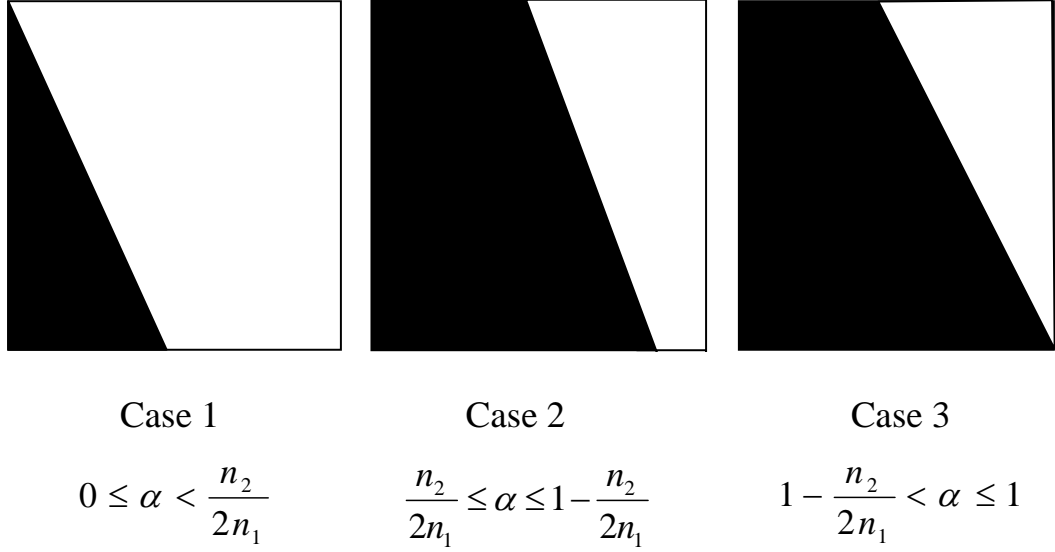


Figure 3-3. Three cases for determining midpoint for VOF

$$(\overline{x_c}, \overline{y_c}) = \alpha, \frac{1}{2} \quad (3.24)$$

$$(\overline{x_c}, \overline{y_c}) = 1 - \sqrt{\frac{n_2}{2n_1} (1 - \alpha)}, 1 - \sqrt{\frac{n_1}{2n_2} (1 - \alpha)} \quad (3.25)$$

After determining the midpoint values, the Level Set values are calculated for the corners of the computational cell by Eq. 3.26, 3.27, 3.28, and 3.29:

$$\phi_{i,j} = [(0 - x_c)n_x + (0 - y_c)n_y]\Delta \quad (3.26)$$

$$\phi_{i+1,j} = [(1 - x_c)n_x + (0 - y_c)n_y]\Delta \quad (3.27)$$

$$\phi_{i,j+1} = [(0 - x_c)n_x + (1 - y_c)n_y]\Delta \quad (3.28)$$

$$\phi_{i+1,j+1} = [(1 - x_c)n_x + (1 - y_c)n_y]\Delta \quad (3.29)$$

The Δ in equations 3.26 thru 3.29 is the computational cell length used to scale the distance from the midpoint. Each cell corner is part of four cells, so each corner has four different values for the Level Set function. To obtain the true value for each point, the smallest absolute value of Level Set is used. Therefore the Level Set function is calculated for all the cells with VOF values between 0 and 1. The Level Set in the other cells is determined by using Eq. 3.30:

$$\frac{\partial \phi}{\partial \tau} = -sgn(\phi)[1 - |\nabla \phi|] \quad (3.30)$$

The equation is iteratively solved until $|\nabla \phi| = 1$, and the Level Set function is determined for the entire computational domain [47].

Once the Level Set function is obtained, the normals and curvature of the drop can be calculated. The normals are defined by Eq. 3.31 and 3.32:

$$n_x = \frac{\partial \phi}{\partial x} \quad (3.31)$$

$$n_y = \frac{\partial \phi}{\partial y} \quad (3.32)$$

The curvature is determined by the divergence of the normals. Using the normals, and the curvature, the surface tension force can be used to solve the momentum balance.

3.2 *Numerical Method*

Once the problem is defined by the governing equations and corresponding boundary conditions, a solution procedure is implemented to numerically solve for the desired data. The solution procedure has two important areas; the technique to determine the velocity and pressure fields controlled by Eq. 3.20, 3.21, and 3.22, and the use of the hybrid VOF/Level-Set method to determine the surface force and move the interface. The next sections describe the numerical techniques used and how the solution procedure is implemented.

3.2.1 General Solution Procedure

Due to the complexity of the equations, the numerical solution is broken up into several different computational blocks. The exact nature of these blocks and the methods used within them are described in sections 3.2.2 and 3.2.3, while the entire solution procedure is summarized in section 3.2.4. To give a better idea of the procedure, a graphical representation of the computational blocks is shown in Figure 3-4

3.2.2 Determining the Velocity and Pressure Fields

Due to the presence of both velocities and pressures in the momentum equations, a technique known as time splitting is used to update velocity and pressure.

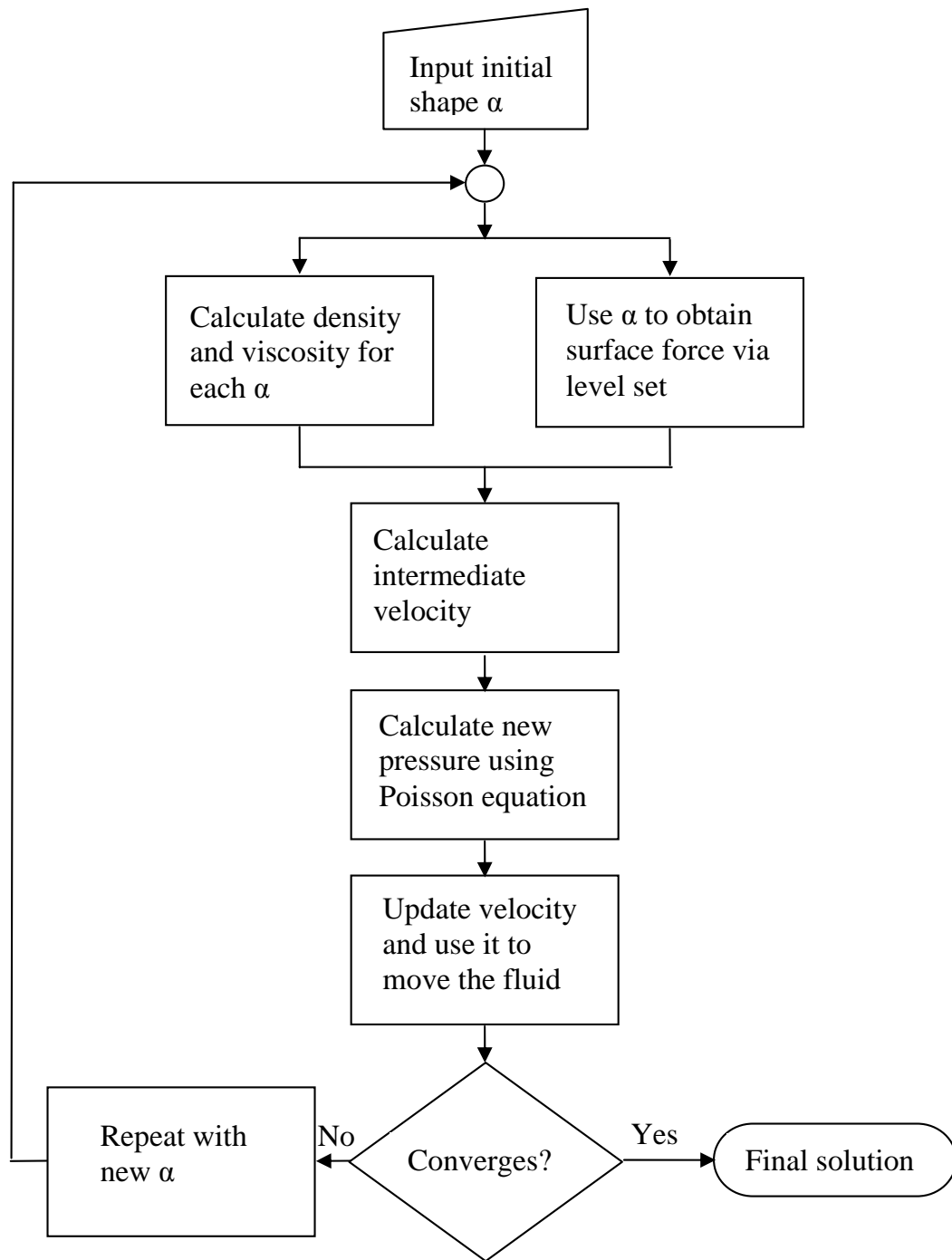


Figure 3-4. Flowchart of solution procedure

This is the same technique used by Haj-Hariri et al [33] to solve for thermocapillary motion of deformable drops. The velocity update is done in two steps according to Eq. 3.33 and 3.34:

$$\frac{u^* - u^n}{dt} = -u^n \cdot \nabla u^n + \frac{1}{\rho^n Re} [\nabla \cdot \tau^n + F^n] \quad (3.33)$$

$$\frac{u^{n+1} - u^*}{dt} = \frac{1}{\rho^n Re} [-\nabla P^{n+1}] \quad (3.34)$$

The terms with superscript n denote values at the present time step and $n + 1$ refers to the updated values. The u^* term is an intermediate velocity which is used to calculate the new pressure by the Poisson equation, Eq. 3.35:

$$\nabla \cdot \left[\frac{1}{\rho^n} \nabla P^{n+1} \right] = \frac{Re}{dt} \nabla \cdot u^* \quad (3.35)$$

This equation is iteratively solved to calculate the new pressure values. Once these values are known, the velocities can be updated to the next time step. Therefore by using the intermediate velocity, the pressure and velocity are updated and ready for the next time step.

In numerically solving Eq. 3.33, 3.34, and 3.35, all the time derivatives are evaluated using a forward finite difference scheme, while the position derivatives are evaluated using a central finite difference. Examples of these schemes for radial

velocity u are shown in Eq. 3.36, 3.37, and 3.38:

$$\frac{\partial u}{\partial t} = \frac{u(t + \Delta t) - u(t)}{\Delta t} \quad (3.36)$$

$$\frac{\partial u}{\partial x} = \frac{u(x + \Delta x) - u(x - \Delta x)}{2\Delta x} \quad (3.37)$$

$$\frac{\partial^2 u}{\partial x^2} = \frac{u(x + \Delta x) - 2u(x) + u(x - \Delta x)}{\Delta x^2} \quad (3.38)$$

These schemes are derived from a Taylor series expansion of the function and provide an accuracy of order Δx^2 . Therefore small grid spacing is used to increase the accuracy of the approximations.

3.2.3 Determining Surface Force and Moving the Interface

The surface force is calculated according to Eq. 3.8 using the normals and curvature of the surface. These values are determined from the gradient of the Level-Set function as in Eq. 3.31 and 3.32. Since the system is an axisymmetric r-z coordinate system, the normals are calculated according to Eq. 3.39 and 3.40:

$$n_r = \frac{\partial \phi}{\partial r} \quad (3.39)$$

$$n_z = \frac{\partial \phi}{\partial z} \quad (3.40)$$

Therefore, the Level-Set function is required to accurately obtain the surface force.

This function is calculated using the method described in section 3.1.2 and solving Eq. 3.23 thru Eq. 3.30. The only difference for the r-z system as opposed to the x-y system is the form of the gradient operator, so the method of determining the Level-Set is the same. The important change for the r-z coordinate system is the method for calculating the VOF.

The VOF uses a volume of fluid that is moved between the computational grids in a similar way actual fluid volumes would move between boxes. In an x-y coordinate system, the volume is just the area of the square grid multiplied by a finite depth. Since the depth is the same for each box, it is only necessary to move the areas that are in the x-y plane. Also the volume of the boxes do not change for different values of x or y, as the grid spacing is not dependent on x or y. However in the r-z coordinate system, rotating the r-z plane through 360° of angle θ creates the volume. The axisymmetric system can be solved as a single r-z plane with no dependence on θ . For this system the volume element is given by Eq. 3.41:

$$dV = r \, dr d\theta dz \quad (3.41)$$

The axisymmetry eliminates the θ term, and areas can be moved as in the x-y system.

Implementing the VOF scheme into this coordinate system is similar to the x-y system described in section 3.1.2. First the amount of fluid in each cell is

determined either from the previous time step, or given in the initial conditions. These α values are used to obtain normals and straight lines are constructed in each interface cell. The lines have the form of Eq. 3.42:

$$n_r(r - r_1) + n_z(z - z_1) = \beta \quad (3.42)$$

The point (r_1, z_1) represents the lower left corner of the computational cell. The value of β is chosen so the volume under the line equals the amount of fluid in the cell. Once the β values are determined, the Level Set function can be calculated just as in the x-y case described by Eq. 3.23 thru Eq. 3.30. The difficult part is obtaining the correct value of β to contain the volume of fluid required by α .

The first step is to construct a function to determine the volume contained under the line of Eq. 3.42 given the normals and a value for β . This volume is arrived at by integrating the area underneath the line according to Eq. 3.43:

$$W = \int_{r_1}^{r_2} (z(r) - z_1) r dr \quad (3.43)$$

Substituting Eq. 3.42 in for the limits and argument gives the following functional definition Eq. 3.44:

$$W(n_r, n_z, \beta, r_1) = \frac{\beta}{n_z} \left[\frac{1}{2} \left(\frac{\beta}{n_r} \right)^2 + r_1 \left(\frac{\beta}{n_r} \right) \right] - \left(\frac{n_r}{n_z} \right) \left[\frac{1}{3} \left(\frac{\beta}{n_r} \right)^3 + \frac{1}{2} r_1 \left(\frac{\beta}{n_r} \right)^2 \right] \quad (3.44)$$

This is the function for a specific case where the normals are positive and the line is entirely within the computational cell. The volume can be generalized to allow the line to extend to the cell to the right or above. Using the Heaviside step function, the volume becomes Eq. 3.45:

$$V(n_r, n_z, \beta, r_1, r_2 - r_1, \Delta z) = W(n_r, n_z, \beta, r_1) \quad (3.45)$$

$$-H(\beta - n_r \Delta r) W(n_r, n_z, \beta - n_r \Delta r, r_2)$$

$$-H(\beta - n_z \Delta z) W(n_r, n_z, \beta - n_z \Delta z, r_1)$$

The function H is the Heaviside step function and takes a value of 1 when the argument is greater than zero and zero when the argument is less than zero.

The last generalization concerns the signs of the normals. The manipulations of the combinations of normals provide four separate cases. The volume for each case is given by Eq. 3.46, 3.47, 3.48, and 3.49:

$$\text{If } n_r \geq 0, n_z \geq 0 \quad \text{Volume} = V(r_1, r_2, z_1, z_2, n_r, n_z, \beta) \quad (3.46)$$

$$\text{If } n_r \geq 0, n_z < 0 \quad \text{Volume} = V(r_1, r_2, z_1, z_2, n_r, -n_z, \beta - n_z \Delta z) \quad (3.47)$$

$$\text{If } n_r < 0, n_z \geq 0 \quad \text{Volume} = V_{max} - V(r_1, r_2, z_1, z_2, -n_r, n_z, -\beta + n_z \Delta z) \quad (3.48)$$

$$\text{If } n_r < 0, n_z < 0 \quad \text{Volume} = V_{max} - V(r_1, r_2, z_1, z_2, -n_r, -n_z, -\beta) \quad (3.49)$$

The maximum volume for the cell is Eq. 3.50:

$$V_{max} = \frac{1}{2}(z_2 - z_1)[(r_2)^2 - (r_1)^2] \quad (3.50)$$

Now given any normals and β , Eq. 3.44 thru Eq. 3.49 can be used to calculate the associated volume.

These functions can now be utilized to obtain the β values necessary for calculating the Level Set function in the partially filled cells. In the first step, an initial guess is tried for β along with the normals to calculate the volume. This volume is compared to the α value required for the cell. The guess for β is changed until the two volumes match and the Level Set can be calculated from the correct β values. Thus the volume of fluid can be used to determine the Level Set employing intermediate β values instead of the simple calculation required for an x-y system. The Level Set then provides the correct normals and curvature needed for the surface force.

The volume functions are also used to move the interface to a new location based on calculated velocities. The motion is accomplished by a simple conservation of mass performed on each cell; mass into one cell equals the mass taken out of a neighboring cell. The first step is to determine the amount of fluid leaving each computational cell, and determine the direction of the flow. For the cells which contain the interface, this step is accomplished by moving the line segment the

appropriate distance for the local velocity. If the line segment moves into the neighboring cell, the volume contained by the segment in the neighbor cell is the amount of fluid leaving into that neighbor cell. This is better illustrated in Figure 3-5.

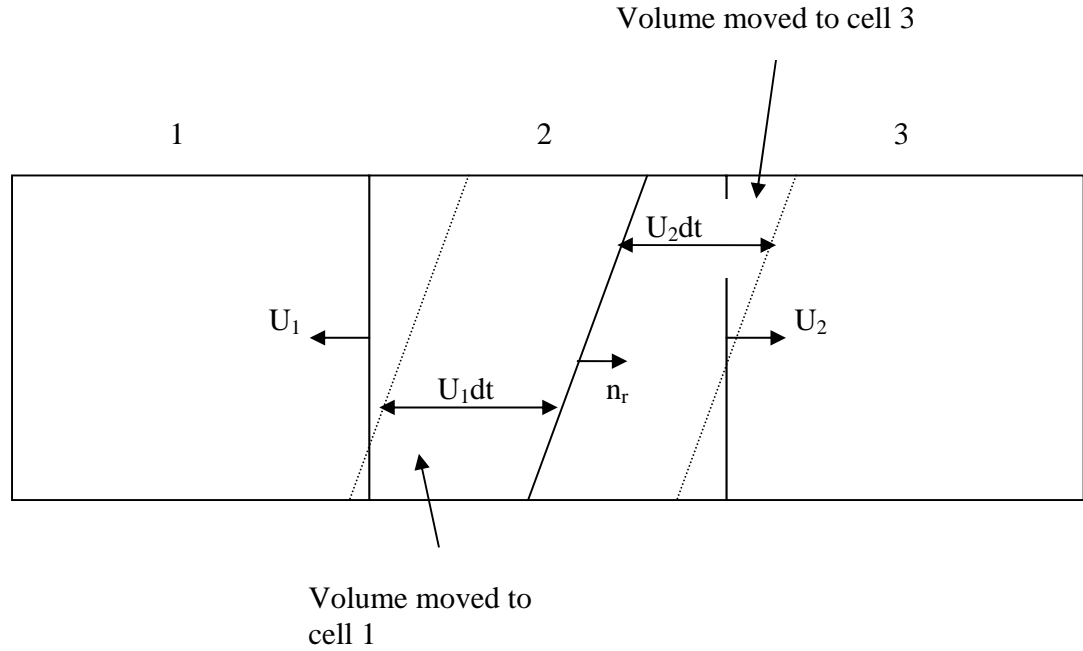


Figure 3-5. Diagram describing the calculation of motion of fluid

In Figure 3-5, cell 2 originally has the interface within it modeled as the solid line segment. The dotted lines represent where the interface would move based on the velocities U_1 and U_2 at the left and right faces. The interface is moved a distance equal to the velocity times the time step dt . Once the line segments are moved, the calculation of volume moved depends on the signs of the normals, n_r and n_z and the signs of the velocity. For example when $U \cdot n_r > 0$, the volume moved to cell 3

shown in Figure 3-5 is the correct volume. However, if the normal and the velocity have opposite signs, the moved volume is calculated by the difference between the original volume of the cell and its new volume with the dotted line. This is labeled as the volume moved to cell 1 in Figure 3-5. The last calculated volumes are from the full cells. Since these cells have no interface to move, the volume moved is a block of fluid, the size of which depends on the velocity. The various ways of determining the volume leaving the cell for all the cases are summed up in Table 3-1.

U_1	U_2	n_r	VOF1	VOF3
+	+	+	0	Volume under dotted line
+	-	+	0	0
+	+	-	0	Volume difference in cell
+	-	-	0	0
-	+	+	Volume difference in cell	Volume under dotted line
-	-	+	Volume difference in cell	0
-	+	-	Volume under dotted line	Volume difference in cell
-	-	-	Volume under dotted line	0
-	+	0	$V = \alpha_2^{\frac{1}{2}}((r_1 - U_1 dt)^2 - r_1^2)$	$V = \alpha_2^{\frac{1}{2}}(r_2^2 - (r_2 - U_1 dt)^2)$
-	+	N/A	$V = \frac{1}{2}((r_1 - U_1 dt)^2 - r_1^2)$	$V = \frac{1}{2}(r_2^2 - (r_2 - U_1 dt)^2)$

Table 3-1. Volumes leaving computational cell for all cases

In Table 3-1, the VOF1 and VOF3 correspond to volumes entering the cell neighbor to the left and the right respectively, and the velocities are for the left and right face of the computational cell. The last two cases of Table 3-1 correspond to a flat interface in the cell, and a full cell. The formulae show how the volumes are calculated based on the velocities. All these cases correspond to the motion in the r direction, but the same methods apply for the z direction using the z velocity

and normal.

Now that the amounts and direction of fluid flows are calculated, the volumes can be updated for the next time step. Each cell is labeled by an i and j to denote the position in the r and z directions. The update is done according to Eq. 3.51:

$$\alpha(i, j) = \frac{\alpha(i, j) V_{max} + VOF3(i - 1, j) + VOF1(i + 1, j) - VOF1(i, j) - VOF3(i, j)}{V_{max}} \quad (3.51)$$

The terms in Eq. 3.51 correspond to the addition of volume from the left and right neighboring cells, and the loss of volume to those cells. V_{max} is the maximum volume the cell can hold and is dependent on the r and z coordinates of the cell. Thus the volume of fluid, α , is actually a fraction describing the extent the cell is full. The volume of fluid is first updated for motion in the r direction, and then the entire process is repeated for the z direction. The cells on top and below the computational cell take the place of the right and left neighbors, but the procedure is the same. Once the z direction is completed, all the α values are updated and ready for the next step of the solution procedure.

3.2.4 Overview of solution procedure

Utilizing the numerical methods, a solution procedure is implemented to determine the steady state shape and velocity of the drop or bubble. First a computa-

tional grid is set up. An initial VOF function is defined to model an axisymmetric sphere in the r - z plane. The sphere is centered at the midpoint of the grid height, and the grid is offset so that there is an equal distance from the edge of the sphere to each boundary. Initial values for velocity and pressure are also input. The last initial conditions are for density and viscosity. Since the density and viscosity of a grid point is a function of the VOF value at that point, they can be calculated at each grid point by Eq. 3.19. The VOF values also are used to determine the Level-Set function at each point using the method in section 3.2.3. The Level-Set values are put into Eq. 3.39 and 3.40 to calculate the normals and the curvature required to update the surface force.

The next step is to use Eq. 3.33 to determine the intermediate velocity. To accomplish this time splitting in the simulation, the velocities are first updated by the advection terms. The divergence of the velocity is calculated and, the stress terms are determined. These terms along with the surface force are then used to update the velocities. From this intermediate velocity, the pressure is calculated according to Eq. 3.35 and used in the second part of the time splitting, Eq. 3.34, to calculate the velocity for the new time step. The new velocity is used in the mass balance to determine the new VOF values and to move the interface for the next time step. After updating all the values, the time step is ended and the process is repeated. New density and viscosity values are calculated from the updated VOF, a new surface force is determined by the new Level-Set function, the time splitting

is done to update velocity and pressure, and the VOF is updated. This cycle is repeated until the velocity and drop shape reach steady state and the solution is done. From the solution, the drop shape and velocity profiles versus time are obtained. This numerical method is implemented for a variety of conditions to obtain the results of the next chapters.

Buoyancy-Driven Results

The solution method described in the previous chapter is utilized to simulate various buoyancy-driven flow conditions. In the first section, the simulation runs are designed to match flows with analytical solutions and previous experiments. Comparing the results with the previous or known values validates the algorithm. Next, a parameter study is done to show the effect of Reynolds number, Capillary number, and viscosity ratio. Last, a non-Newtonian power law fluid is simulated as the suspending fluid. All the simulations were carried out on IBM RS/6000 workstations and a 20 node Atipa Linux cluster.

4.1 *Validating the Algorithm*

For a spherical drop undergoing buoyancy-driven motion within an infinite domain, the migration velocity of the drop can be determined by Eq: 4.1

$$U_{migr} = \frac{2(1 + \lambda)}{3(3\lambda + 2)} \frac{\Delta\rho g a^2}{\mu} \quad (4.1)$$

where λ is the viscosity ratio, $\Delta\rho$ is the difference in density between the fluids, g is the acceleration due to gravity, a is the drop radius, and μ is the outer fluid viscosity. The migration velocity determined by equation 4.1 was found by Hadamard and Rybczynski in [56, 57]. Comparing the velocity of a drop to this Hadamard-Rybczynski velocity, shows the deviation of the drop from an infinite domain or from a spherical drop. When a wall is placed near the sphere, the drag on the sphere is increased and the migration velocity is decreased below the Hadamard-Rybczynski velocity. The ratio between these velocities is given by Eq:

4.2

$$\frac{U_{migr}}{U_{HR}} = \frac{1}{K_1} \quad (4.2)$$

The constant in equation 4.2, K_1 , is calculated by Eq: 4.3

$$K_1 = \frac{1 - 0.75857(\frac{1-\sigma}{1+\frac{2}{3}\sigma})\lambda^5}{1 - 2.105(\frac{1+\frac{2}{3}\sigma}{1+\sigma})\lambda + 2.0865(\frac{1}{1+\sigma})\lambda^3 - 1.7068(\frac{1-\frac{2}{3}\sigma}{1+\sigma})\lambda^5 + 0.72603(\frac{1-\sigma}{1+\sigma})\lambda^6} \quad (4.3)$$

The σ in Eq: 4.3 is the viscosity ratio of the outer fluid to the inner fluid, and

the λ is the ratio of the drop radius to the tube radius from Clift et al. [8]. Therefore, using equations 4.2 and 4.3 the migration velocity of a spherical drop for any condition is calculated. Comparison of the actual migration velocity with the spherical drop velocity displays the effect of deformation. Due to this, the simulation results are all compared to the corresponding spherical velocity for the system.

The first test of the algorithm was to match the migration velocity for a spherical drop. To minimize the deformation, the size ratio was chosen to be 1:20. The simulation was run at four different viscosity ratios to compare with the expected values for a sphere. The Reynolds number for the simulations was 0.01 and the density ratio is 0.7. Figure 4-1 shows the results of the runs along with the values of spherical drops calculated from equations 4.2 and 4.3.

The increase in viscosity ratio leads to decreasing the velocity ratio due to larger drag on the drop. From figure 4-1, the simulation displays the same trend in velocity ratio as the spherical results. Also, the computational data matches the spherical values within 3%. Therefore, the algorithm is able to predict the migration velocities at the 1:20 size ratio for a variety of viscosity ratios.

After matching velocity values at this small size ratio, simulations were carried out at several other size ratios including a simulation of an infinite domain. For the infinite domain, the boundary conditions at the wall were changed from the

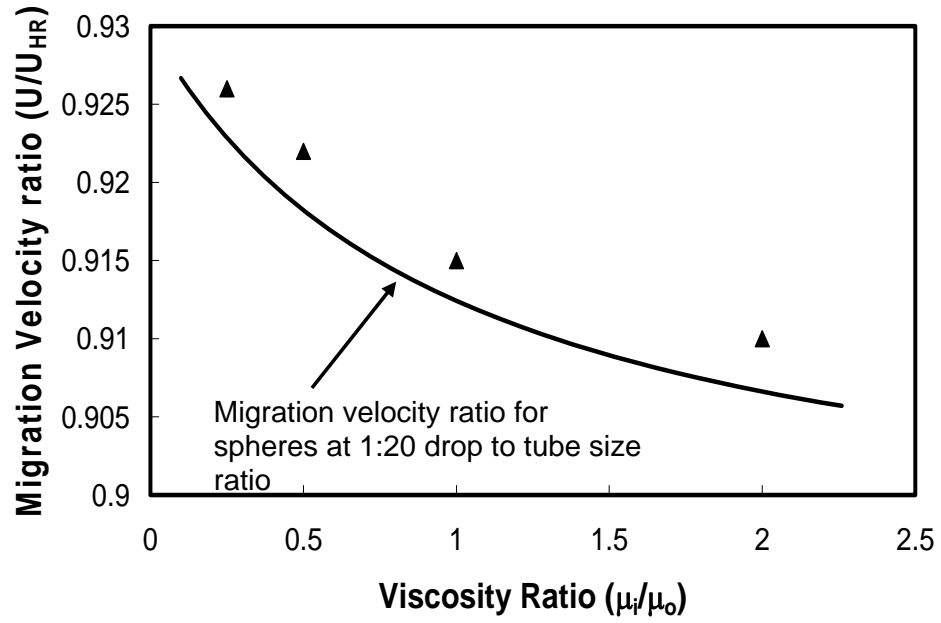


Figure 4-1. Migration velocity ratio versus viscosity ratio for sphere and present work. Size ratio 1:20, Re 0.01.

usual no slip velocity condition of Eq: 4.4

$$\mathbf{u} = 0 \quad \text{at} \quad \bar{r} = 1 \quad (4.4)$$

to the zero derivative condition of Eq: 4.5.

$$\frac{\partial \mathbf{u}}{\partial r} = 0 \quad \text{at} \quad \bar{r} = 1 \quad (4.5)$$

Equation 4.5 is valid when $\bar{r} = 1$ occurs far enough away from the drop, so a small size ratio is still used for the infinite run along with the altered boundary condition.

Along with testing the size ratio, various grid spacings were run to determine the necessary resolution for the simulation. The results of all these runs are displayed below in Table 4-1.

Size ratio	45 grid points	60 grid points	90 grid points	Calculated value
1:4 ratio	0.6250	0.6247	0.6230	0.6207
1:5 ratio	0.7014	0.7003	0.6985	0.6946
Infinite runs	0.9610	0.9750	0.9825	1.0000

Table 4-1. Migration velocity ratios for various size ratios, number of grid points, and calculated spherical values. Simulation parameters: viscosity ratio 0.25, density ratio 0.7, Re 0.01

Table 4-1 shows the simulations ability to match velocities for other size ratios, as well as reach the Hadamard-Rybczinski velocity for the infinite run. Also the increase in grid points improves the accuracy of the runs. However all the results are within 5% error.

Now that the code has been tested in predicting the migration velocity of spherical drops, the next step was to simulate experimental systems that have displayed deformation in the drops. These runs show the algorithms ability to predict the deformed shape of the drop as well as the migration velocity. Two separate systems are used for simulation; the rise of bubbles at finite Reynolds numbers of Ryskin and Leal [15] and the experimental rise of drops in a tube studied by Borhan and Pallinti [6]. The bubbles of Ryskin and Leal were in an infinite domain, so the simulation utilized the alternate boundary condition of Eq. 4.5. For the cases studied, the values of the Reynolds and Weber numbers were 5.0 and 4.0 in case 1 and 50.0 and 10.0 in case 2. Figure 4-2 displays the

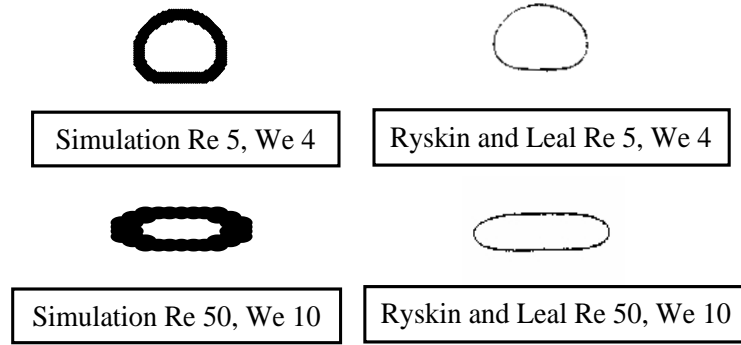


Figure 4-2. Steady state bubble shapes from present work and from Ryskin and Leal 1984 [15]

steady state shape from each run along with the corresponding shape published by Ryskin and Leal [15]. The simulation is able to duplicate the previous shapes at both conditions.

The last test was to model drop deformation within a tube and compare with the experimental results from Borhan and Pallinti [6]. Simulations were run for the parameters of system CW3-1 in [6] (density ratio 0.72, viscosity ratio 0.22, Re 0.01, Bond number 4.1) at size ratios of 0.2, 0.5, 0.7, 0.9, and 1.1 to match the velocities and shapes of various sized drops. The resulting shapes are plotted in figure 4-3 along with the experimental shapes.

Besides the steady state shape, the experimental results included the migration velocity, drop length, maximum equatorial length, and a deformation parameter D , which is the ratio of the drop perimeter to the circumference of a spherical

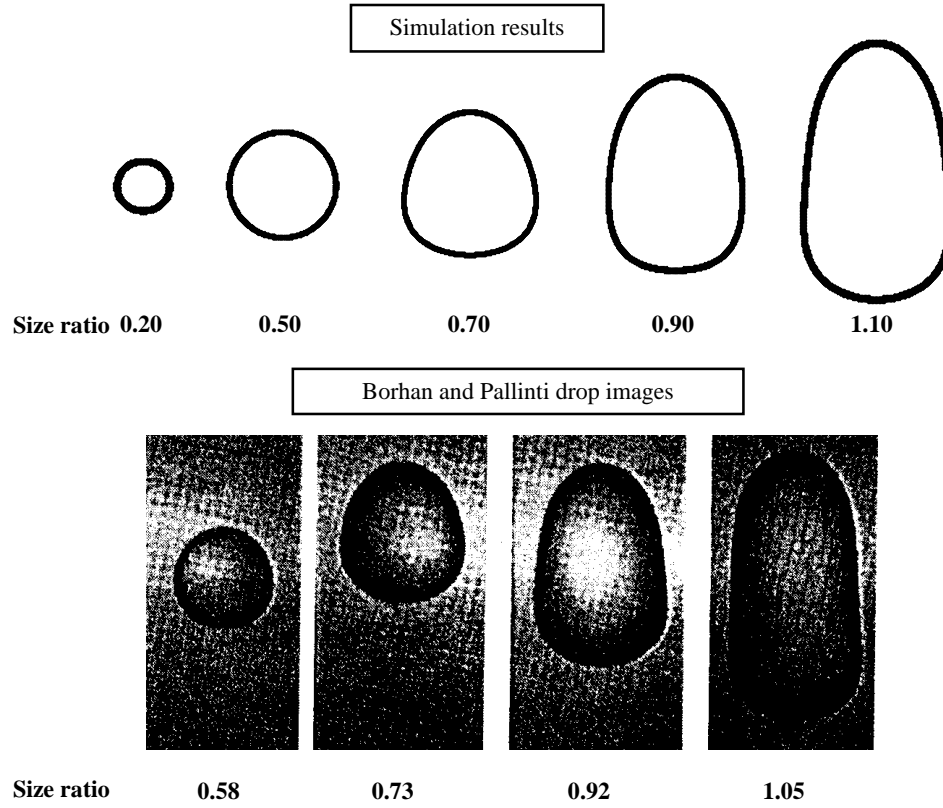


Figure 4-3. Steady state drop shapes from present work and Borhan and Pallinti 1995 [6]

drop with a radius equal to the size ratio. The parameters from the paper and the simulation runs are plotted in figures 4-4 and 4-5.

Figures 4-3, 4-4, and 4-5 demonstrate the accuracy of the algorithm in predicting drop shape and velocity for a drop within a confined system.

The previous tests were carried out to determine the efficiency of the algorithm in simulating drop motion. The simulation was able to predict drop velocity and shape for both analytical and experimental problems with a wide range of parameters. Therefore the model is suitable for use in predicting the properties of

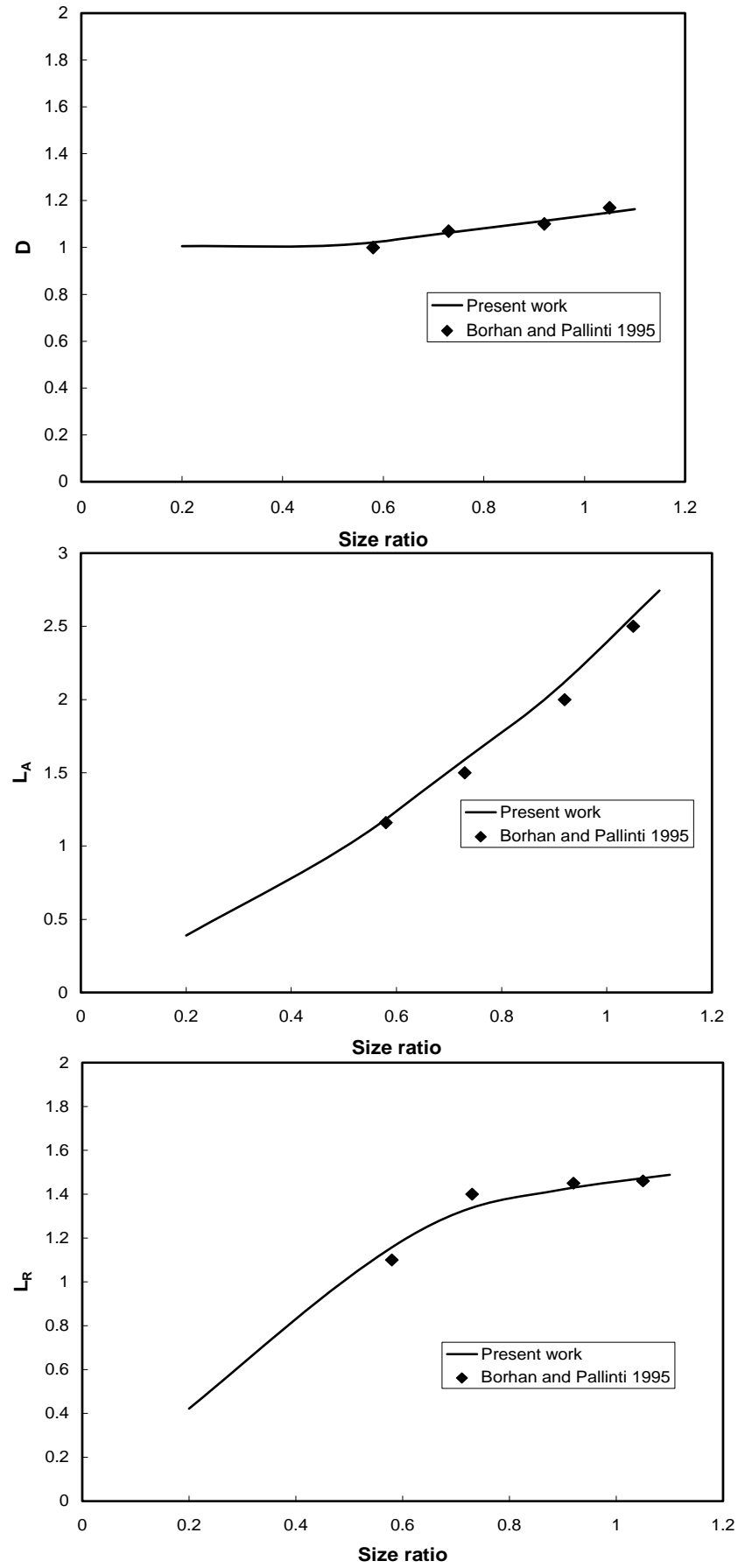


Figure 4-4. D , L_A , and L_R versus size ratio for present work and Borhan and Pallinti 1995 [6].

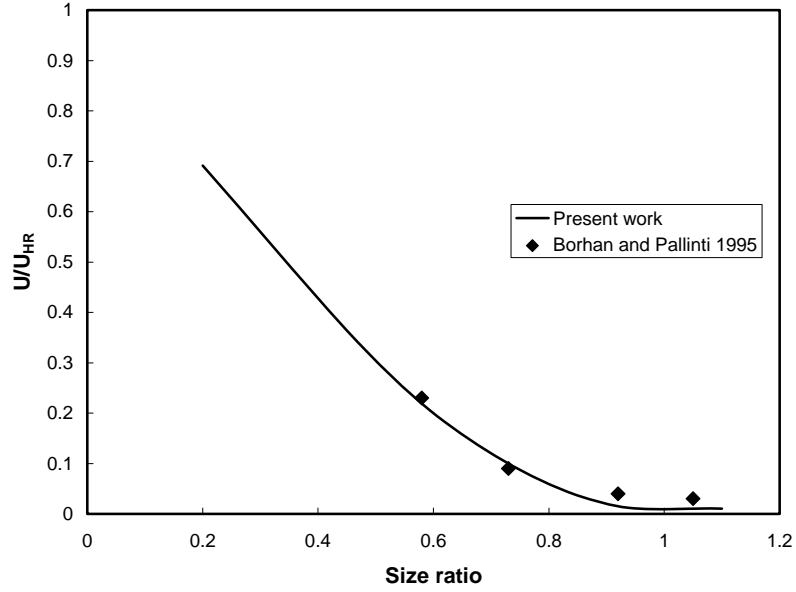


Figure 4-5. Migration velocity ratio versus size ratio for present work and Borhan and Pallinti 1995 [6].

systems difficult to explore experimentally. These simulations explore the effect of different parameters on a buoyancy-driven flow at finite Reynolds numbers, and are described in the parameter study of the next section.

4.2 *Parametric Study of Various Dimensionless Groups*

After validating the simulation, the next step was a parameter study for buoyancy-driven flow of a drop in a tube. In the system, the important dimensionless groups are the Reynolds and Capillary numbers, and the viscosity, density, and size ratios.

The calculations investigated the effect of Reynolds and Capillary numbers, different viscosity ratios, and non-Newtonian character of the suspending fluid for finite values of the Reynolds number. The results of these investigations are presented in the following sections.

4.2.1 Reynolds and Capillary Study

The first two parameters varied were the Reynolds and Capillary numbers. For constant density, viscosity and size ratios, simulations were run for a range of Reynolds numbers (1, 10, 20, and 50) and Capillary numbers (1, 5, 10, 20, and 50). In each case the size, viscosity, and density ratios were 0.7, 1.0, and 0.7 respectively. The steady state shape results from these trials are shown in figure 4-6.

The deformation increases with increasing Capillary number. Because the Capillary number is defined as $\frac{\mu U}{\sigma}$, an increase in Capillary number decreases the surface tension. Thus, the drops with a lower surface tension are easier to deform. The shape results confirm this. Also the deformations increase as the Reynolds number increases. This increase in deformation with Reynolds number was also witnessed by Bozzi et al. [17] and was expected of the data.

Besides the drop shapes themselves, the deformation can be quantified for each drop. Three different values have been determined to characterize the shapes. The first is D or the deformation parameter. This value compares the drop perimeter to the circumference of the equivalent spherical drop. For a set volume, the spherical

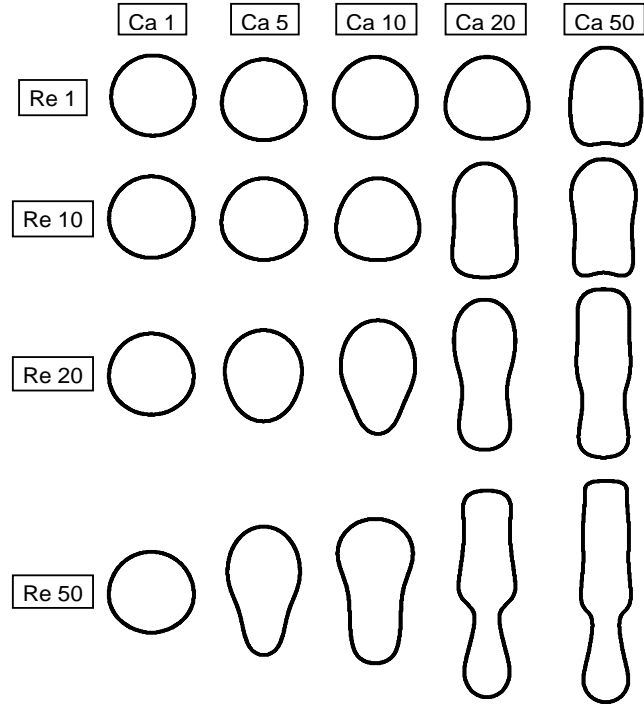


Figure 4-6. Steady state drop shapes for parameter study. Size ratio 0.7, viscosity ratio 1.0, density ratio 0.7.

shape has the smallest value for the perimeter. Therefore, values of D greater than 1 demonstrate the variation of the drop shape from a sphere. The second value is L_A or length of the drop. This determines how much the drop has spread out in the z direction. The last value is L_R or the maximum equatorial length of the drop. Figure 4-7 shows the D values, L_A , and L_R as functions of Capillary number for series of Reynolds numbers.

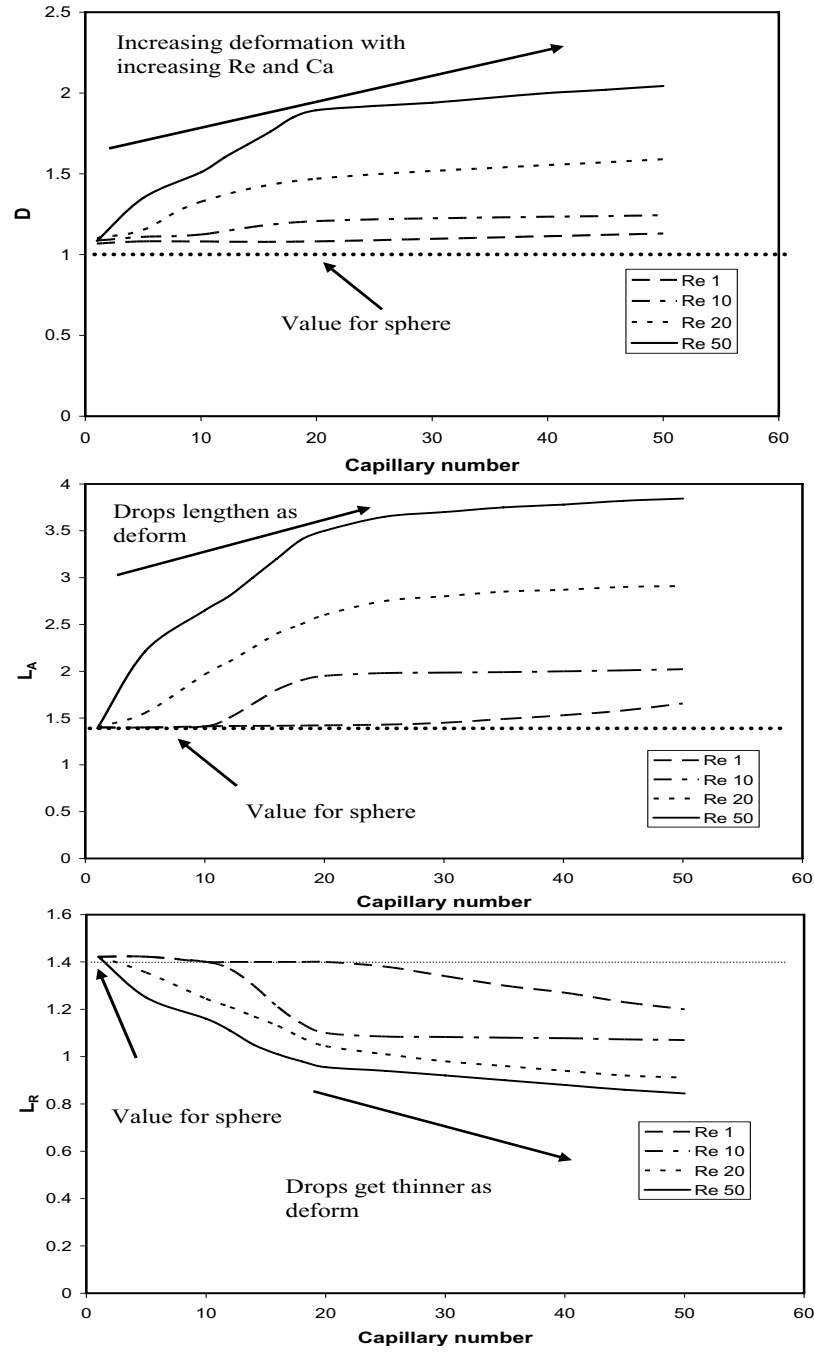


Figure 4-7. D , L_A , and L_R versus Capillary number for $Re=1, 10, 20$, and 50 .

The data in figure 4-7 confirm the visual findings of the steady state shapes. The deviation from a spherical drop grows with increasing Capillary and Reynolds numbers. Also, the runs above a Capillary number of 10 are more sensitive to changes in Reynolds numbers. The drop shapes in those runs elongate with higher flows due to the decreased surface tension, while the smaller Capillary numbers retain their shapes and deform only at higher Reynolds numbers. The smallest Capillary value of 1 retains spherical shape even at the highest Reynolds number.

In the original set of data, there were some anomalies in the shapes of certain combinations of Reynolds and Capillary numbers. To elucidate the transitions of these shapes, further runs were carried out. The drop shapes at Re 20, Ca 5 and Re 50, Ca 5 differed substantially, and it was not clear how the drops of Re 50, Ca 10 and Re 50, Ca 20 were related. Therefore, extra runs at Re 25, Ca 5, Re 35, Ca 5 and Re 50, Ca 15 were performed to obtain these transition shapes. Figure 4-8 displays the shapes of Ca 5 for the four different Reynolds numbers, and figure 4-9 displays the shapes at Re 50 for the three different Capillary numbers.

For the Ca 5 shapes, the transition occurs by the drop elongating in the tail region. The front of the drop remains the same with the back end narrowing and lengthening. The transition at Re 50 has a similar pattern of elongation. However, the narrowing begins to pinch off the drop and appears to be leading to the breakup of the drop at higher Reynolds and Capillary values.

All the simulations in the parameter study report a Reynolds number based

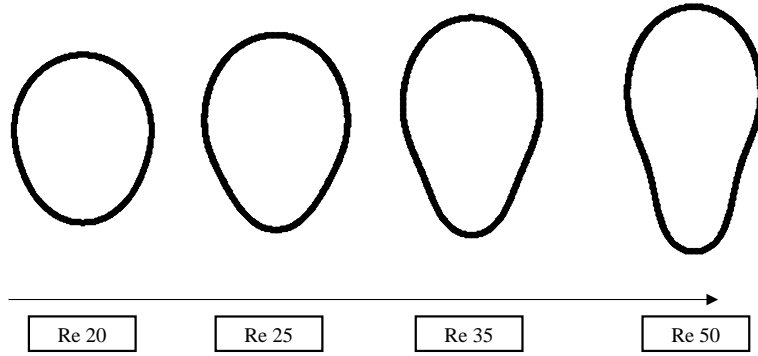


Figure 4-8. Transition of shapes for Ca 5 from Re 20, 25, 35, and 50.

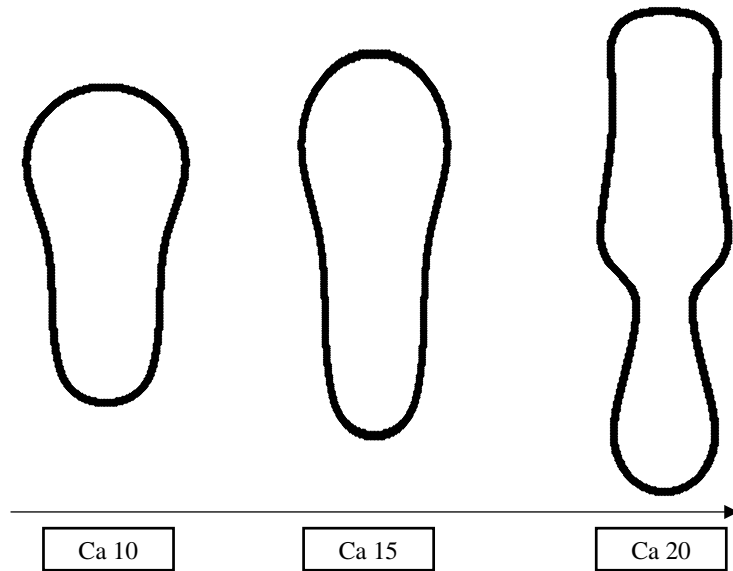


Figure 4-9. Transition of shapes for Re 50 from Ca 10, 15, and 20.

on the migration velocity of the drop. Thus the reported Reynolds numbers are equal to the dimensionless Reynolds number of the simulation multiplied by the dimensionless migration velocity of the drop. To produce the same migration ve-

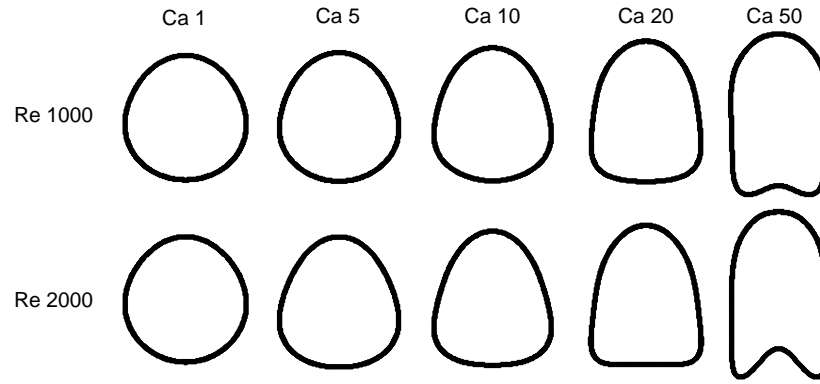


Figure 4-10. Steady shapes for spherical starting simulations. Re^* 1000 and 2000; Ca 1, 5, 10, 20, and 50.

locity based Reynolds number for different migration velocities, the simulation Reynolds numbers are different for each case above. Also the simulations at higher Reynolds numbers utilized a previous steady state shape as the initial shape for the calculation. The steady shapes of figure 4-6 may not be reached by experimental conditions where the drops begin as spheres. To study the effect of the initial shape as well as the simulation Reynolds number, more buoyancy-driven calculations were done. Each of the runs began with a sphere as the initial shape. The parameter values for the simulation Reynolds numbers were 1000 and 2000, while the Capillary numbers were still 1, 5, 10, 20, and 50. The resulting shapes and deformation parameters are shown in figures 4-10 and 4-11.

The drop shapes for the runs of figure 4-10 display a distinct transition as the Capillary number increases. The drops begin to flatten until at Ca of 50, where a dimple in the back of the drop begins to form. As the Reynolds number is doubled,

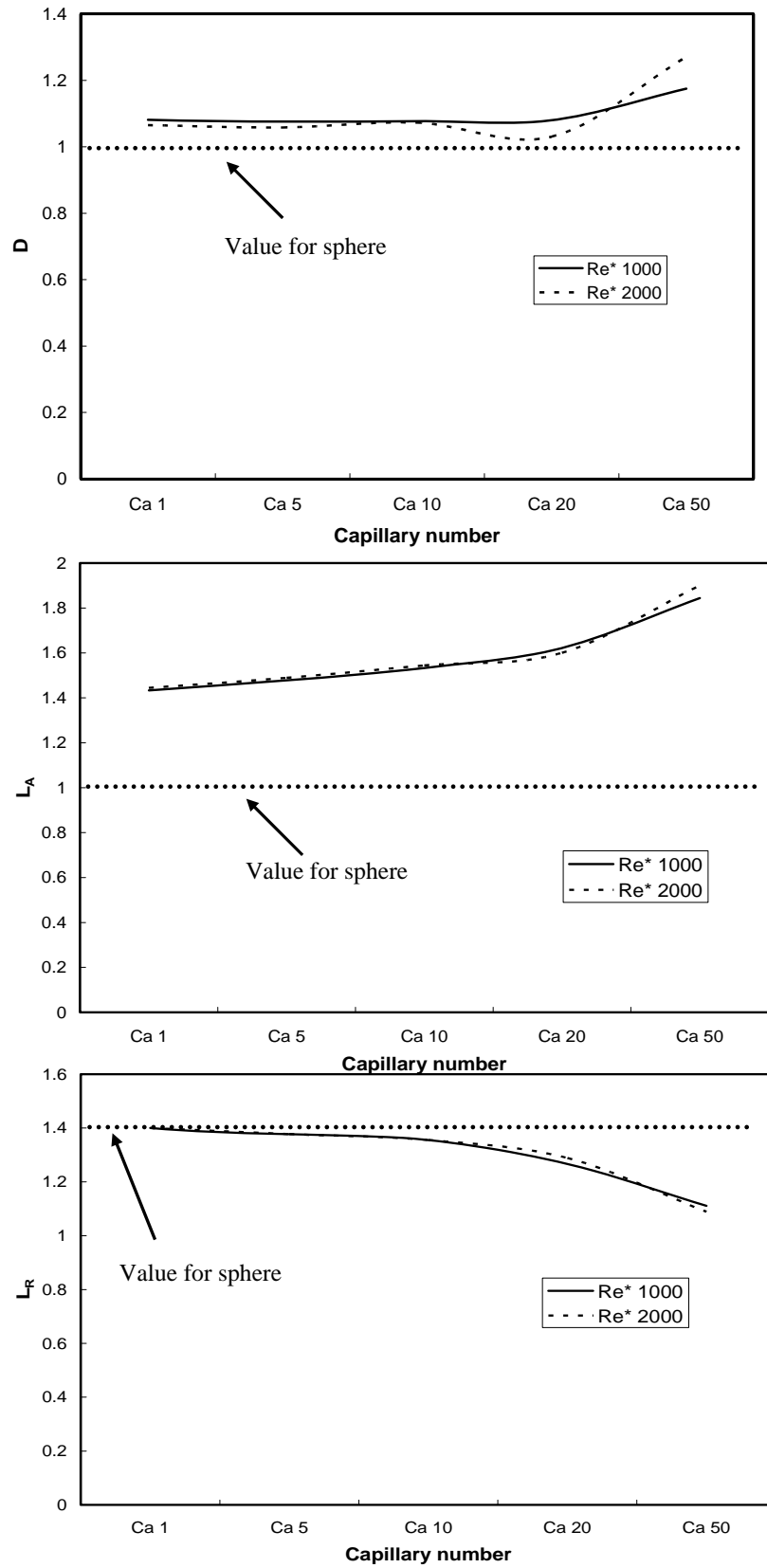


Figure 4-11. D , L_A , and L_R versus Capillary number for Re^* 1000 and 2000.

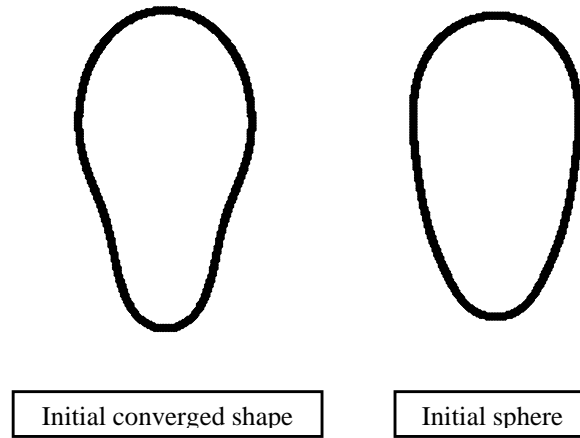


Figure 4-12. Comparison of shapes for Re 50, Ca 5; using converged solution or sphere as initial condition.

the flattening is increased for each drop and the dimple grows for Ca 50. This is the expected pattern for deformation and is better seen in these runs where the simulation Reynolds number is remaining constant. Also the effect of the initial shape is seen for the higher Capillary numbers. In the original simulations, the drops develop tails for Ca 20 and 50 for Reynolds numbers near 2000. However, with the sphere as the initial condition, the drops flatten out in the back or form dimples, but do not stretch out to produce tails. This effect of initial condition was further tested on the higher Reynolds number simulations of the initial study. For Re 50 Ca 5, and Re 20 Ca 50, calculations were performed with the same Reynolds and Capillary numbers as the initial study. In these runs, the initial shapes were spheres instead of the steady shapes of the previous runs. The resulting shapes from these runs are shown in figures 4-12 and 4-13.

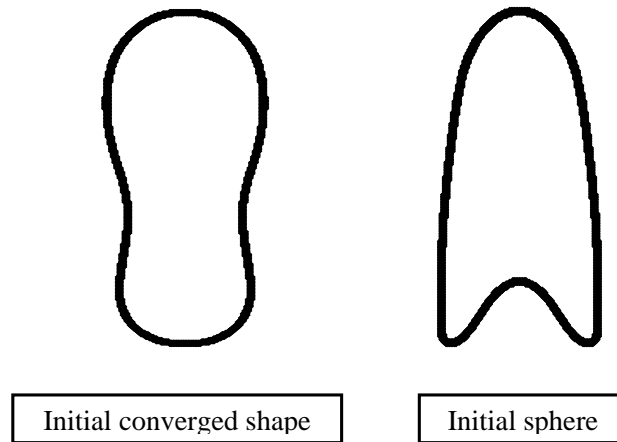


Figure 4-13. Comparison of shapes for Re 20, Ca 50; using converged solution or sphere as initial condition.

Figures 4-12 and 4-13 show the effect of the initial condition on the steady shape. The drops elongate, however some of the features are different. The tail in the initial sphere Re 50 Ca 5 case is not pinched as in the simulation started with a steady shape. The Re 20 Ca 50 case also displays less pinching in the tail as well as a dimple in the back that is present in lower Reynolds number simulations, but not the steady shape simulations. One cause for these differences could be the numerical error of the simulation. By using the converged shapes as the starting point for the next computation, the errors in mass conservation at each time step are all added together. Thus the Ca 5 Re 50 drop based on an initial sphere has more mass than the steady shape result. This additional mass could account for the widening of the drop. This narrowing of the drop can also change the viscous

forces the drop experiences. When the Ca 50 drop narrows, it does not allow the dimple to remain and forces the drop to elongate, and narrow even more. While this gives a possible explanation to the differences for higher Reynolds numbers, the alterations at lower Reynolds number are clearly the initial shape affecting the steady state result. More study needs to look into whether the drops have more than one steady state for a set of parameters, and which initial condition should be used to obtain the true physics of the system.

Along with drop shapes, another important result is the migration velocity. This migration velocity is compared with the Hadamard-Rybczinski velocity to obtain the velocity ratio discussed in the previous section. The ratio is calculated for a sphere and comparison of this value to the actual migration ratio gives the effect deformation has on drop velocity. The drop migration velocity is calculated using Eq. 4.6

$$U_{migr} = \frac{\sum \alpha(i, j) V(i, j)}{\sum \alpha(i, j)} \quad (4.6)$$

where α is the volume of fluid value of the grid cell and V is the vertical velocity at that point. For the size, density, and viscosity ratios used, the Hadamard-Rybczinski velocity has a value of 0.267, and the velocity ratio for a sphere is 0.0821 from equations 4.2 and 4.3. Figure 4-14 shows the migration velocity ratios for each run.

The results of figure 4-14 show a range of effects on the velocity ratio. For the drops above a Capillary number of 10, the deformation increases the velocity ratio

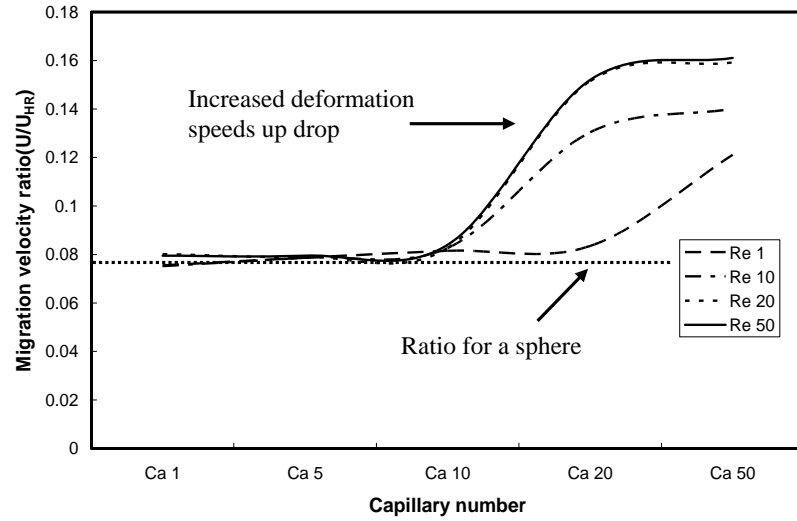


Figure 4-14. Migration velocity ratios versus Capillary number for Re 1, 10, 20, and 50.

above the expected spherical result. The ratio increases with increasing Capillary number and Reynolds number until the transition between a Reynolds number of 20 and 50. The increase in deformation in that range leads to a small increase in velocity. The drop velocity appears to be reaching a maximum value plateau for these conditions. In the lower Capillary numbers the drops remain spherical until higher Reynolds numbers. This does not reduce the surface area of the drop perpendicular to the flow, or reduce the drag on the drop. Thus the velocities remain the spherical value, increasing only when the drops begin to deform.

Besides the migration velocity of the drop, another result of the simulation is the entire velocity field. Graphing the streamfunction provides information about the velocity field in one graph. Using the plotting program, TecPlot, the

streamfunctions were plotted for each velocity field. These plots are displayed in figures 4-15 and 4-16.

Figures 4-15 and 4-16 plot the streamfunctions for each of the drop shapes in the parameter study. Most of the graphs show the expected results of recirculation within the drop, and fluid flowing past the drop in the outer fluid. Some of the larger deformations for Re 20 and 50 have areas within the drop of small values of the streamfunction. These are areas of stagnation for the inner fluid. In the case of Re 50 and Ca 10, the drop develops a second area of circulation in the rear tail of the drop. In the other drops with tails, the fluid in this area is stagnant and this recirculation is not present. To test for the presence of this second area, the surface velocity for the drop is plotted versus arclength to show the change in sign related to a second recirculation in figure 4-17.

Since the interface is smeared across grid points instead of a sharp line, the surface velocity plot has a dispersal of values as the surface velocity is also smeared. The trend in the velocity is evident, and the appearance of the second recirculation area is confirmed by the change in sign of the surface velocity.

4.2.2 Viscosity Ratio Tests

In addition to the Reynolds and Capillary numbers, the viscosity ratio was varied to determine the effect on the system. Since the steady state shape showed a large deformation, the base case was chosen to be Re 10, and Ca 20. The viscosity

ratios tested were 0.5 and 1.5 using the same density and size ratio as in the base case. The resulting values are shown in table 4-2, and the shapes are displayed in figure 4-18.

Trial	Migration velocity ratio	D	L_R	L_A
Viscosity ratio 0.5	0.1694	1.437	1.089	2.422
Viscosity ratio 1.0 (base case)	0.1304	1.207	1.089	1.978
Viscosity ratio 1.5	0.1431	1.373	1.022	2.444

Table 4-2. Results from viscosity ratio test along with base case values

For both changes in viscosity ratio, the deformation and the velocity increases over the base case. In the 0.5 case, the viscosity of the outer fluid is higher than the base case. This higher viscosity produces a larger force on the interface, which increases the deformation and speeds up the drop. The 1.5 case has a smaller outer viscosity than the base case. The outer fluid is easier to move around the drop and responds with a higher velocity. The force of the fluid on the interface is increased by the higher velocity, and the drop elongates more than the base case. This elongation reduces the drag, increasing the migration velocity.

The corresponding streamfunctions for the viscosity ratio test are shown in figure 4-19. The streamfunctions show the typical flow around the drops, along with the different internal circulations for the different viscosity ratios. As the viscosity ratio increases, the recirculation center moves from the front of the drop for 0.5 to the back end of the drop in the 1.5 simulation.

4.2.3 Non-Newtonian Fluids

Last, a non-Newtonian power law fluid is introduced as the suspending fluid. The simulation is the same as before with an additional calculation to determine the viscosity at each point. The stress tensor for a power law fluid is defined by Eq. 4.7

$$\bar{\bar{\tau}} = -[m(-\Phi_v)^{\frac{n-1}{2}}][\nabla \mathbf{u} + \nabla \mathbf{u}^t] \quad (4.7)$$

where the $[m(-\Phi_v)^{\frac{n-1}{2}}]$ term is the equivalent to Newtonian viscosity, μ . The n in equation 4.7 is the power law index and the $-\Phi_v$ term is determined by the velocity field. Therefore, the viscosity at each point depends on the velocity field, the viscosity ratio, and the volume of fluid at the point. Introducing this into the code allows for a non-Newtonian fluid to be simulated. The power law indexes of 0.5 and 1.5 are tested using the case of Re 10 and Ca 20 as a base case. The results of the test are shown in table 4-3 and the steady shapes in figure 4-20.

Trial	Migration velocity ratio	D	L_R	L_A
Power law index 0.5	0.0233	1.207	1.178	1.922
Power law index 1.0 (base case)	0.1304	1.207	1.089	1.978
Power law index 1.5	0.1596	1.106	1.156	1.733

Table 4-3. Results from non-Newtonian fluid test along with base case values

In both non-Newtonian cases, the drops shorten. The 0.5 case has a larger L_R than the base which contributes to the decrease in velocity ratio. The 1.5 case also has the increase in L_R but an increase in the velocity ratio. For a power law fluid, the 1.5 case corresponds to a shear thinning fluid. Therefore, the shear at the drop

interface decreases the viscosity of the outer fluid making it easier to move around the drop and a higher drop velocity. The 0.5 case is shear thickening, causing the reverse to occur. The higher viscosity at the interface introduces more drag on the drop and a lower velocity ratio.

For the 1.5 case, the flattening back of the drop produces a recirculation in the flow behind the drop. While the figure appears to have streamlines passing through the interface, the circulation areas in the back of the drop and behind the drop are two separate areas. The thickness of the drop shape in the figures covers the space between the areas. The recirculation behind the drop can be seen by comparing the streamfunction plots for the 0.5 and 1.5 cases shown in figure 4-21. To further investigate this recirculation, a simulation was run at a Reynolds number of 1, Capillary number of 20, and power law index 1.5. These parameters were used for the original size ratio of 0.7 as well as 0.9 and 1.1. These extra size ratios were studied since the increased size ratios should have larger deformations and possibly more recirculation in the flow. The resulting shapes and streamfunctions for these runs are displayed in figures 4-22 and 4-23.

The simulations at the lower Reynolds number show less deformation than at the higher values. With the lower deformation, the recirculation is less however is still present for all three sizes. The larger size ratios display a similar deformation to each other as the front of the drop forms a tip and the back flattens out, producing a missile like shape. For the larger sizes, the streamfunctions could not

be resolved.

4.3 *Conclusions on Buoyancy-Driven Motion*

The simulation of buoyancy-driven motion has displayed the accuracy of the algorithm for the motion of two-phase flows. In comparison of computational results with analytical and experimental values, the simulation predicted both the correct shape of the drop and the correct migrational velocity. This confirmation was made at several different size ratios, viscosity ratios, and fluid conditions. Due to the availability of results for buoyancy-driven flow, these simulations were able to provide confidence in the new algorithm.

Utilizing this new algorithm, computations were carried out at various parameter values to determine their effects on drop velocity and shape. Parameter tests were done for Reynolds numbers of 1, 10, 20, and 50 with Capillary numbers of 1, 5, 10, 20, and 50. The results display increasing deformation with increases in the Reynolds and Capillary numbers. The use of D , the deformation parameter, L_A , and L_R to characterize the deformations helps quantify these increases. Also, comparison to expected values for a spherical drop shows the deviation from the original shape. The larger Capillary number drops have a smaller surface tension than at low Capillary numbers. With the decrease in surface tension, drag forces elongate the drop along the axis of motion. This elongation reduces the surface area of the drop perpendicular to the motion, thus reducing the experienced drag

and increasing the velocity over a spherical drop. As the elongation increases, the drops grow too large and begin to pinch off. At larger values of Reynolds or Capillary numbers, the pinch points become smaller and lead to drop breakup.

While the deformation increases at each Capillary value as Reynolds number increases, the shapes of Ca 20 and 50 are more sensitive to the Reynolds number than the other Capillary values. To determine the transition shape between the large and small Capillary numbers, simulations at Ca 15 were run. The shape result was closer to the small Capillary values rather than the large deformation at a Capillary value of 20. It appears that Capillary values of 20 or larger lead to drop breakup at higher Reynolds numbers, while the Capillary values below 20 have stable drops which remain intact.

The runs in the parameter study utilized previous steady shapes as initial conditions for the higher Reynolds number calculations. This allowed for less simulation time to reach new steady states. However, further runs using spheres as initial shapes, produce different steady shapes. The effect of numerical simulation error may account for some of these differences at higher Reynolds numbers. However this effect of initial shape needs to be studied further. The difference between Reynolds numbers based on migration velocities of the drops and based on the dimensionless velocity of the system is also investigated. Keeping the simulation Reynolds number constant, produces sets of drop shapes that more accurately display the effects of Capillary and Reynolds numbers on deformation.

Besides the drop shape, the parameters also effected the migration velocity of the drops. The drag force on the drops is proportional the surface area perpendicular to the direction of flow. Deformation of the drops can cause a decrease in this surface area. For the drops with large surface tension, large deformation does not occur, the surface area decreases only slightly, and the velocity increase over the sphere is small. Some of the drops experience deformation which flattens the head of the drop and actually increases the surface area leading to a decrease in velocity. The drops with small surface tension experience a large change in shape, significantly narrowing the drop and increasing the velocity. Some of the drops reached a velocity ratio twice of the spherical value for the system. Thus drop deformation and the parameters which effect it, have a large role in the velocity of the drop.

The role of viscosity ratio in the problem was also investigated with simulations at Re 10 and Ca 20 for viscosity ratios of 0.5 and 1.5. The change in viscosity increases the deformation for both runs. However the 0.5 shape possesses a thinner tail than the 1.5 counterpart. For the 0.5 case, the larger inner viscosity increases the fluid force on the interface. This force causes the drop to elongate more than the base case, and increase the drop velocity. In the 1.5 case, the smaller outer viscosity increases the fluid flow around the interface. The increase in flow also increases the viscous force on the interface and causes the drop to elongate. The elongation decreases the drag on the drop, and the drop velocity increases.

The last parameter studied for buoyancy-driven motion was the non-Newtonian character of the suspending fluid. The non-Newtonian fluid chosen was a power law fluid, and the values of the power index tested were 0.5 and 1.5. The index of 0.5 corresponds to a shear thickening fluid, which introduces a higher viscosity at the interface. This leads to a larger drag force and thus a smaller velocity of the drop. In the case of 1.5, the fluid is shear thinning and an opposite effect occurs. The lower viscosity at the interface reduces drag and the velocity increases. The shapes also reflect these effects. The 0.5 shape deforms more with the larger drag while the 1.5 case has less drag on it and the drop obtains a flatter back. This flatter back produces recirculation in the flow behind the drop. The recirculation occurs even at a lower Reynolds number for smaller deformation.

The simulation of buoyancy-driven flows allowed the testing of the new algorithm to study two-phase flows. Along with proving the effectiveness of the algorithm, several parameter studies were conducted for the flow system. These studies provided insights about the role of Reynolds number, Capillary number, viscosity ratio, and non-Newtonian fluids in the deformation and velocity of rising drops. The next step is to implement the model for the pressure-driven motion of a drop within a tube and to determine the effect of finite Reynolds numbers.

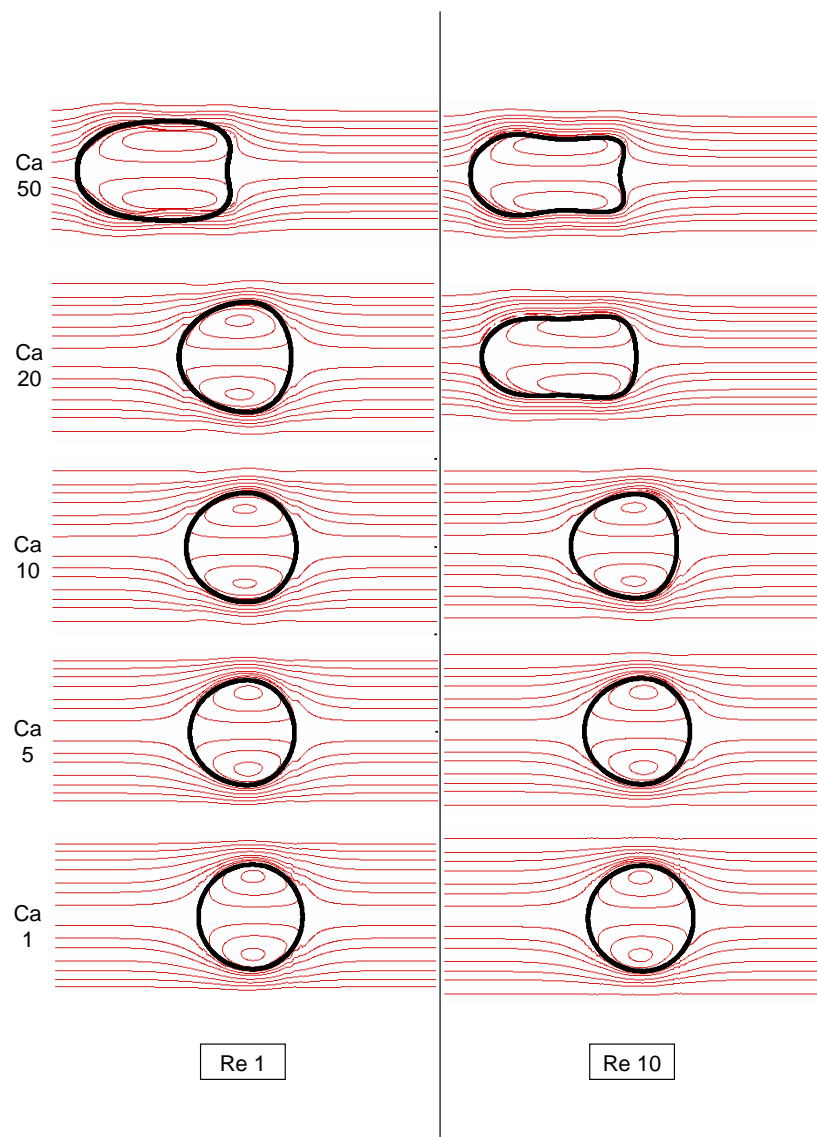


Figure 4-15. Streamfunctions for parameter study for $Re = 1$ and 10 .

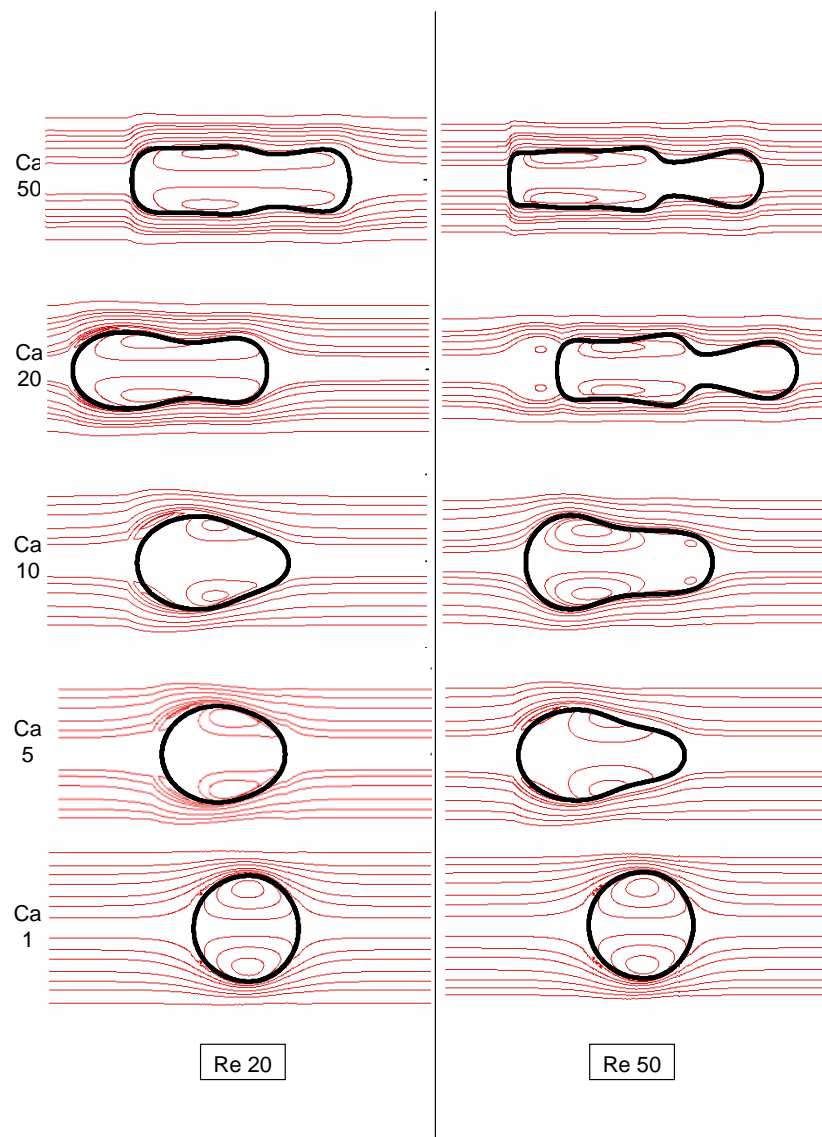


Figure 4-16. Streamfunctions for parameter study for $Re = 20$ and 50 .

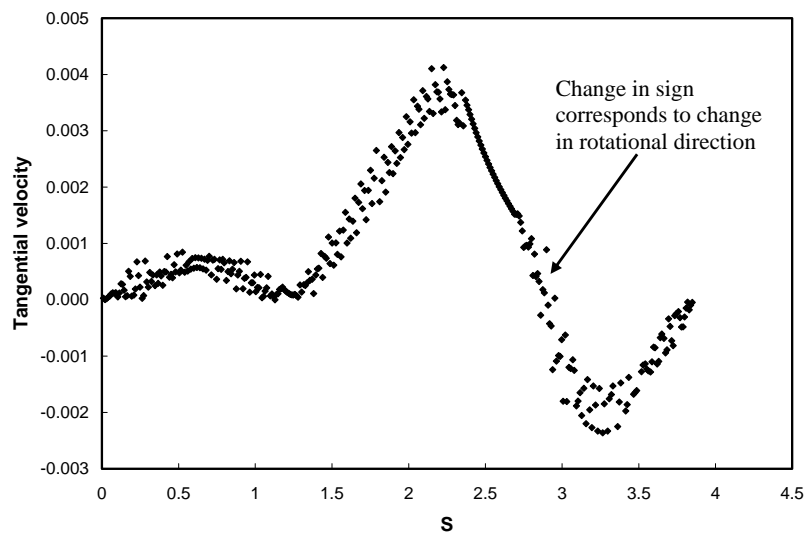


Figure 4-17. Surface velocity ratios versus arclength for $Re = 50$ $Ca = 10$ shape.

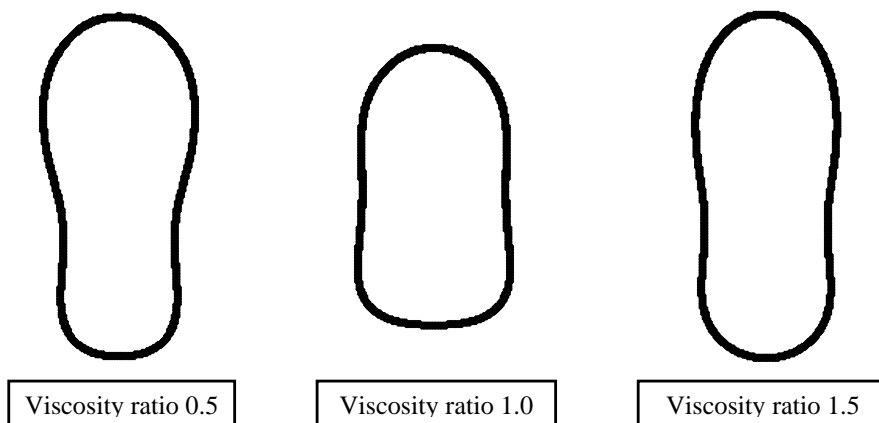


Figure 4-18. Steady state shape results from viscosity ratio test for 0.5, 1.0 (base case), and 1.5.

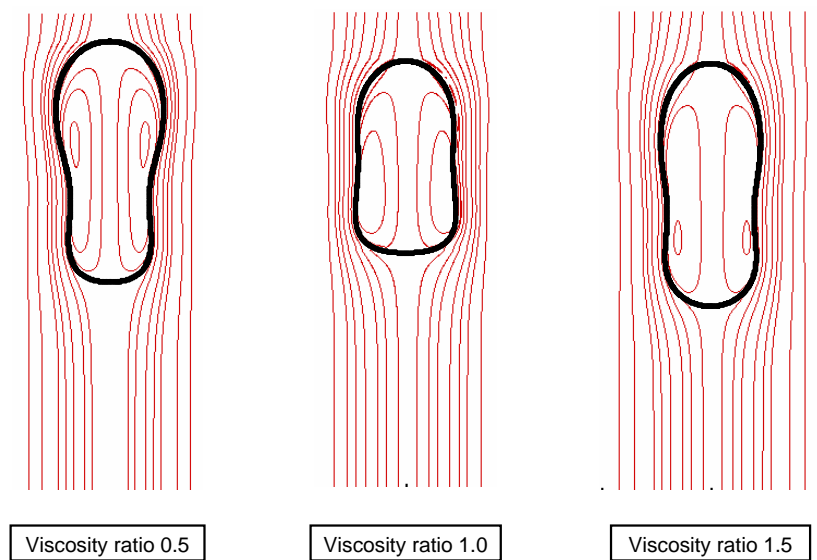


Figure 4-19. Streamfunctions for viscosity ratios 0.5 and 1.5.

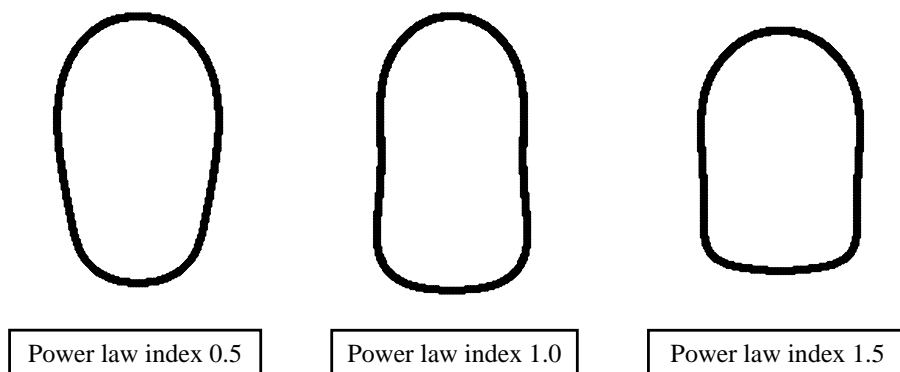


Figure 4-20. Steady state shape results from non-Newtonian fluid test for power law indexes 0.5, 1.0 (base case), and 1.5.

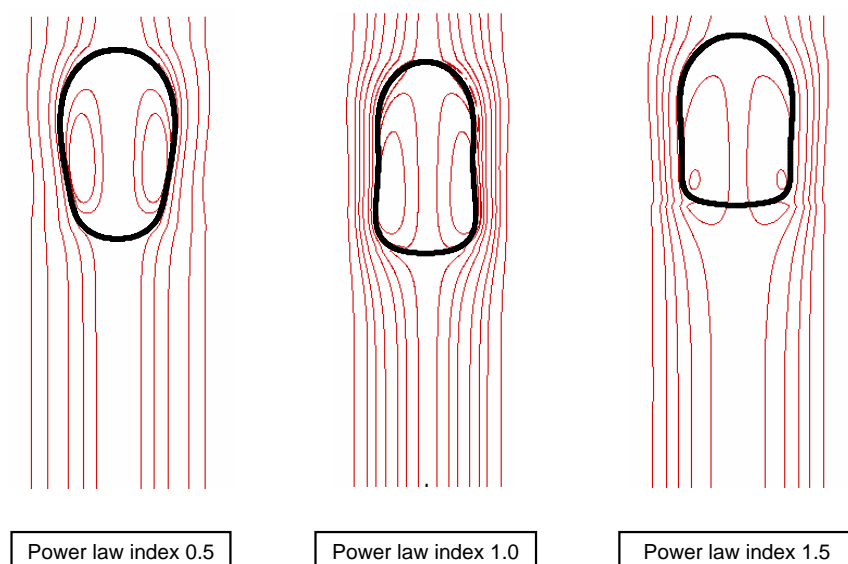


Figure 4-21. Streamfunctions for power law indices 0.5 and 1.5.

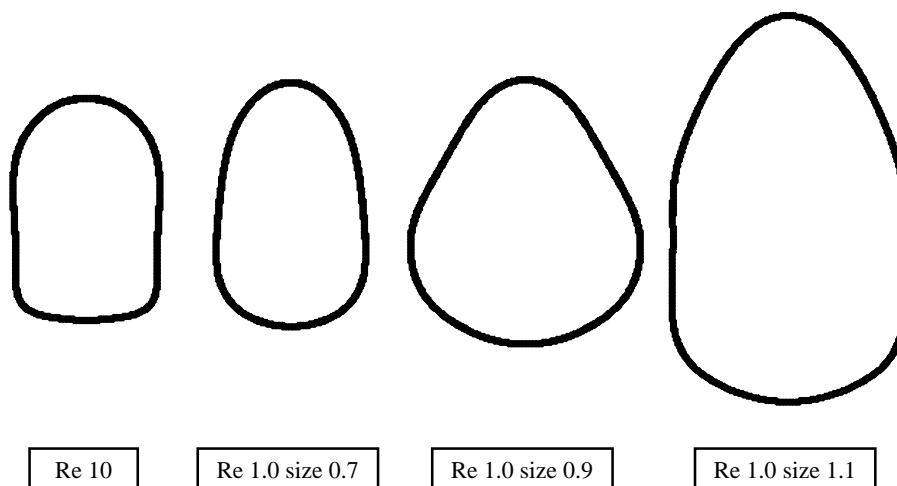


Figure 4-22. Steady state shape results from non-Newtonian fluid test for power law index 1.5, Re 10 size 0.7, and Re 1 sizes 0.7, 0.9, and 1.1.

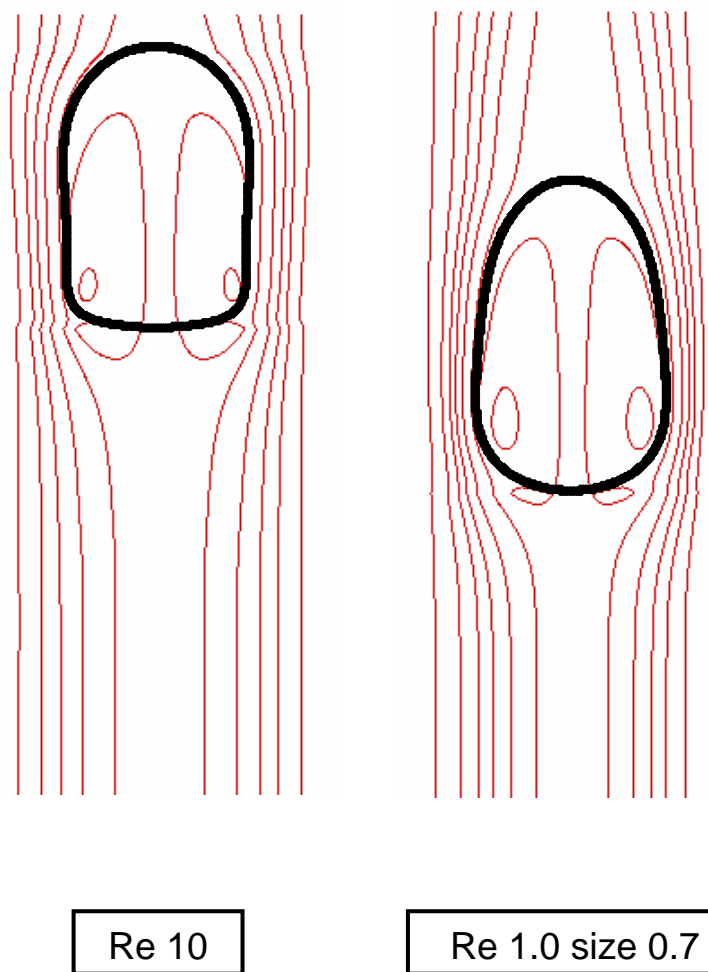


Figure 4-23. Streamfunctions for power law index 1.5 and Re 10 and 1: size 0.7.

Pressure-Driven Results

After proving the effectiveness of the new algorithm in simulating the buoyancy-driven motion of drops, the next step is to employ the technique for the higher velocity pressure-driven flow. The simulation of these flows is used to determine the effect of Reynolds and Capillary numbers on the flow conditions and drop shapes. Calculations are also carried out for non-Newtonian power law fluids. The sections below reintroduce the pressure-driven problem, explain the alterations to the code from the buoyancy-driven case, present the results of the parameter study, and discuss the conclusions gained from the data.

5.1 *Problem Formulation*

As discussed in an earlier chapter, pressure-driven flow of a drop reduces to the unidirectional flow in a pipe at points far away from the drop. Deriving the equa-

tions from axisymmetric, cylindrical conservation of momentum equations gives equations 5.1 and 5.2 for velocity and pressure.

$$\bar{v} = 2(1 - r^2) \quad (5.1)$$

$$\frac{\partial \bar{P}}{\partial z} = -8 \quad (5.2)$$

Since these conditions describe flow away from the drop, equations 5.1 and 5.2 are used as boundary conditions for velocity and pressure at the top and bottom of the computational domain. This is in contrast to the buoyancy-driven simulations, where a zero derivative condition was used for both pressure and velocity. The boundary conditions at the centerline and wall remain the same as in buoyancy-driven flow.

Besides the new boundary conditions at the top and bottom of the domain, the other change to the simulation involves the force term in the conservation of momentum equations. To simplify the problem, flow in a horizontal pipe is simulated, thus eliminating the gravitational term in the equation. The new force term is shown in equation 5.3

$$F = \frac{1}{Re} |\nabla \phi| \bar{n} \nabla \cdot \bar{n} \quad (5.3)$$

where the only term left is due to the surface tension force. The force term depends

on the normals of the interface, which are calculated from the Level Set function in the same manner as the previous code. Therefore, alteration of the boundary conditions and the force term allow the same simulation code to be implemented for pressure-driven simulations.

One last modification to the numerical technique is required due to the nature of the flow field. The velocities experienced by the drop within the pressure-driven flow are orders of magnitude larger than in the buoyancy-driven case. These high velocities move the drop through the stationary computational grid and towards the top boundary. As the drop gets closer to the boundary, the assumption of the boundary being far away from the drop breaks down, and the boundary condition that is implemented is no longer valid at that point. To overcome this problem, the grid must be moved to re-center the drop in the middle of the domain. Figure 5-1 shows this centering of the drop.

This motion is accomplished by transferring VOF, velocity, and pressure values from each grid point to a grid point below it. For example, the VOF values are moved according to equation 5.4

$$\alpha(i, j) = \alpha(i, j + COM) \quad (5.4)$$

where COM is the integer value of grid points required to bring the drop back to center. This is done over every grid point for the VOF, velocity, and pressure

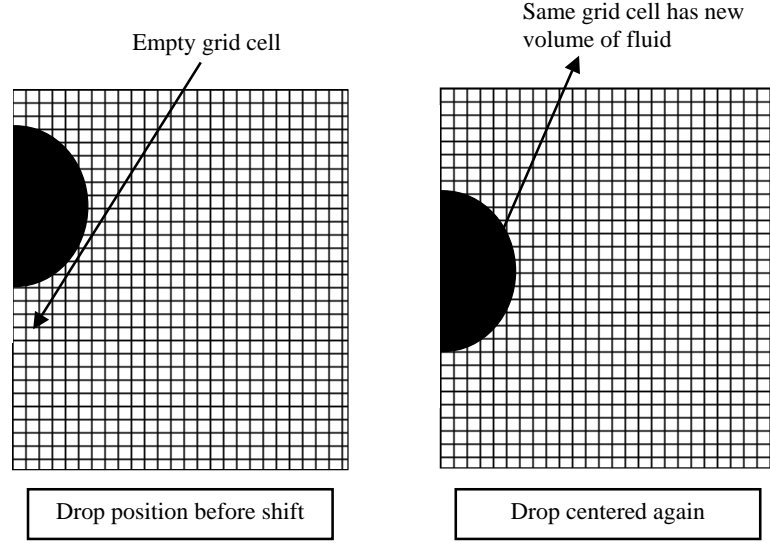


Figure 5-1. Centering drop by moving VOF values to lower grid points.

values. The points at the top of the grid where $j + COM$ does not exist in the computational domain, are given values of velocity and pressure determined by equations 5.1 and 5.2. Since these points represent space above the original computational box, the points are far away from the drop, and the undisturbed flow field values are appropriate. This grid motion is done whenever the top of the drop reaches within a distance from the top of the computational grid. Thus, the drop stays away from the boundary, and the boundary condition is valid to implement. With these alterations in the code in place, simulations of pressure-driven flow can be accomplished.

5.2 *Study on Drops in Pressure-Driven Flow*

The procedure for studying pressure-driven flow was similar to buoyancy-driven flow. First, the code was verified against previous experimental results. Then, computations were carried out to determine the effect of Reynolds numbers and Capillary numbers on the drop shape and velocity. Non-Newtonian fluids were also simulated as the suspending fluid. The next sections describe the results of these studies.

5.2.1 Comparison to Experimental Results

For drops within pressure-driven flows, previous numerical and experimental work are compared using the drop shape or deformation, drop migration velocity, and the extra pressure loss due to the drop. To match deformation, a system was chosen to mimic the numerical simulation of a clean drop within a pressure-driven flow of Johnson [25]. The parameters were chosen the same as the previous work. However the Reynolds number in Johnson is identically zero, so a small value of 0.1 was utilized in the simulation. The resulting simulation shape and the reported shape of Johnson are displayed in figure 5-2.

In figure 5-2, the shape matches well to the previous result with a slightly larger deformation in the back of the drop. This increase in deformation is possible due to the larger Reynolds number used in the simulation compared to the previous result.

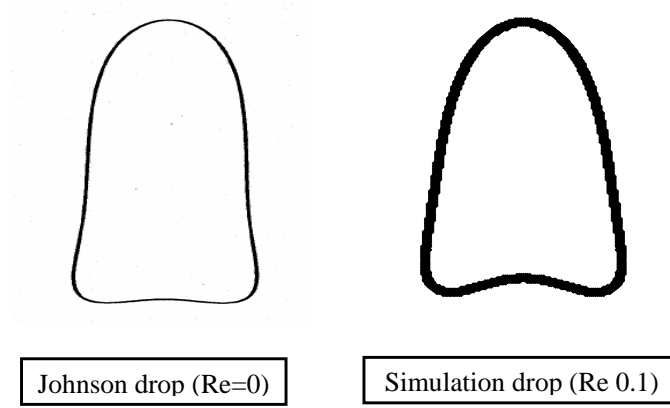


Figure 5-2. Comparison of present work shape (size ratio 0.7, viscosity ratio 1.0, density ratio 1.0, Re 0.1, and Ca 1.2) to results of Johnson 1999 [25].

Ho and Leal in their experimental work also measured an increased pressure difference due to the presence of the drop in [27]. A simulation was run to match the experimental conditions of system 1(c) (size ratio 0.914, viscosity ratio 2.04, density ratio 1.0, Re 0.09 and Ca 0.15) and compare the velocity of the drop and the additional pressure loss. The results are displayed in table 5-1.

Source of data	Relative drop velocity ($\frac{U}{V}$)	Additional pressure loss (Pa)
Ho and Leal [27]	1.32	22.5
Simulation	1.314	20.4

Table 5-1. Comparison of simulation to literature result for relative drop velocity and additional pressure loss [27].

The simulation results match the experimental velocity well. The additional pressure drop is not exactly the same as the experimental value, but the value is within 10%. Also, the additional pressure drop is difficult to measure experimentally leading to uncertainty in the value. Thus, the calculation is able to predict

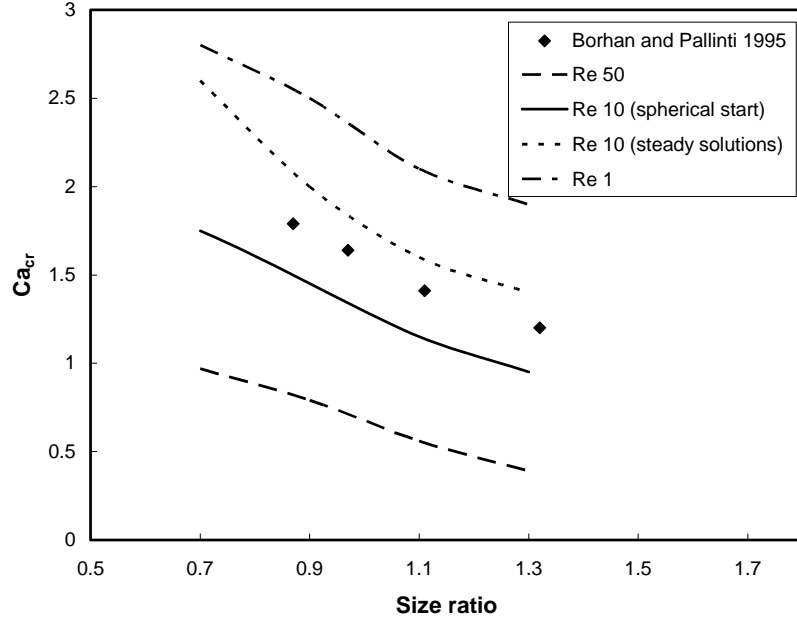


Figure 5-3. Critical Capillary numbers versus size ratio for present work at Re 1, 5, 10, and 50 and results of Borhan and Pallinti 1995 [31]; simulation parameters viscosity ratio 0.2, density ratio 0.72, Bond number 0.4.

velocity and the additional pressure drop of the experiment.

The experimental work of Borhan and Pallinti in [31] and Pallinti in [58] investigated the critical Capillary number for drop breakup. Simulations were run to match the CW8-2 experiments of [31] at higher Reynolds numbers to determine if the calculation produced the same trend in critical Capillary numbers at the higher Reynolds numbers. These simulations showed the effectiveness of the calculation in predicting drop breakup as compared with experiments. Also the runs investigated the effect of Reynolds number on critical Capillary number. The critical values of the Capillary number at different Reynolds numbers are plotted versus size ratio along with the experimental results in figure 5-3.

Figure 5-3 shows the simulations match the same trend of the experimental results. Also, the various results at different Reynolds numbers displays an interesting trend as the critical values pass through a maximum around $Re \approx 1$ and then fall to below the experimental results for larger Reynolds numbers. This trend will be further investigated in the parameter study of Reynolds and Capillary numbers.

Comparison of the simulation to previous experimental and numerical results proves the ability to predict the drop deformation, velocity, pressure, and breakup characteristics. The agreement for a variety of parameter values and types of pressure-driven flow confirms the calculation predicts the physical outcome of the system. Thus it can be used to study the effect of different dimensionless parameters on deformation, velocity, and breakup. The following sections describe the results of these studies.

5.2.2 Parameter Study of Reynolds and Capillary Numbers

Previous work in the area of pressure-driven flows has been done in the Stokes regime or $Re \ll 1$. As in buoyancy-driven motion, the goal of the study is to look at drop shapes and velocities at finite or $O(1)$ Reynolds numbers. Both the Reynolds and Capillary numbers are varied to determine their impacts. With the larger velocities of the flow field, the possibility of drop breakup occurs. The previous work of Olbricht and Kung [28] and Johnson [25] found critical values

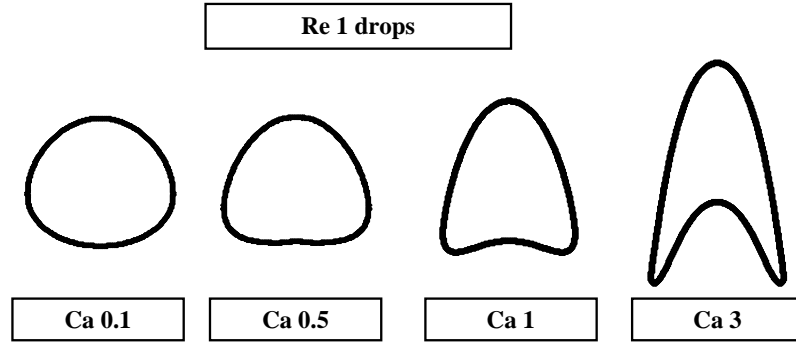


Figure 5-4. Steady state drops for Re 1, Ca values of 0.1, 0.5, 1, and 3.

of the Capillary number above which the drop breaks up. The effect of higher Reynolds numbers on this critical Capillary number is also investigated within the parameter study on Re and Ca.

The original Capillary values to be tested were 1, 5, 10, 20, and 50, the same values from the buoyancy-driven parameter study. For all the runs, the size ratio is 0.7, the density ratio is 1.0, and the viscosity ratio is 1.0. The Reynolds numbers were 1, 5, 10, and 50. After attempting these combinations, drop breakup occurred, and new values were chosen at each Reynolds number to find the critical Capillary number. For Re 1, the Capillary values tested were 0.1, 0.5, 1, and 3. Above Ca of 3.0, the drop breaks up and no steady shape is found. The steady state shapes of the runs are shown in figure 5-4.

The deformation increases with increasing Capillary number as in buoyancy-driven flow. Also, the manner of the deformation is different than the other simulations. In buoyancy-driven flow, the drops were elongated along the centerline.

These drops deform at the centerline with the bottom interface moving closer to the top of the drop with each increase in Capillary number. This motion forces the fluid inside the drop further out towards the wall and into the slower flow. Thus the sides of the drop are swept back in winglike shapes. As the Capillary number increases, the layer of fluid at the centerline decreases in length. This decrease continues until the critical Capillary value is reached and the drop breaks up. In the previous study done by Olbricht and Kung [28], this critical value was 2.28 for flow at small Reynolds numbers. The results here show a critical value of 3.0. This difference in critical values arises from finite Reynolds numbers. Apparently, the addition of inertial terms to the problem induce stability in the drops, thus raising the value of the critical Capillary number. Testing for this critical value at the higher Reynolds numbers can determine if this effect continues or is isolated to $O(1)$ Re.

The next Reynolds number tested was 5, and the Capillary values were 0.1, 0.5, 1.0 and 2.5. Figure 5-5 displays the steady shape results.

The shapes display the same trend as the Re 1 shapes with increasing winglike shapes as the Capillary number increases. The drop shape at Ca 1 is more deformed than the Re 1 shape, while the Ca 0.1 and 0.5 drops remain at small deformations. For Re 5, the critical Capillary value was found to be 2.5. This value is lower than at Re 1, so the additional inertia is destabilizing the drop. The trend is similar to the results of drop breakup simulating the experiments of Borhan and Pallinti.

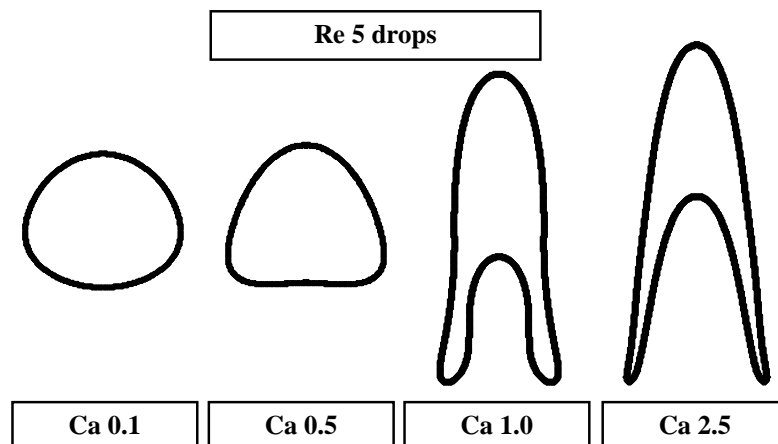


Figure 5-5. Steady state drops for Re 5, Ca values of 0.1, 0.5, 1.0, and 2.5.

The decrease in critical Capillary number is expected to continue for increasing Reynolds numbers.

Deformation parameters, D , L_A , and L_R , are calculated for each drop. These values allow comparison to a spherical drop as well as comparing the deformations between drops. Figure 5-6 displays these values versus Capillary number for the first two Reynolds numbers studied.

The deformation parameters increase with Capillary number for both sets of Reynolds numbers. However, the figures also show the increase in deformation between the two Reynolds numbers for the larger Capillary values. The Capillary values of 0.1 and 0.5 show almost no change with respect to the change in Reynolds number. The strength of the surface tension for those drops overcomes the increase in flow and the deformation stays the same.

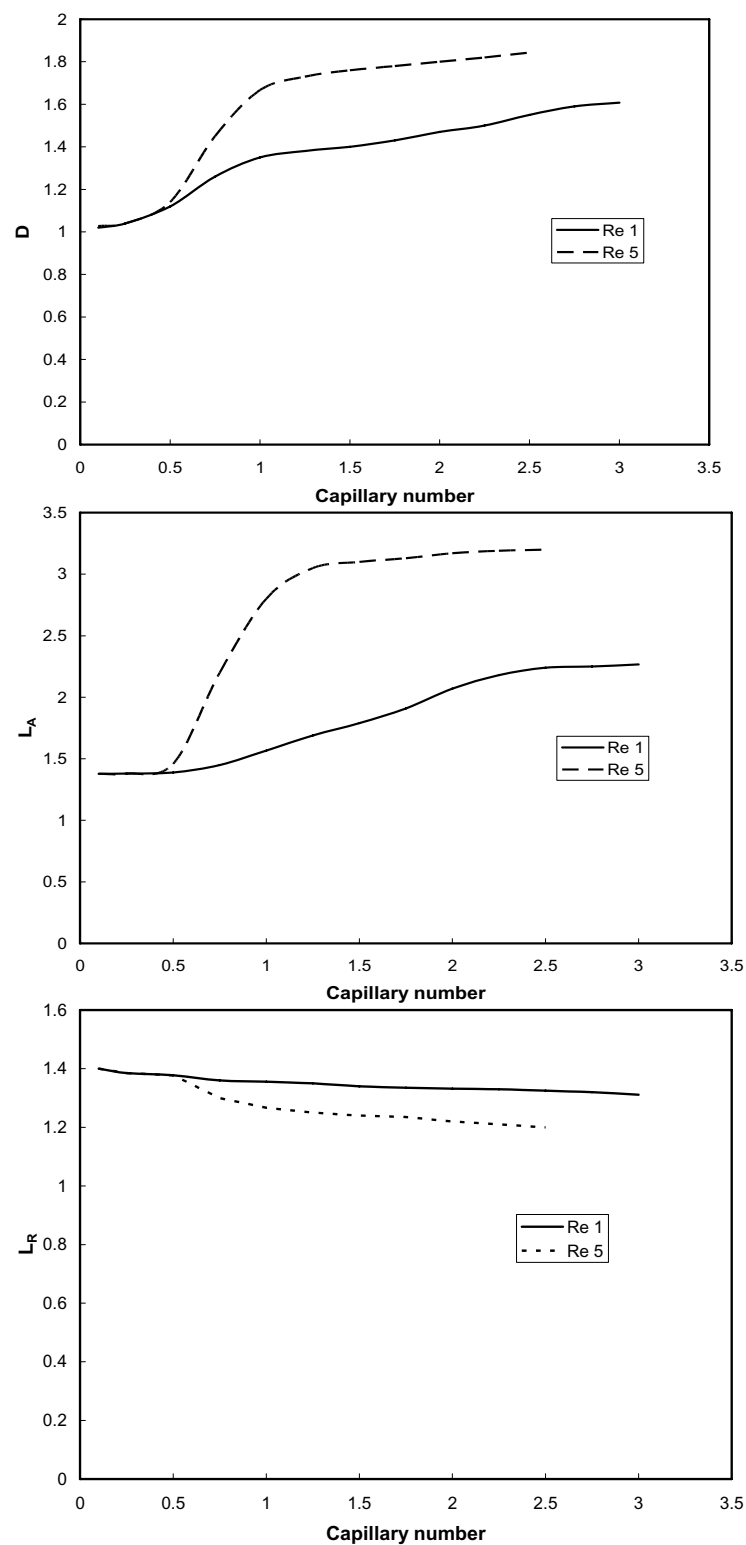


Figure 5-6. D , L_A , and L_R versus Capillary number for Re 1 and 5.

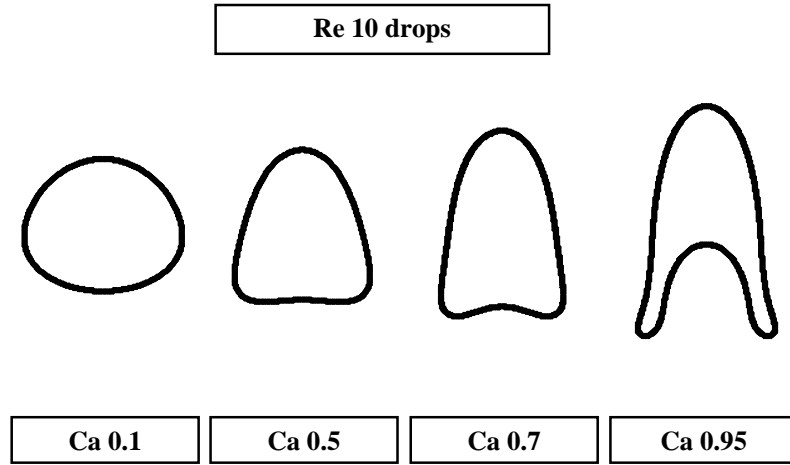


Figure 5-7. Steady state drops for Re 10, Ca values of 0.1, 0.5, 0.7, and 0.95.

The next Reynolds number tested, 10, produced drop breakup for a Capillary value of 1. Thus, the Capillary numbers tested were below 1 to obtain the critical value which still reaches steady shape. The values are 0.1, 0.5, 0.7, and 0.95. Figure 5-7 shows the steady shapes for Re 10.

Once again the deformation increases with increasing Capillary number. The simulations found $Ca_{critical} = 0.95$ for this Reynolds number. This value is less than the critical value reported by Olbricht and Kung [28]. While the critical values found for Re 1 and 5 were larger, higher values of the inertial terms reduce the stability and lower the critical value. Besides the shapes, the deformation parameters for Re 10 are shown in figure 5-8.

The deformation increases with the Capillary number, however the parameters for Ca 0.1 and 0.5 are similar to the values at Reynolds numbers of 1 and 5. The

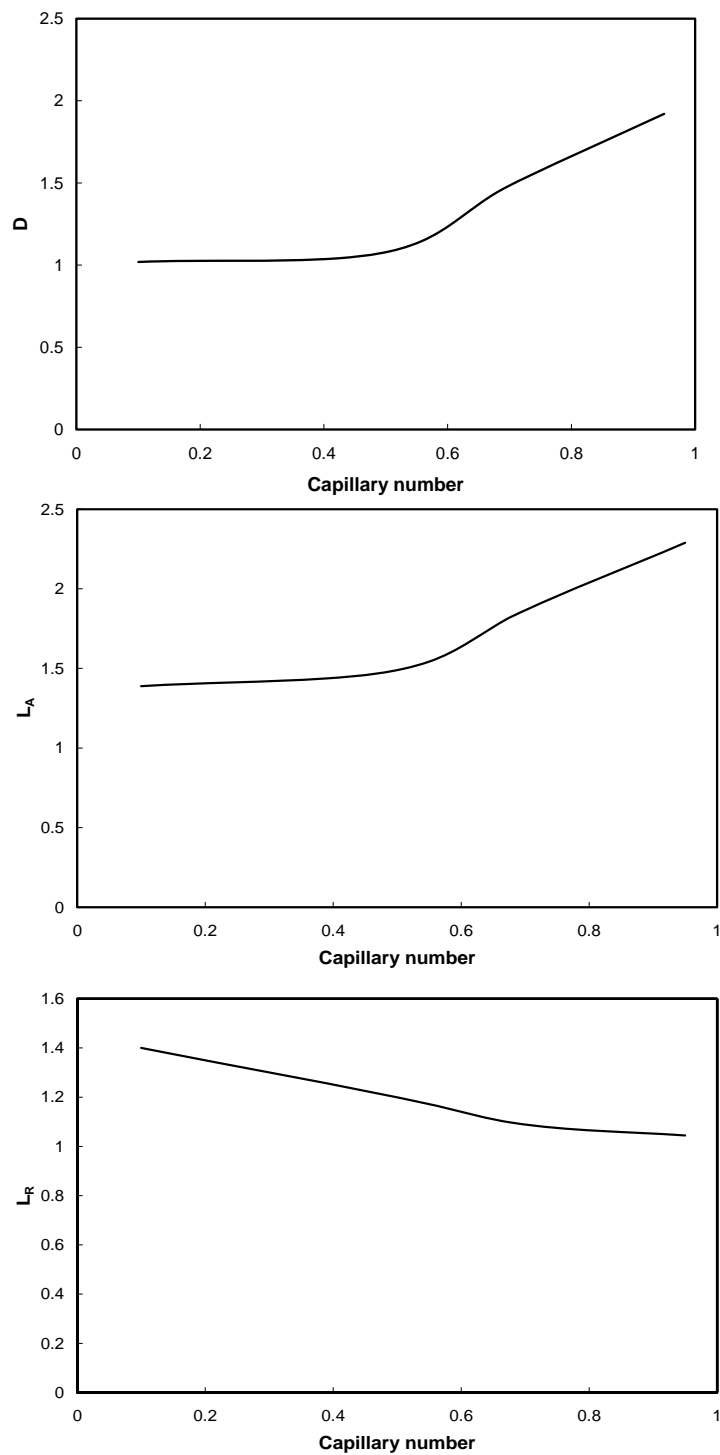


Figure 5-8. D , L_A , and L_R versus Capillary number for Re 10.

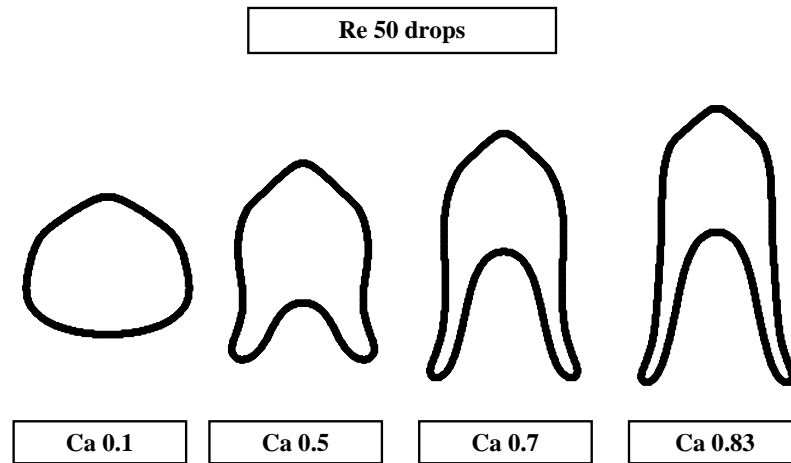


Figure 5-9. Steady state drops for Re 50, Ca values of 0.1, 0.5, 0.7, and 0.83.

Ca 0.5 case has a slight increase in deformation, but the drops retain their shapes despite another increase in flow.

The last increase in Reynolds number is to a value of 50. Steady shape Capillary numbers were found at Ca 0.1, 0.5, 0.7, and 0.83, with the critical value of 0.83. These shapes are shown in figure 5-9.

The shapes show the further deformation occurring at this high value of the Reynolds number. The deformation parameters follow the same trend as earlier Reynolds numbers and are shown in figure 5-10.

Thus the study has shown the effect both Capillary and Reynolds numbers have on drop shapes. Also, the various values for the critical Capillary number at each Reynolds number have been found. These critical values display the effect Reynolds number plays in the break up of the drops.

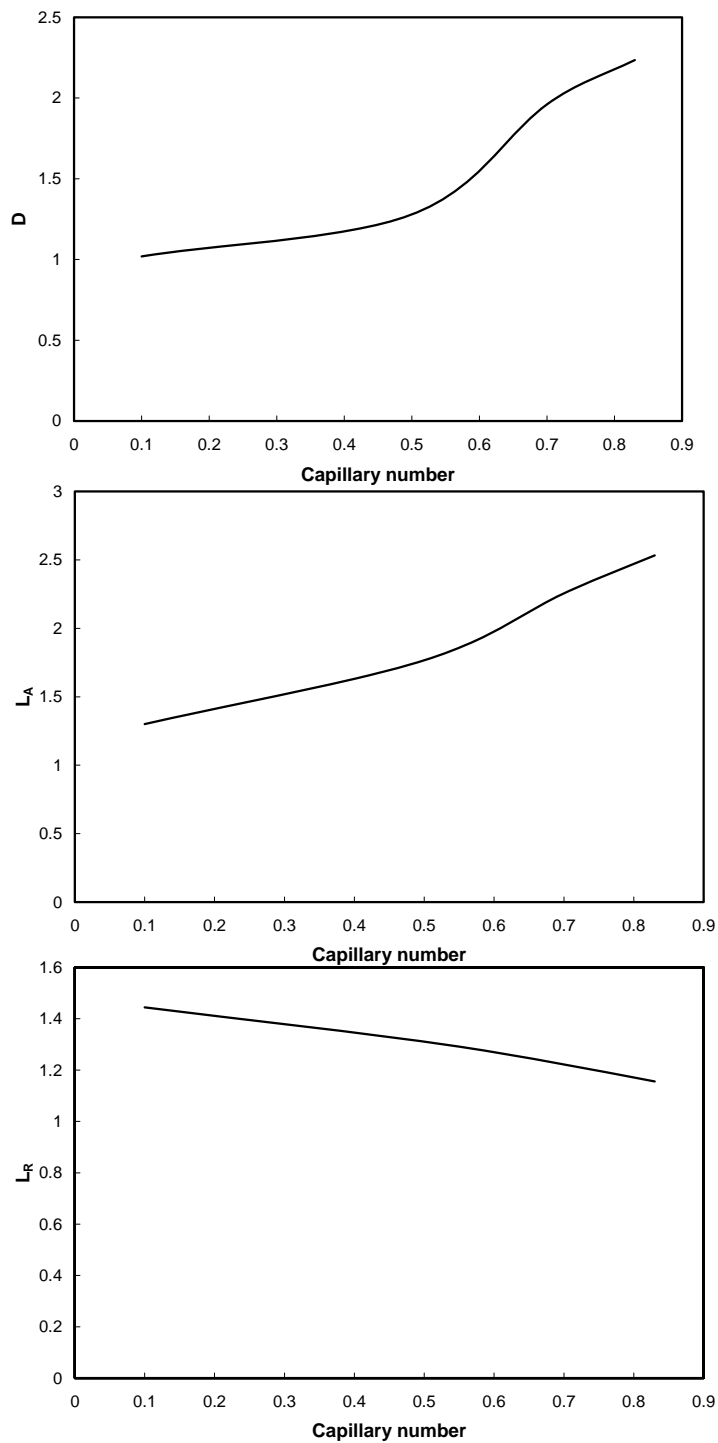


Figure 5-10. D , L_A , and L_R versus Capillary number for Re 50.

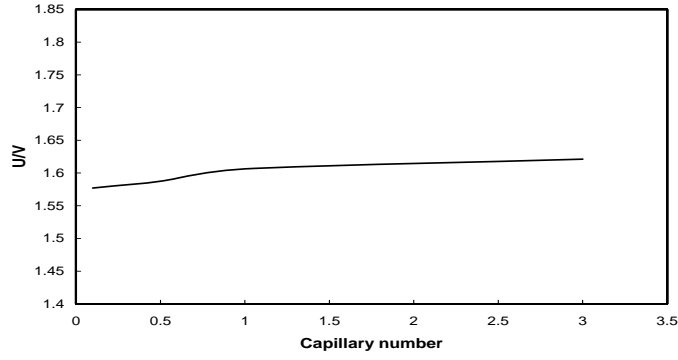


Figure 5-11. Migration velocity versus Capillary number for Re 1.

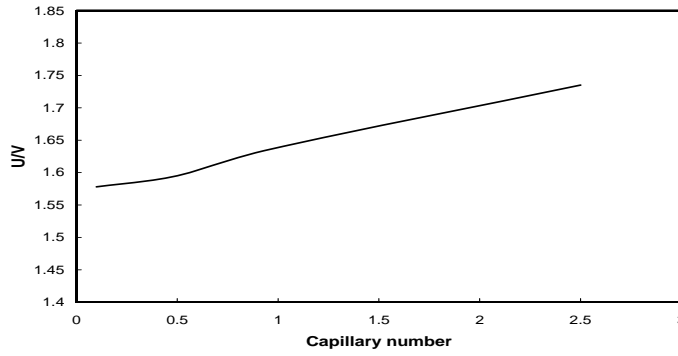


Figure 5-12. Migration velocity versus Capillary number for Re 5.

Besides drop shape, another important output of the simulation is the migration velocity. Figures 5-11, 5-12, 5-13, and 5-14 show the velocity versus Capillary number for Reynolds number 1, 5, 10, and 50 respectively.

The drop velocities increase with increasing Reynolds numbers. Also, the velocity increases with increasing Capillary number.

Streamfunction plots were also created as in the buoyancy driven simulations. Figures 5-15, 5-16, 5-17, and 5-18 show the streamfunctions for Reynolds numbers

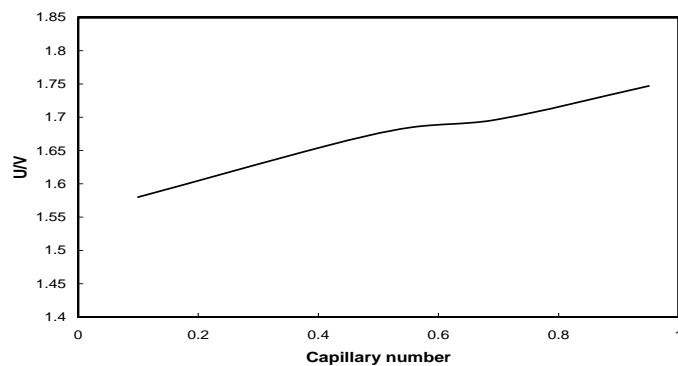


Figure 5-13. Migration velocity versus Capillary number for Re 10.

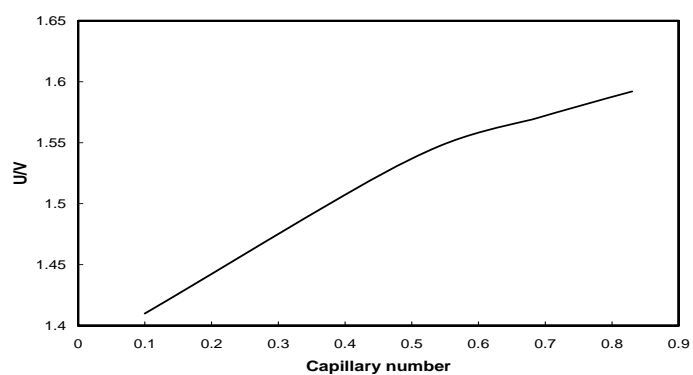


Figure 5-14. Migration velocity versus Capillary number for Re 50.

1, 5, 10, and 50 respectively.

The streamfunctions are similar to the results from buoyancy driven motion. However the pressure driven results have different recirculation zones inside the drops that vary in position with the different parameters. For the drops with lengthening tails, the highest recirculation appears to move into the thin tail region, rather than staying in the middle of the drop as in the lower Capillary number simulations. Also, the outer fluid contains recirculation zones both above and

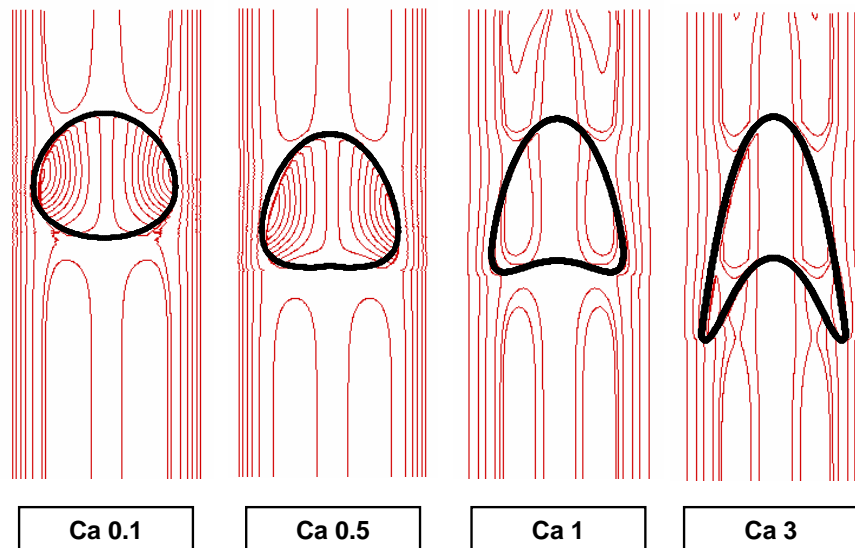


Figure 5-15. Streamfunctions for Re 1, Ca values of 0.1, 0.5, 1, and 3.

below the drop. This is the recirculation of the outer fluid due to the presence of the drop. The outer fluid is moving under the pressure gradient until it contacts the drop, forcing the fluid to turn around. This motion is evident in each of the streamfunction plots both above and below the drop. The fluid at the wall does not see the drop and just moves along the wall.

The parameter study determined the effect of Reynolds and Capillary numbers on drop size and velocity. The most interesting result out of the study, is the effect of Reynolds number on drop breakup via the critical Capillary number. To summarize, table 5-2 displays the critical values at each Reynolds number along with the literature value for small Reynolds number.

The original increases in Reynolds numbers increase the value of the critical

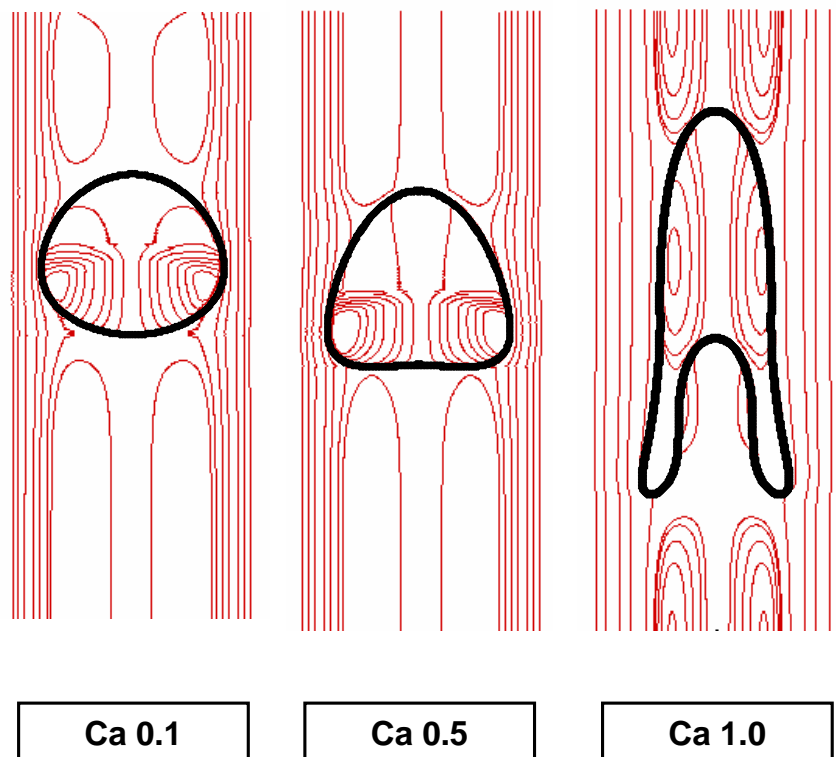


Figure 5-16. Streamfunctions for Re 5, Ca values of 0.1, 0.5, and 1.0.

Capillary number. Thus, the inertia stabilizes the drops and allows smaller surface tension drops to remain intact. Increasing the Reynolds number decreases the critical value until at Re 10 when the value is below the literature result. At this point, the added inertia destabilizes the drop and increases drop breakup. Increasing Reynolds number past this point further decreases the critical value, continuing the trend of increases in velocity adding to the drop breakup. Therefore, the finite Reynolds number has a dual effect; stabilizing the drop for Re close to

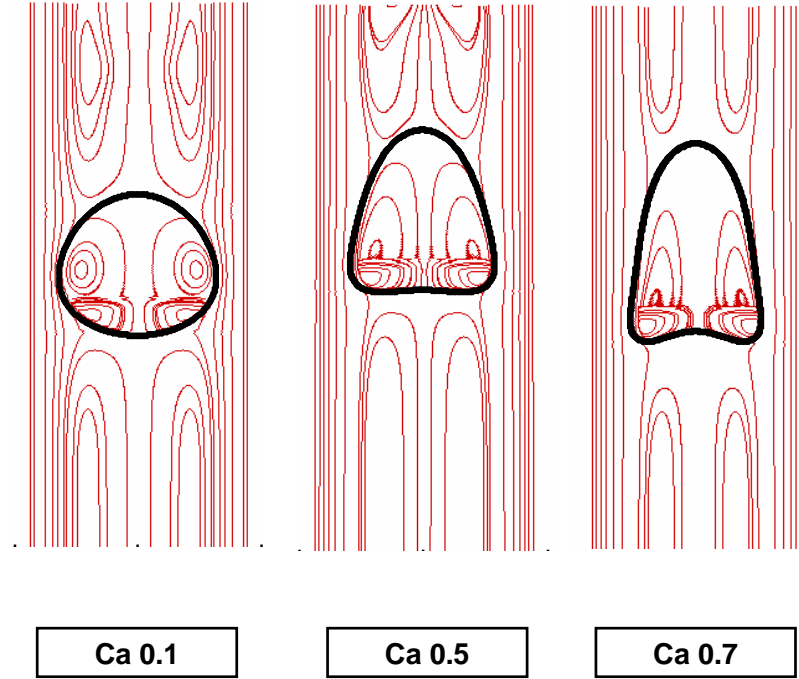


Figure 5-17. Streamfunctions for Re 10, Ca values of 0.1, 0.5, and 0.7.

Reynolds number	$Ca_{critical}$
$Re \ll 1$	2.28 [28]
1	3.0
5	2.5
10	0.95
50	0.83

Table 5-2. Critical Capillary numbers at various Reynolds numbers including literature result [28].

1, and destabilizing the system for $Re > 10$.

5.2.3 Viscosity Ratio and Non-Newtonian Tests

Besides the Reynolds and Capillary numbers, two other parameters were studied to determine the effect on drop deformation; the viscosity ratio and a non-

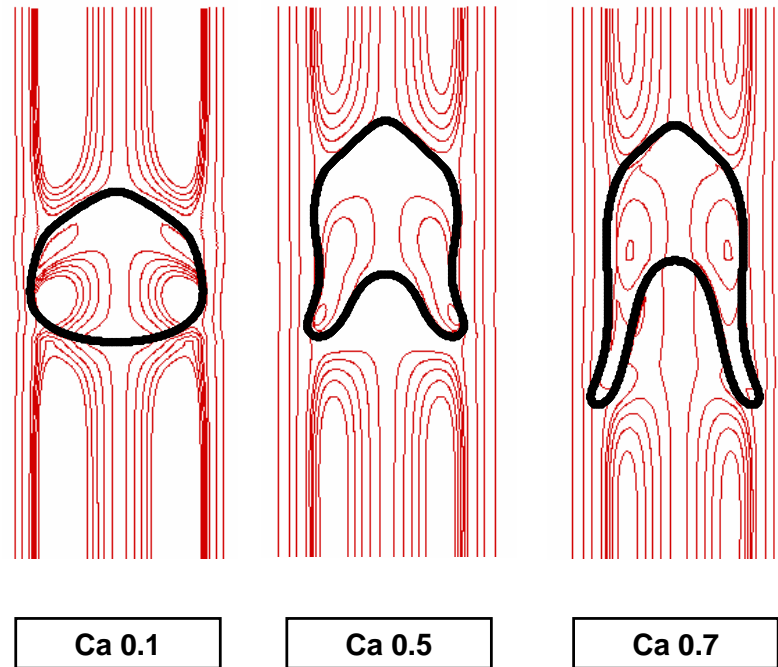


Figure 5-18. Streamfunctions for Re 50, Ca values of 0.1, 0.5, and 0.7.

Newtonian power law fluid as the suspending fluid. For the test on viscosity ratio effect, the base case was chosen as Re 5 and Ca 0.5. This set had enough deformation to show the effect of the viscosity ratio, but was away from the critical Capillary number for this Reynolds number so the change in viscosity ratio could not lead to drop breakup. The viscosity ratios tested were 0.5 and 1.5 with a value of 1.0 for the base case. Comparison of the velocities and deformation parameters are in table 5-3 and the resulting shapes are shown in figure 5-19.

The results from the viscosity ratio test show increased deformation as the viscosity ratio is increased. The more viscous drops are elongated further than at

Trial	Relative drop velocity	D	L_R	L_A
Viscosity ratio 0.5	1.585	1.078	1.365	1.4
Viscosity ratio 1.0 (base case)	1.591	1.058	1.378	1.388
Viscosity ratio 1.5	1.963	2.26	1.267	1.845

Table 5-3. Results from viscosity ratio test along with base case values

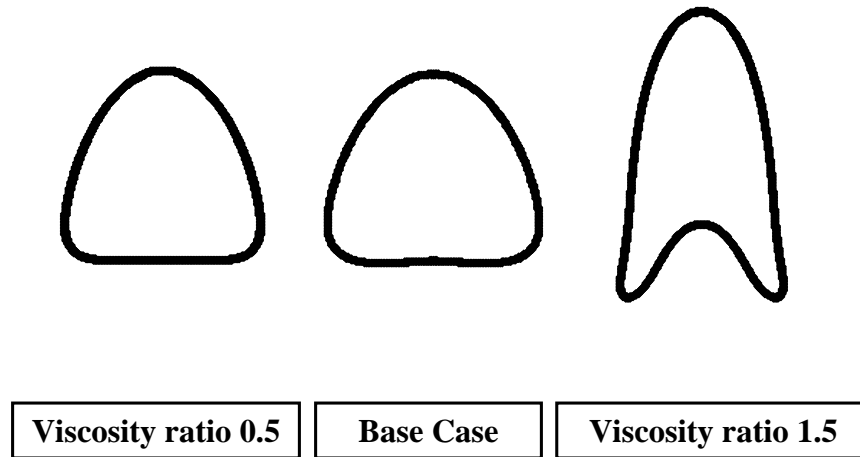


Figure 5-19. Steady state shape results from viscosity ratio test for 0.5, 1.0 (base case), and 1.5.

lower viscosity. This effect goes against intuition as the more viscous drops should be more difficult to deform. However the work of Ho and Leal [27] found this same dependence on viscosity ratio experimentally and discussed the counterintuitive nature of their findings. The increase in deformation for increasing viscosity ratio is limited to the range of $O(1)$ viscosity ratios as solid drops with infinite ratios do not deform more than bubbles that have ratios approaching zero. Since the viscosity ratios tested are within the $O(1)$ regime, the findings from the simulation are comparable to the trends of Ho and Leal, and increasing viscosity ratios lead to increased deformation.

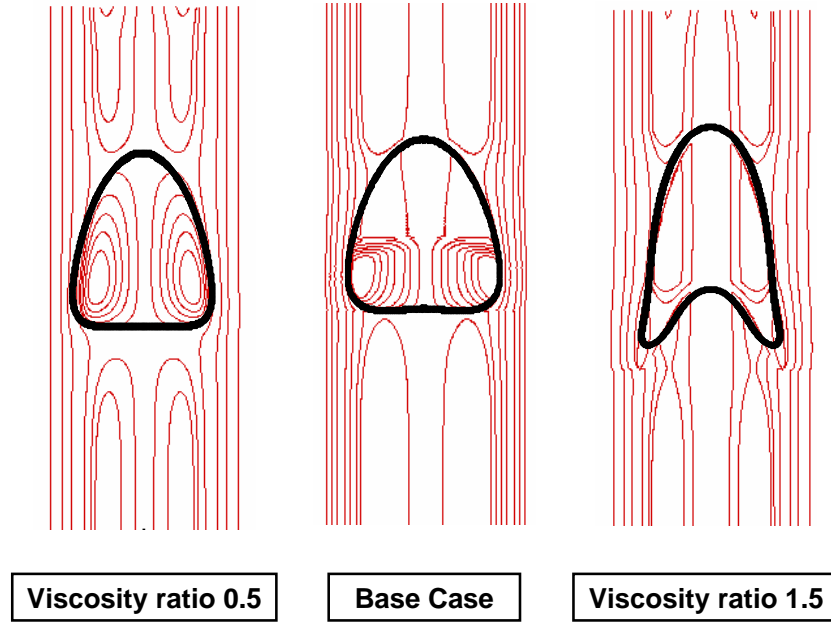


Figure 5-20. Streamfunctions from viscosity ratio test for 0.5, 1.0 (base case), and 1.5.

Streamfunctions were also plotted for the viscosity ratio test and are shown in figure 5-20.

The other study involved the simulation of a non-Newtonian power law fluid as the suspending fluid. Since the boundary conditions for the simulation, equations 5.1 and 5.2, were derived for the pressure-driven flow of a Newtonian fluid, new conditions were required for a power law non-Newtonian fluid. Solving for a cylindrical coordinate system gives equations 5.5 and 5.6 for velocity and pressure.

$$\bar{v} = \frac{3n+1}{n+1} \left(1 - r^{\frac{n+1}{n}}\right) \quad (5.5)$$

$$\frac{\partial \bar{P}}{\partial z} = -2\left(\frac{3n+1}{n}\right)^n \quad (5.6)$$

The n in equations 5.5 and 5.6 is the power law index. In the work of Ho and Leal [27], experiments were run for a viscoelastic fluid following power law behavior as well as the Newtonian fluids. Thus, a simulation was run to match the experimental conditions of Ho and Leal system 7(c), a fluid with a power law index of 0.45. The results are shown in table 5-4.

Source of data	Relative drop velocity ($\frac{U}{V}$)	Additional pressure loss (Pa)
Ho and Leal [27]	1.36	8.1
Simulation	1.357	6.9

Table 5-4. Comparison of simulation to literature result for relative drop velocity and additional pressure loss [27].

As in the Newtonian case, the simulation is able to match the experimental velocity and extra pressure drop. Besides verifying with previous work, simulations were also done to test the effect of changing the power law index. The base case was chosen the same as in the viscosity ratio test, Re 5 and Ca 0.7. The resulting shapes and deformation parameters are given in figure 5-21 and table 5-5.

Trial	Relative drop velocity	D	L_R	L_A
Power law index 1.2	1.615	1.24	1.28	1.66
Power law index 1.0 (base case)	1.591	1.058	1.378	1.388
Power law index 0.5	1.541	1.13	1.29	1.58

Table 5-5. Results from power law index test along with base case values

The shapes in figure 5-21 show the non-Newtonian drops are thinner and have a flattened back. Ho and Leal described the experimental shapes in the viscoelastic fluid as having a similar shape with a pointed head and flattened back [27]. Thus

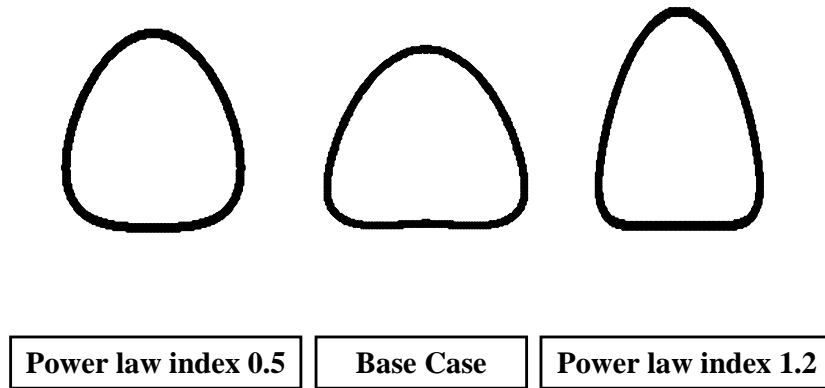


Figure 5-21. Steady state shape results from power law index test for 0.5, 1.0 (base case), and 1.2.

the drops deform just as in previous experiments. Comparison of the different power law indices displays greater deformation for the 1.2 case than the 0.5 case. This trend resembles the increase in deformation with increasing viscosity ratio. The higher power law index corresponds to a shear thinning fluid, so the suspending fluid viscosity decreases, in essence increasing the viscosity ratio. For the lower index the opposite is true, and the viscosity ratio is decreased. Therefore, the deformations in the non-Newtonian fluids are different in character to Newtonian fluids, but follow the same trend with respect to viscosity ratio as the Newtonian counterpart.

Last, the streamfunctions for the non-Newtonian test are plotted in figure 5-22.

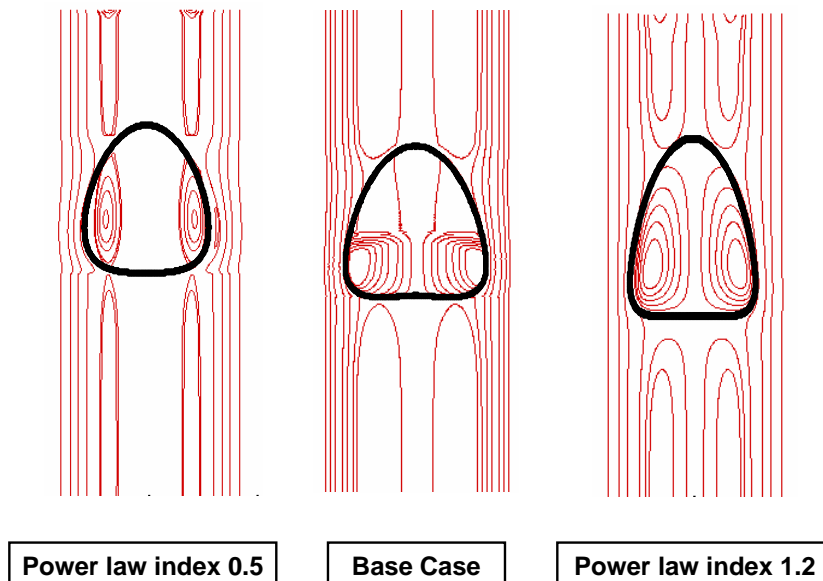


Figure 5-22. Streamfunctions from power law index test for 0.5, 1.0 (base case), and 1.2.

5.3 *Conclusions on Pressure-Driven Flow*

The simulations on pressure-driven flow further the work done with buoyancy-driven motion. The drops deform in a different manner, along the centerline of the drop rather than elongating. This deformation increases with Capillary number and Reynolds number. Also, the larger velocities in pressure-driven flow cause the drop to break apart above a critical value of the Capillary number. The computations examine the role of Reynolds number in this critical Capillary value.

To verify the validity of the alterations of the original code to model pressure-driven flow, simulations were run matching the conditions of several previous experimental and computational studies. The calculated values compared well with the

shape, velocity, and additional pressure loss of published values. Drop breakup was also examined in these comparative simulations. The critical Capillary numbers followed the same trend as the experiments versus drop size ratio. These calculations also discovered a trend in critical values for increasing Reynolds numbers. The Capillary numbers decreased as the Reynolds number increased. However, the values at $Re\ 1$ and $Re\ 5$ are above the experimental values while higher Reynolds numbers are below. It appears the small Reynolds numbers stabilize the drop and the critical values pass through a maximum before falling with increasing flow. This effect is studied further in the parameter study on Capillary and Reynolds numbers.

The parameter study found the effect of Capillary and Reynolds numbers on the deformation and velocity of the drops. As in buoyancy-driven flow, the drop deforms more as Capillary number increases. This deformation also increases with increasing Reynolds number. The drop velocities increase with increases in Reynolds and Capillary numbers. These deformations reduce the drag on the drops, and this allows the increase in drop speed.

Another effect studied in the parameter study involves the critical Capillary number. For Reynolds numbers on the order of 1, the Capillary number at which drop break up occurs is larger than the values found in previous work. The addition of the inertial terms to the flow stabilizes the drops at these Reynolds numbers. Increasing the Reynolds number above 10, reduces the critical value below the ex-

perimental values. For these runs, the larger Reynolds number and larger inertial terms introduce more instability to the drops. As the Reynolds number continues to increase, the critical Capillary number continues to decrease. Since the larger Reynolds numbers lead to more deformed drops, the behavior of the critical Capillary number for larger Reynolds numbers is expected. However, the increase of stability for low Reynolds numbers is a surprising result and should be studied more in future work.

Along with studying Reynolds and Capillary numbers, the effect of viscosity ratio and non-Newtonian fluids was determined. The viscosity ratio test showed increased deformation with increasing viscosity ratio. While this finding goes against intuition, previous experiments have seen the same trend for $O(1)$ viscosity ratios and the results here confirm that trend. Non-Newtonian fluids are studied by modeling the suspending fluid by a power law relation. To verify the computation, the simulation was matched with a previous experimental study. The results agreed, giving confidence in the calculation. Tests on different power law indices showed a different deformation in the non-Newtonian fluid. The drops became tapered in the front and flat in the back. This same deformation was reported in previous experiments with viscoelastic fluids. Also, deformation increased with increasing the power law index in a similar way to increasing the viscosity ratio. The increase in index does locally increase the viscosity ratio between the fluids, so the increase in deformation is expected.

The pressure-driven results display the ability of the algorithm to describe deformation for a different flow field. Besides the various drop shapes, the results point out the effect of parameters on drop speed and break up.

Conclusions and Future Work

The previous chapters have described the simulation predictions for the numerous cases studied in this work. In this last chapter, some physical explanations for the predictions and the advantages of this new method are discussed. Also future areas of research that can further utilize this new technique are presented.

6.1 *Conclusions*

The simulation of two-phase flows is a difficult problem that is important to a wide range of industrial applications. The new hybrid method presented here overcomes the disadvantages of previous methods by combining the best features of each into one algorithm. The numerical technique was tested on the model problem of a single drop flowing within a tube full of a different suspending fluid. This problem has previous analytical, experimental, and computational results for

a variety of system parameters. After confirming the effectiveness of the code, numerical predictions were carried out in two major areas; buoyancy-driven and pressure-driven motion of the drop.

For buoyancy-driven flows, the first simulations run were at small size ratios and Reynolds numbers to test the ability of the computation to predict migration velocity of spherical drops. The results were compared with the analytical solution for a variety of size and viscosity ratios. All of the drops remained spherical and the velocities compared well with the expected values. After testing the velocity, the next step was to compare drop shapes with previous work on deformable drops. Simulations were run in both the infinite domain and at various size ratios within a tube and compared to known data. The computations were able to match the shapes and velocities and the method was proved accurate in capturing the physics of the problem.

Once tested against previous work at lower Reynolds numbers, the method was utilized to predict systems at finite Reynolds numbers. A parameter study was undertaken on the effects of both Capillary and Reynolds numbers on the drop deformation and migration velocity. It was found that deformation increased with increasing Capillary number. As this corresponds to decreasing the surface tension, this result was expected. Also the deformation increased with increasing Reynolds number. This trend was seen in previous work and was also expected. The drops deformed by increasing in axial length, decreasing in radial length, and developing

a tail. This streamlining of the drops allows for larger drop velocity which increased with increasing deformation. Another finding out of the parameter study was the dependence of drop shape on initial conditions. Simulations using a sphere as the initial shape have different steady shapes than ones utilizing a previous steady shape as the initial condition. This suggests that there are multiple steady states and the initial condition is important to the final result.

The reason for the formation of the dimple or re-entrant cavity is difficult to predict because of the nonlinearity of the interface deformation problem even at small Reynolds number. For steady shapes, the viscous and pressure forces at the interface are balanced with the interfacial tension force. Under certain flow conditions, the viscous and pressure forces outside the drop may become so large that creation of a region of negative curvature will be required to balance the internal and external stresses. Once this negative curvature is formed, increasing the capillary number decreases the surface tension and requires a larger curvature to balance the viscous normal stresses. Thus, increases in capillary number after formation of the cavity would be expected to lead to increasing curvature of the cavity, consistent with the numerical predictions.

Besides the Capillary and Reynolds numbers, the effect of viscosity ratio was also examined. Both increasing and decreasing the ratio lead to more deformed drops, however the type of deformation is different for each. Lowering the ratio produced a drop with a thinner tail, whereas increasing the ratio leads to a more

even shaped, elongated drop. The effect of viscosity ratio in the case of buoyancy-driven motion produces a minimum in drop velocity as the viscosity ratio increases. The lowest viscosity ratio produces a larger velocity due to the decrease in drag force with decreasing viscosity of the drop phase. For the largest viscosity ratio, the larger drag expected for the more viscous drop due to presence of the wall is moderated by inertia as well as increased deformation of the drop which tends to increase the thickness of the liquid film separating the drop and the tube wall.

The last area tested was the use of a power law non-Newtonian fluid as the suspending fluid. For the lower power law index, the drop narrowed in the back, but did not elongate as in the viscosity ratio test. In the higher power law index case the drop became shorter and developed a flat back. The flat back of the drop produced a recirculation in the flow behind the drop seen in previous work where the drop shape became flat. This area was studied further by carrying out simulations for the higher index at a lower Reynolds number. The lower shape had less of the deformation, but still some recirculation. The size ratio was increased to increase the deformation and test the effect on the flow. The higher size ratios produced bullet type shapes with narrow tips and wider backs. The smaller gap between the drop and the wall also produced recirculation in the flow in front of the drop as well as the area behind the drop. The effect of the power-law index follows the predicted trend for the effect of viscosity ratio. For a larger power-law index, the stress in the outer fluid increases for fixed shear rate. This is equivalent

to a lower effective viscosity ratio for the system which is predicted to lower the drag on the drop. The opposite is true for a smaller power-law index. Thus, drop mobility would be expected to increase with increasing power-law index, which is what the computations predict.

The second major area studied was pressure-driven flow of the drop. In this case, the drop was placed into a developed flow field and allowed to deform. As in the buoyancy-driven case, simulations were carried out to compare with previous work. The computations were able to match the velocity, shape, and breakup characteristics of previous experiments and computations.

The parameter study once again studied the effect of Reynolds and Capillary numbers. As before, increasing the Capillary number increased the deformation of the drops. This increase in deformation also occurred with increased Reynolds numbers. The drops elongated as in buoyancy-driven, however the deformation also produced a flat back or dimple as the high velocity at the midpoint altered the drops.

One interesting result of the parameter study was the effect of Reynolds number on the critical Capillary number. Due to the higher velocities, the drops breakup at a certain value of the Capillary number, the critical Capillary number. The study found critical values for $Re\ 1$ and $Re\ 5$ to be higher than the reported value, and values at higher Reynolds numbers were less than the reported value. This trend was also seen in comparison with drop breakup at different size ratios.

Tests were also run for different viscosity ratios. The deformation increased with increasing viscosity ratio. For pressure-driven flow, the effect of drop deformation plays a bigger role in determining the velocity. As the deformation increases with increasing viscosity ratios, so does the velocity. This increase in deformation with increasing viscosity ratio was also reported in previous studies.

The non-Newtonian power law fluid was also used as the suspending fluid. Deformation in the power law fluid was different than the Newtonian fluid as the drop became more streamlined with a tapered head and wider back. This deformation was similar to the larger size ratios in the power law fluid for buoyancy-driven flow and to previous experiments with viscoelastic fluids. The effect of the power-law index follows the predicted trend for the effect of viscosity ratio. For a larger power-law index, the stress in the outer fluid increases for fixed shear rate. This is equivalent to a lower effective viscosity ratio for the system which is predicted to lower the drag on the drop. The opposite is true for a smaller power-law index. Thus, drop mobility would be expected to increase with increasing power-law index, which is what the computations predict again as in buoyancy-driven flows.

In general, the work shows the new hybrid method successful in simulating two-phase flows. The agreement with previous work for a wide variety of flows, parameters, and shapes, allows the computation to be used for a range of problems. The effectiveness of the method over previous VOF techniques can be further quan-

tified by comparison of drop curvatures calculated utilizing the hybrid VOF/Level Set and just the VOF alone. Table 6-1 displays the average curvature and standard deviation for various grid sizes utilizing the two numerical techniques.

Grid	Hybrid VOF/Level Set		VOF	
Spacing	Avg curvature	Deviation	Avg curvature	Deviation
30	2.00857	0.2661	0.2085	11.47
45	2.000238	0.4178	0.6536	16.929
60	1.999063	0.5315	0.3167	22.773
90	1.99764	0.7674	1.1879	33.809
120	2.0058	1.0032	0.4551	45.677

Table 6-1. Curvature of spherical drop calculated by hybrid VOF/Level Set method and VOF method

The results of table 6-1 clearly show the hybrid method to have standard deviations almost two orders of magnitude less than the VOF by itself for all the grid spacing. Since the shape was a sphere of radius 1.0, the exact curvature is 2.0. The hybrid VOF/Level Set method is within 0.5% of the exact value for all the grid spacing. The VOF by itself has errors of at least 40% for all the grid spacings tested and the hybrid method clearly improves both the accuracy and precision for calculation of drop curvatures.

The work done here developed a new algorithm for simulating two-phase flow problems. The algorithm was proven successful at matching previous experimental, theoretical, and numerical results for the model problem of a drop in a tube. The advantages of the hybrid VOF/Level Set method are in two areas. First, the hybrid method calculates drop curvature more accurately and precisely than a conventional VOF technique. At the same time, the hybrid method is able to

conserve the mass of the drop with the same precision as a conventional VOF technique. With the success of the simulation in those two areas, the method is advantageous over any of the previously used numerical solvers. The next section discusses some future uses of this hybrid method.

6.2 *Future Work*

The finite Reynolds number runs for buoyancy-driven flow predict a variety of deformation for the drops at different Capillary numbers. For the largest Reynolds and Capillary numbers, the drops begin to pinch off similar to drop breakup. Simulations at higher Reynolds and Capillary numbers should be carried out to determine if a critical Capillary number exists for buoyancy-driven flow as well. Also, the effect of the density ratio can be investigated using the simulations.

While more computations can be done for more values of all the parameters, another area that should be undertaken is experimental. Reproducing the simulation conditions in a laboratory environment will allow further verification of the code, as well as providing visual evidence of the drop shapes.

Both experiments and simulations can be done in the last area for buoyancy-driven motion, the use of non-Newtonian fluids. The different types of fluids, other than just power law fluids, can be introduced into the problem. Also, non-Newtonian fluids should be used as the drop fluid as well as the suspending to de-

termine the effects in systems with any combination of Newtonian/non-Newtonian fluids. Numerically this would require altering the code for the correct stress relationship to velocity for the given fluid. The tests should also be done experimentally to verify the simulation and the stress/velocity relation of the fluid. Since many polymeric systems are non-Newtonian fluids, these results can have an impact in polymer flow problems.

The pressure-driven flow problem has different challenges that should be looked into with further study. While the critical Capillary numbers were found for the larger Reynolds numbers, resolution problems complicated determining the critical values at the lower Reynolds numbers. To accomplish these runs, more computational time or memory is required. Parallelizing the code to work on multiple processors aids in both time and memory and needs to be carried out to run these simulations. A partial parallelizing was done for one subroutine of the program to allow the higher resolution runs. However, the increase in speed is offset by communication time between processors. A full parallelizing is required to allow for higher resolution at a reasonable computation time.

Besides the effect of Reynolds number on the critical Capillary number, simulations can be run for various density, and viscosity ratios to display the effect they have on drop breakup. Different non-Newtonian fluids should be tested to determine their impact on drop shape and critical Capillary numbers.

As in buoyancy-driven flow, experiments should be carried out for pressure-

driven flow to verify the predictions of the computations. These experiments should vary all the parameters: Re , Ca , density ratio, viscosity ratio, and non-Newtonian fluids. The experiments can confirm the simulation shapes as well as the critical Capillary numbers found for each system.

The ultimate goal of the algorithm is to model any flow system containing an interface. Along with simulating any kind of fluid, computations should be carried out for a variety of different interfacial conditions. These conditions could include the coalescence of multiple drops or any shape interface. Once the algorithm is able to simulate all these types of interfaces and systems, computations can determine the flow conditions given any system. Thus, the simulation can provide steady interface shape, velocity fields, and pressure drop of any flow problem without needing to run an experiment. This application saves the time and money required for the experiments and provides the user all the pertinent flow information necessary for the system.

Bibliography

- [1] C. D. Han and Y. W. Kim. Dispersed Two-Phase Flow of Viscoelastic Polymeric Melts in a Circular Tube. *Trans. Soc. Rheol.* **19** (1975) 245.
- [2] W. L. Olbricht. Pore-Scale Prototypes of Multiphase Flow in Porous Media. *Ann. Rev. Fluid Mech.* **28** (1996) 187.
- [3] F. P. Bretherton. The Motion of Long Bubbles in Tubes. *J. Fluid Mech.* **10** (1961) 166.
- [4] H. L. Goldsmith and S. G. Mason. The Movement of Single Large Bubbles in Closed Vertical Tubes. *J. Fluid Mech.* **14** (1962) 42.
- [5] M. Coutanceau and P. Thizon. Wall Effect on the Bubble Behaviour in Highly Viscous Liquids. *J. Fluid Mech.* **107** (1981) 339.
- [6] A. Borhan and J. Pallinti. Buoyancy-Driven Motion of Viscous Drops through Cylindrical Capillaries at Small Reynolds Numbers. *Ind. Eng. Chem. Res.* **34** (1995) 2750.
- [7] M. Manga and H. A. Stone. Buoyancy-Driven Interactions Between Two Deformable Viscous Drops. *J. Fluid Mech.* **256** (1993) 647.
- [8] R. Clift, J. R. Grace, and M. E. Weber. *Bubbles, Drops, and Particles* Academic 1978.
- [9] T. D. Taylor and A. Acrivos. On the Deformation and Drag of a Falling Viscous Drop at Low Reynolds Number. *J. Fluid Mech.* **18** (1964) 466.
- [10] R. G. Cox. The Deformation of a Drop in a General Time-Dependent Fluid Flow. *J. Fluid Mech.* **37** (1969) 601.
- [11] C. Pozrikidis. The Buoyancy-Driven Motion of a Train of Viscous Drops Within a Cylindrical Tube. *J. Fluid Mech.* **237** (1992) 627.

- [12] P. G. Saffman. The Lift on a Small Sphere in a Slow Shear Flow. *J. Fluid Mech.* **22** (1965) 385.
- [13] B. P. Ho and L. G. Leal. Inertial Migration of Rigid Spheres in Two-Dimensional Unidirectional Flows. *J. Fluid Mech.* **65** (1974) 365.
- [14] J. Magnaudet, S. Takagi, and D. Legendre. Drag, Deformation and Lateral Migration of a Buoyant Drop Moving Near a Wall. *J. Fluid Mech.* **476** (2003) 115.
- [15] G. Ryskin and L. G. Leal. Numerical Solution of Free-Boundary Problems in Fluid Mechanics. Part 2. Buoyancy-Driven Motion of a Gas Bubble Through a Quiescent Liquid. *J. Fluid Mech.* **148** (1984) 19.
- [16] D. S. Dandy and L. G. Leal. Buoyancy-Driven Motion of a Deformable Drop Through a Quiescent Liquid at Intermediate Reynolds Numbers. *J. Fluid Mech.* **208** (1989) 161.
- [17] L. A. Bozzi, J. Q. Feng, T. C. Scott, and A. J. Pearlstein. Steady Axisymmetric Motion of Deformable Drops Falling or Rising Through a Homoviscous Fluid in a Tube at Intermediate Reynolds Number. *J. Fluid Mech.* **336** (1997) 1.
- [18] R. H. Davis. Buoyancy-Driven Viscous Interaction of a Rising Drop with a Smaller Trailing Drop. *Physics of Fluids* **11** (1999) 1016.
- [19] M. A. Rother, A. Z. Zinchenko, and R. H. Davis. Buoyancy-Driven Coalescence of Slightly Deformable Drops. *J. Fluid Mech.* **346** (1997) 117.
- [20] P. C.-H. Chan and L. G. Leal. The Motion of a Deformable Drop in a Second-Order Fluid. *J. Fluid Mech.* **92** (1979) 131.
- [21] E. M. Toose, B. J. Geurts, and J. G. M. Kuerten. A 2D Boundary Element Method For Simulating the Deformation of Axisymmetric Compound Non-Newtonian Drops. *Int. J. Numer. Meth. Fluids* **30** (1999) 653.
- [22] G. Hetsroni, S. Haber, and E. Wacholder. The Flow Fields in and Around a Droplet Moving Axially Within a Tube. *J. Fluid Mech.* **41** (1970) 689.
- [23] M. J. Martinez and K. S. Udell. Axisymmetric Creeping Motion of Drops Through Circular Tubes. *J. Fluid Mech.* **210** (1990) 565.
- [24] C. Coulliette and C. Pozrikidis. Motion of an Array of Drops Through a Cylindrical Tube. *J. Fluid Mech.* **358** (1998) 1.
- [25] R. A. Johnson. Effect of Surfactants on the Dynamics of Viscous Drops. PhD. Thesis, The Pennsylvania State University, 1999.

- [26] R. A. Johnson and A. Borhan. The Effect of Surfactants on the Pressure-Driven Motion of a Drop in a Tube in the Limit of High Surface Coverage. *J. Colloid Interface Sci.* **218**(1) (1999) 184.
- [27] B. P. Ho and L. G. Leal. The Creeping Motion of Liquid Drops Through a Circular Tube of Comparable Diameter. *J. Fluid Mech.* **71** (1975) 361.
- [28] W. Olbricht and D. Kung. The Deformation and Breakup of Liquid Drops in Low Reynolds Number Flow Through a Capillary. *Phys. Fluids A.* **4** (1992) 1347.
- [29] H. Zhou and C. Pozrikidis. Pressure-Driven Flow of Suspensions of Liquid Drops. *Phys. Fluids* **6** (1994) 80.
- [30] A. Borhan and J. Pallinti. Pressure-Driven Motion of Drops and Bubbles through Cylindrical Capillaries: Effect of Buoyancy. *Ind. Eng. Chem. Res.* **37** (1998) 3748.
- [31] A. Borhan and J. Pallinti. Breakup of Drops and Bubbles Translating Through Cylindrical Capillaries. *Physics of Fluids* **11** (1999) 2846.
- [32] R. Balasubramaniam and R. Shankar Subramanian. An Exact Solution With Newtonian Interfacial Rheology and Stretching/Shrinkage of Interfacial Area Elements for Small Marangoni Numbers. *Ann. N.Y. Acad. Sci.* **1027** (2004) 1.
- [33] H. Haj-Hariri, Q. Shi, and A. Borhan. Thermocapillary Motion of Deformable Drops at Finite Reynolds and Marangoni Numbers. *Phys. Fluids* **9** (1997) 845.
- [34] M. A. Rother, A. Z. Zinchenko, and R. H. Davis. A Three-Dimensional Boundary-Integral Algorithm for Thermocapillary Motion of Deformable Drops. *Journal of Colloid and Interface Science* **245** (2002) 356.
- [35] V. Berejnov, O. M. Lavrenteva, and A. Nir. Interaction of Two Deformable Viscous Drops Under External Temperature Gradient. *Journal of Colloid and Interface Science* **242** (2001) 202.
- [36] B. D. Nichols and C. W. Hirt. Improved Free Surface Boundary Conditions for Numerical Incompressible-Flow Calculations. *Journal of Computational Physics* **8** (1971) 434.
- [37] B. D. Nichols and C. W. Hirt. Calculating Three-Dimensional Free Surface Flows in the Vicinity of Submerged and Exposed Structures. *Journal of Computational Physics* **12** (1973) 234.

- [38] C. W. Hirt, A. A. Amsden, and J. L. Cook. An Arbitrary Lagrangian-Eulerian Computing Method for All Flow Speeds. *Journal of Computational Physics* **14** (1974) 227.
- [39] C. W. Hirt and B. D. Nichols. Volume of Fluid (VOF) Method for the Dynamics of Free Boundaries. *Journal of Computational Physics* **39** (1981) 201.
- [40] A. M. C. Janse, P. E. Dijk, and J. A. M. Kuipers. The Volume of Fluid Method in Spherical Coordinates. *International Journal of Numerical Methods for Heat and Fluid Flow* **10** (2000) 654.
- [41] Y. Y. Renardy, M. Renardy, and V. Cristini. A New Volume-of-Fluid Formulation for Surfactants and Simulations of Drop Deformation Under Shear at a Low Viscosity Ratio. *European Journal of Mechanics B/Fluids* **21** (2002) 49.
- [42] J. H. Jeong and D. Y. Yang. Finite Element Analysis of Transient Fluid Flow with Free Surface Using VOF (Volume-of-Fluid) Method and Adaptive Grid. *International Journal for Numerical Methods in Fluids* **26** (1998) 1127.
- [43] D. Gueyffier, J. Li, A. Nadim, R. Scardovelli, and S. Zaleski. Volume-of-Fluid Interface Tracking with Smoothed Surface Stress Methods for Three-Dimensional Flows. *Journal of Computational Physics* **152** (1999) 423.
- [44] D. J. E. Harvie and D. F. Fletcher. A New Volume of Fluid Advection Algorithm: the Defined Donating Region Scheme. *International Journal for Numerical Methods in Fluids* **35** (2001) 151.
- [45] S-O. Kim, Y. Sim, and E-K. Kim. A First-Order Volume of Fluid Convection Model in Three-Dimensional Space. *International Journal for Numerical Methods in Fluids* **36** (2001) 185.
- [46] W. J. Rider and D. B. Kothe. Reconstructing Volume Tracking. *Journal of Computational Physics* **141** (1998) 112.
- [47] S. Osher and J. A. Sethian. Fronts Propagating with Curvature-Dependent Speed: Algorithms Based on Hamilton-Jacobi Formulations. *J. Comp. Phys.* **79** (1988) 12.
- [48] E. G. Puckett, A. S. Almgren, J. B. Bell, D. L. Marcus, and W. J. Rider. A High-Order Projection Method for Tracking Fluid Interfaces in Variable Density Incompressible Flows. *J. Comp. Phys.* **130** (1997) 269.
- [49] M. Sussman, P. Smereka, and S. Osher. A Level Set Approach for Computing Solutions to Incompressible Two-Phase Flow. *J. Comp. Phys.* **114** (1994) 146.
- [50] J. U. Brackbill, D. B. Kothe, and C. Zemach. A Continuum Method for Modeling Surface Tension. *J. Comp. Phys.* **100** (1992) 335.

- [51] Y. C. Chang, T. Y. Hou, B. Merriman, and S. Osher. A Level Set Formulation of Eulerian Interface Capturing Methods for Incompressible Fluid Flows. *J. Comp. Phys.* **124** (1996) 449.
- [52] C. Kaliakatsos and S. Tsangaris. Motion of Deformable Drops in Pipes and Channels Using Navier-Stokes Equations. *International Journal for Numerical Methods in Fluids* **34** (2000) 609.
- [53] M. Sussman and E. G. Puckett. A Coupled Level Set and Volume-of-Fluid Method for Computing 3D and Axisymmetric Incompressible Two-Phase Flows. *J. Comp. Phys.* **162** (2000) 301.
- [54] G. Son and N. Hur. A Coupled Level Set and Volume-of-Fluid Method for the Buoyancy-Driven Motion of Fluid Particles. *Numerical Heat Transfer, Part B* **42** (2002) 523.
- [55] G. Son. Efficient Implementation of a Coupled Level-Set and Volume-of-Fluid Method for Three-Dimensional Incompressible Two-Phase Flows. *Numerical Heat Transfer, Part B* **43** (2003) 549.
- [56] J. S. Hadamard. Mouvement permanent lent d'une sphere liquide et visqueuse dans un liquide visqueux. *C. R. Acad. Sci. Paris* **152** (1911) 1735.
- [57] W. Rybczynski. On the Translatory of a Fluid Sphere in Viscous Medium. *Bull. Acad. Sci. Cracow, Series A* **40** (1911) 40.
- [58] J. Pallinti. Buoyancy-and Pressure-Driven Motion of Drops and Bubbles in Vertical Cylindrical Capillaries. PhD. Thesis, The Pennsylvania State University, 1995.

Vita

Anthony Daniel Fick

Anthony Daniel Fick was born on February 26, 1976. He graduated from North Pocono High School in Moscow, PA in 1994. He received his Bachelor of Science degree in Chemical Engineering with honors and distinction from the Pennsylvania State University in 1998.

Anthony began work on his PhD. in August of 1998 working for Dr. Ali Borhan in simulation of multi-phase flow problems. He also conducted work in dynamic simulation of capillary interfacial motion. His research in capillary flows, buoyancy-driven motion of a drop within a tube, and pressure-driven motion of a drop within a tube is in the process of becoming published papers.

Anthony spent several semesters as a teaching assistant for classes in process control and fluid mechanics. He was also in charge of the chemical engineering graduate student's coed intramural flag football team. In his spare time, he enjoyed playing volleyball for a number of teams both on and off campus.